ABSTRACT

METHODS FOR THE DIRECT SIMULATION OF NANOSCALE FILM BREAKUP AND CONTACT ANGLES

by
Kyle Mahady

This thesis investigates direct simulation of fluids with free surfaces and contact lines, with a focus on capturing nanoscale physics in a continuum based computational framework. Free surfaces and contact lines have long presented some of the most challenging problems in computational fluid dynamics. Extensive progress has been made in recent years, and a wide variety of different methods are currently employed for direct simulation in these contexts. The complexity of the full governing equations for such flows poses significant challenges in terms of analytical techniques, and leads to lengthy computational times for direct simulations. For these reasons, reduced models are preferable in many contexts, even when it is not clear that such reduced models strictly apply.

Recent advances in nanotechnology motivate the comparison between direct simulations and reduced models by presenting situations in which each possesses advantages; these experiments involve the deposition of nanoscale flat metallic structures onto a surface with unprecedented precision, the almost instantaneous liquefaction of which leads to new initial liquid configurations which have been previously impossible to achieve in an experimental setup. The mechanisms that lead to the instability of these structures are a combination of classical liquid instability (such as Rayleigh-Plateau), novel capillary instabilities driven by the initial geometry, and nanoscale physics.

This study begins by examining the differences in qualitative behavior between direct numerical simulation of the full equations and a particular reduced model in the context of wetting and dewetting of drops. Afterwards, a specific initial liquid

geometry is presented, the breakup of which requires direct numerical simulation in order to explain the experimental behavior. A parameter study of this geometry demonstrates that it offers a rich variety of dynamics; the breakup of the geometry is found to result in nanoparticle arrangements previously unobtainable using similar techniques, and through careful tuning of the parameters the end state of the breakup can be various combinations of metallic filaments and nanoparticles. While such instabilities are driven by surface tension, an important class of thin film instability is driven by intermolecular fluid/solid interactions. A numerical method is developed which, for the first time, permits the explicit inclusion of this fluid/solid interaction in the context of direct numerical simulations. This method not only allows for modeling and simulating film breakup, but additionally yields a numerical method for the simulation of contact angles as well.

METHODS FOR THE DIRECT SIMULATION OF NANOSCALE FILM BREAKUP AND CONTACT ANGLES

by
Kyle Mahady

A Dissertation
Submitted to the Faculty of
New Jersey Institute of Technology
in Partial Fulfillment of the Requirements for the Degree of
Doctor of Philosophy in Mathematical Sciences

Department of Mathematical Sciences

August 2015

APPROVAL PAGE

METHODS FOR THE DIRECT SIMULATION OF NANOSCALE FILM BREAKUP AND CONTACT ANGLES

Kyle Mahady

Dr. Shahriar Afkhami, Dissertation Advisor — Date
Associate Professor of Mathematics, New Jersey Institute of Technology

---

Dr. Lou Kondic, Dissertation Advisor — Date
Professor of Mathematics, New Jersey Institute of Technology

Dr. Linda Cummings, Committee Member — Date
Professor of Mathematics, New Jersey Institute of Technology

Dr. Michael Siegel, Committee Member — Date
Professor of Mathematics, New Jersey Institute of Technology

Dr. Philip Rack, Committee Member — Date
Professor of Materials Science and Engineering, University of Tennessee Knoxville

BIOGRAPHICAL SKETCH

Author: Kyle Mahady

Degree: Doctor of Philosophy

Date: August 2015

Undergraduate and Graduate Education:

- Doctor of Philosophy in Mathematical Sciences,
  New Jersey Institute of Technology, Newark, NJ, 2015
- Bachelors of Science in Mathematics
  Montclair State University, Montclair, NJ, 2008

Major: Mathematical Sciences

Presentations and Publications:

K. Mahady, S. Afkhami and L. Kondic, "On the influence of initial geometry on the evolution of fluid filaments," submitted to *Physics of Fluids* (in review).

K. Mahady, S. Afkhami and L. Kondic, "A volume of fluid method for simulating fluid/fluid interfaces in contact with solid boundaries," *Journal of Computational Physics*, vol. 294 p 243, 2015.

K. Mahady, "Inclusion of fluid-solid interaction in Volume of Fluid to simulate spreading and dewetting for large contact angles," *Conference Presentation*, 67^{th} Annual Meeting of the APS Division of Fluid Dynamics, San Francisco, 2014.

J. Fowlkes, N. Roberts, Y. Wu, J. Diez, A. Gonzalez, C. Hartnett, K. Mahady, S. Afkhami, L. Kondic, and P. Rack, "Hierarchical nanoparticle ensembles synthesized by liquid phase directed self-assembly", *Nano Letters*, vol. 14, no 2, p 774, 2014.

K. Mahady, S. Afkhami and L. Kondic, "Comparison of Navier-Stokes simulations with long wave theory: Study of wetting and dewetting," *Physics of Fluids*, vol 25, no 11, p 112103, 2013.

N. Roberts, J. Fowlkes, K. Mahady, S. Afkhami, L. Kondic and P. Rack, "Directed assembly of one- and two-dimensional nanoparticle arrays from pulsed laser induced dewetting of square waveforms," *ACS Applied Materials & Interfaces*, vol 25, no 11, p 4450, 2013.

K. Mahady, "Influence of geometry on instability: Breakup of fluid strips with square-wave perturbations," *Conference Presentation*, 66$^{\text{th}}$ Annual Meeting of the APS Division of Fluid Dynamics, Pittsburgh, 2013.

K. Mahady, "A numerical study of nanoscale drop assembly via square-wave breakup," *Conference Presentation*, SIAM Conference on Mathematical Aspects of Materials Science, Philadelphia, 2013.

ACKNOWLEDGMENT

I would like to thank my advisors Profs. Shahriar Afkhami and Lou Kondic, for their immense patience, support, and guidance. Prof. Afkhami has been an inspiration through his enthusiasm and encouragement to pursue exciting ideas, and Prof. Kondic for his practicality and guidance.

I next thank Profs. Linda Cummings, Michael Siegel, and Philip Rack, for being on my thesis committee. Prof. Cummings and Prof. Siegel have provided invaluable feedback, assistance, and instruction during my time at NJIT. Our collaboration with Prof. Rack has provided the seed for much of my thesis work.

I would like to thank Prof. Javier Diez, for his work on our first publication together. I also thank Chris Hartnett of University of Tennessee, for his excellent experimental work and for guiding me through the experimental process.

I would like to express my gratitude to Stéphane Popinet, for writing the software package Gerris, which I have used extensively in my research.

Finally, I would like to thank the various other graduate students with whom I have collaborated and shared office space with. In particular – Ivana Seric, Nanyi Dong, and Michael Lam, have provided many useful discussions.

This research was supported in part by the The National Science Foundation under grants NSF-DMS-1320037 and CBET-1235710.

TABLE OF CONTENTS

TABLE OF CONTENTS
(Continued)

Chapter **Page**

LIST OF TABLES

Table **Page**

LIST OF FIGURES

Figure **Page**

LIST OF FIGURES
(Continued)

Figure **Page**

LIST OF FIGURES
(Continued)

Figure **Page**

LIST OF FIGURES
(Continued)

Figure **Page**

LIST OF FIGURES
(Continued)

Figure **Page**

LIST OF FIGURES
(Continued)

Figure **Page**

CHAPTER 1

INTRODUCTION

Droplets on surfaces, and their formation by means of the breakup of liquid interfaces, are ubiquitous in every day life, from a thin film of water breaking into drops on a solid substrate, to a dripping faucet. The richness of the physics of these phenomena introduces numerous complexities for both numerical and analytical study. Numerical simulations must accommodate the free surface of the liquid as it undergoes extensive deformation, as well as possible topology changes. While simulation of liquids with free surfaces is difficult, much more difficult still is the simulation of phenomena in which a solid substrate is partially covered by one liquid, as in a drop on a solid substrate.

When two immiscible fluids - for example, water and air - are in contact with a solid surface, the terms wetting and dewetting refer to the phenomena by which these fluids displace one another. For liquid on a solid surface, the intersection of the free surface of the liquid with the solid substrate is known as the contact line; this intersection is characterized by the angle formed between the interface and the solid, known as the contact angle, which may take a wide range of values depending on the properties of the fluids and the solid. The problem of wetting and dewetting has been extensively studied both theoretically and experimentally (see e.g., [4, 17, 76, 80, 81, 83, 86], and [10] for a review). In order to deal with the complexities associated with the fluid/fluid interface, wetting and dewetting phenomena are frequently modeled by means of the long–wave (otherwise referred to as lubrication, and which we occasionally abbreviate L-W) theory; see [18, 63] for reviews. Long–wave theory assumes small slopes everywhere on the interface, and is additionally typically derived assuming negligible inertial effects. The long–wave

approach allows the reduction of the complicated mathematical description to a simpler problem of a nonlinear 4th order partial differential equation for the fluid thickness. Still, even within the long–wave approach, a difficulty arises when employing the commonly used no-slip boundary condition at the fluid/solid interface: a non-integrable shear-stress singularity at the moving contact line. Simulating dynamic contact lines therefore requires additional ingredients for the model. One option is to include fluid/solid interaction forces with conjoining-disjoining terms which lead to a prewetted (often called 'precursor') layer in nominally 'dry' regions. This approach effectively removes the 'true' contact line, consequently avoiding the associated singularity [24, 31, 74]. A second approach is to relax the no-slip condition and instead assume the presence of slip at the fluid/solid interface. Both slip and disjoining pressure approaches have been extensively used to model a variety of problems including wetting, dewetting, film breakup, and many others (see, e.g., [18, 63] for reviews).

While the approach based on the long–wave model has been very successful, it is limited by the assumptions used to formulate the theory: in particular the restriction to small interfacial slopes (strictly speaking, slopes much less than unity), and therefore small contact angles. For this reason, computationally demanding direct simulations of the full governing equations may be used. A large variety of different methods for tracking the evolution of the interface are currently employed. Lagrangian methods conform the computational grid to the interface (e.g. [7, 81, 82]). Eulerian methods require a separate mechanism to track the interface location; these include front tracking methods (e.g. [91]), and interface capturing methods such as Volume of Fluid methods and level set methods. The latter two methods easily treat topology changes, and with recent developments have been shown to be effective for simulating surface tension driven flows [36, 66, 71, 87]. A common feature of Volume of Fluid methods is that contact angles are imposed geometrically, in that the angle at

which the interface intersects the solid substrate is specified as a boundary condition on the interface [1, 2, 86].

The fact that Volume of Fluid (which we occasionally abbreviate VoF) methods employ a geometrically imposed contact angle has crucial consequences for the physics of the contact line. We can contrast this most readily with the disjoining pressure methods used in long–wave based methods that we mentioned above. The geometric method forces the fluid interface to intersect the solid substrate with at an angle equal to the contact angle as a boundary condition on the interface orientation, while disjoining pressure attempts to model the underlying liquid/solid interaction that gives rise to contact angles. This is not a unique feature of long–wave based models; a variety of other computational methods have been considered in the context of wetting/dewetting which employ similar liquid/solid interactions. Here we mention phase-field methods that treat two fluids with a diffuse interface by means of a smooth concentration function, which typically satisfies the Cahn-Hilliard or Allen-Cahn equations, and is coupled to the Navier-Stokes equations. Jacqmin [49] describes a phase-field contact angle model that uses a wall energy to determine the value of the normal derivative of the concentration on a solid substrate. This model has been used to study contact line dynamics [50, 51], and similar models have been considered in the investigation of the sharp interface limit of the diffuse interface model [77, 96]. Lattice-Boltzmann methods have also treated the contact angle with a wall energy contribution [12, 55]. These approaches have explained a variety of phenomena related to spreading of fluids on solid substrates, but do not consider explicitly the long distance stabilizing and destabilizing forces between fluid and solid, as has been done via the disjoining pressure in the long–wave model.

What is crucially missing from both the Volume of Fluid based methods, as well as all of the methods described above (with the exception of long–wave), is the phenomenon of disjoining pressure. That is, the long-range interaction between a

liquid and a solid substrate does not just give rise to a contact angle, it also leads to a difference in pressure inside the liquid which is dependent on the thickness of the film, and this pressure can lead to the spontaneous rupture of the film into drops. The long distance fluid/solid interaction is naturally included in molecular dynamics (MD) simulations [37, 61, 68] that typically consider Lennard-Jones potential between fluid and solid particles. However, MD simulations are, in general, computationally expensive, even when simulating nanoscale systems. One would therefore like to be able to include liquid/solid interaction within the framework of a continuum model. While there have been methods which incorporated similar long range interactions into direct simulations (for example, the Volume of Fluid method of [52]), to our knowledge this has not been extensively applied to wetting phenomena. Such a method, which we describe in detail in this thesis, permits the direct simulation of contact angle physics, as well as film rupture.

The difference in contact angle physics between those methods which simulate the underlying liquid/solid interaction, and the geometric contact angle method used by Volume of Fluid, is of great practical interest, in addition to its obvious theoretical significance. While at large scales these two behave much the same, this can not be said at nanoscales, where the aforementioned disjoining pressure can be a dominant mechanism driving film breakup.

The natural instabilities of nanoscale films have been of great interest recently, as these have been harnessed as a means for the self-assembly of nanoparticles and nanoparticle arrays [35]. Metallic nanoparticles have great potential in a variety of applications, and have been used as a basis for controlled growth of carbon nanofibers [45], with applications in numerous settings [32]. More generally, formation of nano-structures of metallic materials finds a role in applications that range from plasmonics to liquid crystal displays and solar cells [58, 84]. For example, the size and distribution of metallic particles are known to be related to the coupling of

surface plasmons to incident energy. Controlling this coupling has the potential for large increases in the yield of solar cell devices, see, e.g., [57]; for this application, it is particularly important to be able to produce uniformly distributed and closely spaced metallic nanoparticles [6, 59]. The accurate simulation of the breakup of nanoscale films is of fundamental importance for the understanding of the mechanisms that lead to this breakup, and subsequently to control the size and distribution of the resultant nanoparticles.

Our focus for computational methods is full direct numerical simulation of the Navier-Stokes equations, where the free surface is tracked using the Volume of Fluid method. In Chapter 2, we outline the basic governing equations, and give an overview of the computational methods that we use. The equations in Chapter 2 are given in dimensional form; the nondimensionalization of these equations is specific to the needs of each subsequent chapter and will be discussed there.

In Chapter 3, we undertake a study of the comparison between direct simulation of fluid spreading on a substrate using the Volume of Fluid interface capturing method, with the classical long–wave approximation. We review basic aspects of theory of wetting drops, and describe the long–wave approximation. In order to isolate the influence of the small slope assumption inherent in long–wave theory, we present a quantitative comparison between the two methods in the regime where inertial effects are negligible. The flow geometries that we consider include wetting and dewetting drops within a broad range of equilibrium contact angles in planar and axisymmetric geometries, as well as liquid rings. For perfectly wetting spreading drops we find good quantitative agreement between the models, with both of them following rather closely Tanner's law. For partially wetting drops, while in general we find good agreement between the two models for small equilibrium contact angles, we also uncover differences that are particularly evident in the initial stages of evolution, for retracting drops, and when additional azimuthal curvature is considered. The

contracting rings are also found to evolve differently for the two models, with the main difference being that the evolution occurs on the faster time scale when the long–wave model is considered, although the ring shapes are very similar between the two models.

In Chapter 4, we turn our attention to the direct numerical simulation of the aforementioned nanoscale liquid breakups, with a particular focus on the influence of the complex initial shapes that are now possible using those methods. We study the nontrivial influence of the initial geometry on the evolution of a liquid filament deposited on a substrate. Based on the analogy to the classical Rayleigh–Plateau instability of a free-standing liquid jet, an estimate of the minimal distance between the final states (sessile drops) can be obtained. However, this numerical study shows that while the prediction based on the RP instability mechanism is highly accurate for an initial perturbation of a sinusoidal shape, it does not hold for a rectangular waveform perturbation. The results show that rectangular-wave perturbations can lead to the formation of patterns characterized by spatial scales that are much smaller than what is expected based on the Rayleigh–Plateau instability mechanism. Moreover, the nonlinear stage of the evolution and end states are not simply related, with a given end state resulting from possibly very different types of evolution; a variety of end state shapes may result from a simple initial geometry, including one- and two-dimensional arrays of drops, a filament with side drops, and a one-dimensional array of drops with side filaments. Some features of the numerical results are related to the recent experimental study by [72].

In Chapter 5, we present a novel approach to model the fluid/solid interaction forces in a direct solver of the Navier-Stokes equations based on the Volume of Fluid interface tracking method. The key ingredient of the model is the explicit inclusion of the fluid/solid interaction forces into the governing equations. We show that the interaction forces lead to a partial wetting condition and in particular to a natural

definition of the equilibrium contact angle. We present two numerical methods to discretize the interaction forces that enter the model; these two approaches differ in complexity and convergence. To validate the computational framework, we consider the application of these models to simulate two-dimensional drops at equilibrium, as well as drop spreading. We demonstrate that the model, by including the underlying physics, captures contact line dynamics for arbitrary contact angles. More generally, the approach permits novel means to study contact lines, as well as a diverse range of phenomena that previously could not be addressed in direct simulations.

In Chapter 6, we develop an improvement to the method described in Chapter 5. We show that this method has similar properties to the method of Chapter 5 with regards to the computation of contact angles. However, it requires considerably less resolution, and thus computational time, which allows it to be practically applied to thin liquid film breakup due to the fluid/solid interaction, as well as to simulations in three dimensions. We thoroughly study the instability of thin films using this method, and compare simulations with a linear stability analysis from long–wave theory. We additionally apply this method to study the rupture of such thin films, and analyze the effect of varying contact angle and parameters on the length scales of the breakup.

In Chapter 7, we summarize the present progress and describe the future outlook.

CHAPTER 2

COMPUTATIONAL METHOD

Throughout this thesis, we are concerned with the Navier-Stokes equations, formulated for two phases and subject to an incompressibility condition. When we discuss "two phases", we specifically mean two distinct, immiscible fluids. Purely as a matter of convention, one of these is referred to as a "liquid phase", and the other as a "vapor phase". As the names imply, the "liquid phase" is the fluid that forms films and drops on surfaces, and the vapor phase a fluid which occupies much of the rest of the domain; variables associated with the liquid phase are subscripted by the letter l and those associated with the vapor by v. In order to make notation clearer, we define a characteristic function, $\chi(\mathbf{x})$. This characteristic function takes the value 1 inside of the liquid, and 0 in the vapor. In dimensional terms, the Navier-Stokes equations become

$$\rho(\chi)\left(\partial_t \mathbf{u} + \mathbf{u}\cdot\nabla\mathbf{u}\right) = -\nabla p + \nabla\cdot\left(\mu(\chi)\left(\nabla\mathbf{u} + \nabla\mathbf{u}^T\right)\right) + \gamma\kappa\delta_s\mathbf{n} \tag{2.1}$$

$$\nabla\cdot\mathbf{u} = 0 \tag{2.2}$$

Here, ρ is the density, μ is the viscosity, and these both depend on the fluid phase by means of the characteristic function χ: $\rho(\chi) = \chi\rho_l + (1-\chi)\rho_v$ and $\mu(\chi) = \chi\mu_l + (1-\chi)\mu_v$. The coefficient of surface tension is γ, the interfacial curvature is κ, and δ_s is a delta function centered on the interface, so that the force due to surface tension is reformulated as a singular force as in [11]. The unknowns in this equation are the pressure p, and the velocity field $\mathbf{u}(\mathbf{x})$, which we write as $\mathbf{u} = (u, v)$ in 2D and $\mathbf{u} = (u, v, w)$ in 3D; conventionally, everything is expressed in Cartesian coordinates unless otherwise noted. Eq. (2.1) essentially reformulates Newton's second law, while Eq. (2.2) states the conservation of mass.

The most common boundary condition applied to Eqs. (2.1)-(2.2) at a solid substrate is the no-slip condition:

$$\mathbf{u} = 0 \tag{2.3}$$

The solution of Navier-Stokes equations subject to Eq. (2.3) leads to a stress singularity at a moving contact line. Modeling dynamics in this context requires some regularizing scheme to deal with the so-called 'contact line singularity', which manifests itself as an infinite stress at the line where the three phases — liquid, vapor, and solid — meet. Numerous approaches to overcome this difficulty exist, as reviewed recently in [10] and [18]. We commonly use a slip model [27, 43, 44, 46] where the no-slip boundary condition at the fluid-solid interface is relaxed. Thus, instead of having vanishing horizontal velocities at the substrate, we assume the Navier slip condition

$$\mathbf{u} \cdot \mathbf{t}_s = \Lambda \frac{\partial}{\partial \mathbf{n}_s} \mathbf{u} \cdot \mathbf{t}_s \tag{2.4}$$

where $\mathbf{t}_s$ is the substrate tangential vector and $\mathbf{n}_s$ is the substrate normal vector, and the parameter Λ is the slip length.

We solve Eqs. (2.1)-(2.2) by means of the open source software package Gerris [67]; What follows, unless otherwise specified, is an overview of the method given in [66]. Spatial discretization is accomplished by means of a quadtree (in 2D) or an octree (in 3D); the domain is decomposed into discrete square volumes, referred to as cells. All variables are defined at cell centers, and are interpreted as their average over the cell. This mesh is adaptive, allowing for effective computation of simulations with regions of very different interface curvatures and spatial scales. The interface between the two fluids is tracked using an implementation of the Volume of Fluid method. The Volume of Fluid method tracks the interface by introducing a volume fraction function, T, which is equal to the fraction of the cell occupied by the fluid

phase. The volume fraction is advected with the fluid flow, obeying the transport equation:

$$\frac{\partial T}{\partial t} + \nabla \cdot (\mathbf{u}T) = 0$$

The Volume of Fluid method reconstructs a sharp interface. For each cell, the gradient, ∇T, is computed using the Mixed-Young's method [5], so that the unit normal vector is given by $\mathbf{M} = \nabla T/|\nabla T|$. This permits a linear reconstruction of the interface in each cell, according to the equation $\mathbf{M} \cdot \mathbf{x} = \alpha$, where α is determined by T (see [73] for details).

The solution of the Navier-Stokes equations is accomplished through a time-splitting projection method. First, a predictor step calculates the auxiliary velocity field $\mathbf{u}_*$ by applying the advection terms and viscous forcing (note that in what follows a subscripted asterisk will indicate that the term is evaluated on the auxiliary field):

$$\rho_{n+1/2}\left[\frac{\mathbf{u}_* - \mathbf{u}_n}{\Delta t} + \mathbf{u}_{n+1/2} \cdot \nabla \mathbf{u}_{n+1/2}\right] = \nabla \cdot [2\mu_{n+1/2}((1-\eta)D_n + \eta D_*)] \qquad (2.5)$$

where $D = \frac{1}{2}(\nabla \mathbf{u} + \nabla \mathbf{u}^T)$ is the rate of deformation tensor. The parameter η characterizes the implicitness of the method; $\eta = 1/2$ yields a Crank-Nicholson, second order scheme, and $\eta = 1$ yields first-order accurate, fully implicit scheme. The time step is variable, and the explicit treatment of the surface tension requires [66] that the time step satisfies $\Delta t \leq \sqrt{\rho \Delta^3/(\pi\gamma)}$, where Δ is the width of the smallest computational cell. In our surface tension driven flows, this constraint dominates the time-stepping restrictions. The advection term $\mathbf{u}_{n+1/2} \cdot \nabla \mathbf{u}_{n+1/2}$ is estimated using a conservative Godunov method proposed in [9]. The discrete equation is solved using a multigrid method with Jacobi iteration scheme.

The surface tension is added to $\mathbf{u}_*$ in the next step, and is computed as a modification of the continuum surface force implementation of the surface tension

proposed in [11], where ∇T is used to approximate the $\delta_s \mathbf{n}$ in Eq. (3.1):

$$\mathbf{u}_* \leftarrow \mathbf{u}_* + \frac{\Delta t \gamma \kappa_{n+1/2}}{\rho_{n+1/2}} \nabla T_{n+1/2} \tag{2.6}$$

Interface curvature, κ, is estimated using a modification of the height function method [1, 36, 85] first proposed in [89] and described in detail in [66]. In this method, the 'height' of the fluid interface in a computational cell is calculated above a reference axis (e.g. the x axis). If we refer to the height function as f, then the curvature of the interface in two dimensions is given by the standard formula $\kappa = f''/(1 + f'^2)^{3/2}$, so that three fluid heights are required for a finite difference approximation of this curvature in each cell. The height functions are also used to impose the contact angle, as described below.

Since the velocity field must be incompressible, the auxiliary field is written, using the Helmholtz decomposition, as

$$\mathbf{u}_* = \mathbf{u}_{n+1} + \frac{\Delta t}{\rho_{n+1/2}} \nabla p_{n+1/2} \tag{2.7}$$

where again p is the pressure. Taking the divergence of both sides leads to a Poisson equation,

$$\nabla \cdot \left(\frac{\Delta t}{\rho_{n+1/2}} \nabla p_{n+1/2} \right) = \nabla \cdot \mathbf{u}_* \tag{2.8}$$

The divergence-free velocity field is finally given by

$$\mathbf{u}_{n+1} = \mathbf{u}_* - \frac{\Delta t}{\rho_{n+1/2}} \nabla p_{n+1/2} \tag{2.9}$$

The volume fraction T is solved for at half timesteps by a conservative method; the variables $\mu_{n+1/2}$ and $\rho_{n+1/2}$ are thus known through their functional dependence on the volume fraction function.

We treat the contact angle differently depending on the context. In Gerris, the two dimensional code implements the contact angle as described in [1]. In this

method, the slope of the interface in the contact line cell is imposed so that the angle formed by the interface with the substrate is θ_{eq}, and the forcing due to the contact angle enters into Eq. (3.1) through the surface tension term. It is thus sufficient to modify the computation of the curvature term to take this into account. The height of the fluid in the contact line cell is found from a linear reconstruction of the interface in that cell, using the value of the volume fraction T and the slope determined by θ_{eq}. In order to have a large enough stencil of heights to compute the curvature, 'ghost cells' are introduced, which are cells outside the domain where the height function and T are defined. The height function in the ghost cells is found by extending the linear reconstruction in the contact line cell into the ghost cells. The same method as above is used for $\theta_{eq} = 0$, and is equivalent to setting $T = 1$ in the ghost cells.

In three dimensions, there is no implementation of general contact angles, so our choices are limited by that is possible by specifying boundary conditions on T. We can impose a 90° contact angle by setting a homogeneous Neumann condition on T on the substrate; since the interface normal is given by ∇T, this implies that $\nabla T = (\partial_x T, 0, \partial_z T)$, and thus this is equivalent to a 90° contact angle. Likewise, setting $T = 1$ on the substrate results in a 0° contact angle, and $T = 0$ a 180° contact angle. It is important to note that the computational method developed in Gerris is accurate when dealing with surface tension driven flows. We demonstrate the accuracy and the convergence of these simulations, in the context of spreading drops, at the end of Chapter 4. Chapters 5 and 6 discuss a new computational method for including the contact angle in Gerris for both two and three dimensional simulations.

CHAPTER 3

COMPARISON OF NAVIER-STOKES SIMULATIONS WITH LONG–WAVE THEORY: STUDY OF WETTING AND DEWETTING

3.1 Introduction

The comparison between the results of Navier-Stokes equations and the long–wave model is the main focus of this chapter. Despite the wide application of long–wave based models, we were unaware of benchmark tests considering the validity of long–wave model by comparing its solutions to direct numerical solutions of the full Navier-Stokes system in a fully dynamic setting. To accurately describe the evolution under general conditions, it is important to consider a more complete theory, and discuss the degree of agreement. This agreement (or lack of it) is of relevance also for practical reasons: obtaining direct solutions of Navier-Stokes equations is computationally demanding, and knowing precisely when long–wave model can be used, and with which degree of accuracy, is needed.

As we discuss in detail below, carrying out this comparison in a meaningful way is not trivial, since the models necessarily involve their own sets of definitions of relevant quantities (such as contact angle). Therefore, comparing 'raw' data, such as front positions as a function of time, for example, turns out not to be always very insightful; instead, we carry out the comparison by considering the degree of agreement of the two models with asymptotic solutions in the form of Cox-Voinov and Tanner's laws [88] for the flow regimes where these laws are expected to be valid. To facilitate the comparison between the models and the asymptotic solutions, we concentrate on flow configurations such that inertial effects are not significant (to the degree possible), capillary numbers are reasonably small, and the effect of the vapor phase is minimal. Furthermore, we consider relatively simple flow geometries,

so to be able to focus on the comparison between the models, and not necessarily on the complexities which may be expected if more complicated flow problems were treated. First we consider the classical problem of a wetting or dewetting drop on a substrate in two and three dimensions. Second, motivated by recent works on liquid metals [3, 93, 94], we investigate the fluid ring geometry [39].

The remainder of this chapter is organized as follows. In Section 3.2, we present the full governing equations including a Navier slip model [27, 43, 46, 44] to alleviate the stress singularity at the moving contact line which occurs when the no-slip condition is applied on the substrate [47]. We continue by describing the long–wave model which also uses the slip model for consistency with the Volume of Fluid based solver, and specifies the contact angle via a disjoining pressure approach, discussed in some detail in [24]. In Section 3.3 we systematically investigate the degree of agreement between the models for both wetting and dewetting problems in two and three (axisymmetric) dimensions. Section 3.4 considers the problem of a fluid ring structure collapsing into a drop. We conclude in Section 3.6.

3.2 Models

The governing equations that we will study in this chapter are the Navier-Stokes equations, Eqs. (2.1)-(2.2). We nondimensionalize by choosing the velocity scale to be $U = \gamma/\mu_l$ and the length scale to be $L = \mu_l/(\rho_l U)$. With these scales, Eqs. (2.1)-(2.2) remain formally the same:

$$\rho\left(\partial_t \mathbf{u} + \mathbf{u}\cdot\nabla\mathbf{u}\right) = -\nabla p + \nabla\cdot\left[\mu\left(\nabla\mathbf{u} + \nabla\mathbf{u}^T\right)\right] + \gamma\kappa\delta_s\mathbf{n}, \tag{3.1}$$

$$\nabla\cdot\mathbf{u} = 0. \tag{3.2}$$

Here, $\rho = 1$ in the liquid phase and $\rho = \rho_v/\rho_l$ in the vapor phase, where ρ_v is the vapor phase density. Similarly, $\mu = 1$ in the liquid phase and $\mu = \mu_v/\mu_l$ in the vapor phase, where μ_v is the vapor phase viscosity. We have γ represent a unit surface

tension. The ratios ρ_v/ρ_l and μ_v/μ_l are both set to 1/100; for these ratios, we have found that the influence of the exterior fluid on the results is negligible. Likewise, the Navier slip boundary (Eq. (2.4)) condition remains formally the same

$$u = \Lambda \frac{\partial u}{\partial y} \tag{3.3}$$

where Λ is the dimensionless slip length. Solution of Eqs. (3.1)-(3.3) are solved via Gerris, as described in Chapter. 2

3.2.1 Long–Wave Model

The long–wave approach allows for the reduction of the Navier-Stokes equations to a single nonlinear partial differential equation for the fluid thickness, h. We note that although this approach is strictly valid only for fluid configurations characterized by small free surface slopes, it has been commonly used in situations where the contact angle is not necessarily small. The partial wetting conditions can be considered in the model by accounting for van der Waals forces between solid and fluid, as briefly described below.

The comparison between the results of long–wave approach and solutions of the Stokes or Navier-Stokes equations has been considered in the literature, but mostly for steady state configurations. For example, [64] compares the solutions for the steady cross section of a rivulet flowing down a plane obtained by solving the complete Navier-Stokes equation with the predictions of the long–wave approach (see their Table I). For a contact angle of 30°, they find that the differences between both approaches related to the shape of the free surface are of the order of a few percents. The appropriateness of the use of long–wave approach was also discussed earlier in [41]. In that work it was shown that there are some differences in the free surface slope between long–wave theory and Stokes formulation, but only very close to the contact line.

In the present chapter, the partial wetting conditions are included in the long–wave model via the disjoining pressure $\Pi(h)$, which represents the effects of the intermolecular forces through the solid/liquid interface (see, e.g., [24] and the references in that paper). Using the time and length scales defined previously, the resulting (nondimensional) equation for the fluid thickness, $h = h(x, y, t)$, which also includes the Navier slip boundary condition, Eq. (2.4), is (see, e.g., [63])

$$3\,\frac{\partial h}{\partial t} + \nabla \cdot \left(H^3 \nabla \nabla^2 h\right) + \nabla \cdot \left[H^3 \nabla \Pi(h)\right] = 0 \tag{3.4}$$

where $H^3 = h^2(h + 3\Lambda)$. Here, the first term stands for viscous dissipation and the other two terms account for the driving forces, which are surface tension and disjoining pressure, respectively. For disjoining pressure, we use power-law form

$$\Pi(h) = K_{dj}\left[\left(\frac{h_*}{h}\right)^m - \left(\frac{h_*}{h}\right)^n\right] \tag{3.5}$$

where the exponents satisfy $m > n > 1$. The first term represents the liquid/solid repulsion, while the second term stands for the attraction, and when they balance, Eq. (3.5) predicts a stable film of dimensionless thickness $h = h_*$. Here, K_{dj} is a dimensionless pressure scale given by $K_{dj} = \mathcal{A}L/(6\pi\gamma h_*^3)$, where $\mathcal{A}$ is the Hamaker constant for the liquid/solid/vapor configuration [48]. Instead of characterizing the interaction by means of $\mathcal{A}$, it is also possible to relate K_{dj} with the equilibrium contact angle, θ_{eq}, as discussed in some detail in e.g., [24]. Briefly, through the 'augmented' Young-Laplace condition, which assumes a local equilibrium of pressures, one obtains $K_{dj} = \tan^2\theta_{eq}/(2M)$ where $M = (m-n)/((m-1)(n-1))$; we use $(m, n) = (3, 2)$, and $h_* = 10^{-3}$ except if specified differently. Note that here we are assuming a dependence on θ_{eq} in the form of $(\tan^2\theta_{eq})/2$ instead of $(1 - \cos\theta_{eq})$ as usually seen in the literature [24, 74]. In fact, the former dependence comes directly from using the linearized form of the free surface curvature [60], which is consistent with the hypothesis of small slope in the long–wave approximation, while the latter is derived

when using the complete (nonlinear) form. The connection between K_{dj} and θ_{eq} has been recently discussed in more detail in [38].

In the present chapter, we concentrate on one-dimensional solutions of Eq. (3.4), in both planar and axial geometry. To consider both cases simultaneously, we write Eq. (3.4) in the form

$$3\frac{\partial h}{\partial t} + \frac{1}{x^d}\frac{\partial}{\partial x}\left[x^d H^3 \frac{\partial}{\partial x}\left(\frac{1}{x^d}\frac{\partial}{\partial x}\left(x^d \frac{\partial h}{\partial x}\right) + \Pi(h)\right)\right] = 0 \tag{3.6}$$

where $d = 0, 1$ for planar and axisymmetric cases, respectively. The evolution from a given initial condition, $h(x, 0)$, towards equilibrium is calculated by solving Eq. (3.6) using a numerical code discussed elsewhere [23]. It is worth pointing out that inclusion of Navier slip in the present long–wave model is not needed from the computational point of view; we include, however, slip effects anyway so to facilitate the comparison with the Volume of Fluid results, where slip is required. One consequence is the presence of two length scales in the long–wave model (the slip length and the thickness of prewetted layer), increasing the complexity. To simplify, we always use $h_* \ll \Lambda$ (for $\Lambda \neq 0$) so that, as discussed in the following section, the results are not influenced by the value given to h_*.

Before proceeding with the comparison of the models, it is worth pointing out their differences: (i) Volume of Fluid requires externally imposed contact angle, considers a two fluid problem, and includes inertial effects, and (ii) the long–wave approach requires the presence of a prewetted layer (of the thickness comparable to h_*), requires disjoining pressure to specify contact angle, and ignores the inertial effects. While, in principle, non-zero contact angle can be implemented in the long–wave approach by specifying it externally, we consider on the physical grounds that using disjoining pressure for this purpose is more appropriate. In order to minimize, if not completely remove these differences, in this chapter we proceed as follows: (i) consider a low inertia, surface tension dominated regime (i.e., the Reynolds

and capillary numbers are small); (ii) analyze carefully what is the influence, if any, of the prewetted layer and disjoining pressure on the long–wave results, and (iii) concentrate on the ratio of the fluid densities and viscosities in the Volume of Fluid simulations such that the vapor phase has no influence on the results. As we will see below, we find that the influence of the thickness of the prewetted layer and the details of disjoining pressure model are minimal, allowing us to concentrate on the intrinsic differences between the considered models.

3.3 Partially Wetting Drops: Spreading and Retracting

In the simulations that follow, we take as initial configuration a fluid geometry characterized by an initial contact angle, θ_i, different from the equilibrium contact angle, θ_{eq}, so that the imbalance of forces leads to contact line motion and bulk flow, until θ_{eq} is reached. In particular, we take the initial fluid profile to be the portion of the circle with radius R and center $(0, -R\cos\theta_i)$ lying above the x-axis. In the long–wave simulations, the fluid profile is lifted by an amount h_*. An equilibrium contact angle, θ_{eq}, is specified on the solid substrate, and we consider spreading and retracting of planar and axisymmetric drops from the initial to the equilibrium configuration using Volume of Fluid and long–wave simulations.

As we will see below, direct comparison of the two models (e.g., considering front positions as a function of time suggests significant differences between the two models; the unifying features can be extracted by considering the relation between the instantaneous contact angle, θ, θ_{eq}, and the contact line front velocity, v_f, that is expected to be satisfied based on the well known Cox-Voinov law [92]

$$\theta^3 - \theta_{eq}^3 = 9Ca\log\left(h_M/h_m\right) + O(Ca) \tag{3.7}$$

Here we define the capillary number as $Ca = \mu_l U v_f/\gamma$, h_M is a macroscopic length scale, and h_m is a microscopic length scale. With our choice of scales, Ca and the

Reynolds number, $Re = \rho_l L U v_f/\mu_l$, satisfy $Ca = Re = v_f$. Note that the Cox-Voinov law is derived under the assumptions of Stokes flow dominated by capillary effects, with the only restriction that $\theta < 3\pi/4$.

For our purposes, we consider this general form of the Cox-Voinov law:

$$\theta^3 - \theta_{eq}^3 = aCa^b \tag{3.8}$$

with a prefactor, a, and exponent, b. As we will see, the differences between the two models will require focusing on b when discussing the agreement of the models between themselves, and with this generalized form of the Cox-Voinov law; a is discussed in some more detail in the Remarks at the end of this section. The exponent b is computed by performing a least squares fit in the above equation over a representative portion of the spreading process, defined by $Ca > 0.001$, and $\theta^3 - \theta_{eq}^3 < 0.7(\theta_i^3 - \theta_{eq}^3)$. This choice ensures that the drop is spreading fast enough so that its speed can be accurately resolved, and removes any transient effects associated with early times. Spreading speeds on the order of or less than 0.01 are typical; this places us in a viscous, capillary regime where the Cox-Voinov and the long–wave equations are applicable. Moreover, this choice ignores the early phase of spreading and retraction, which is not governed by Eq. (3.8).

For the Volume of Fluid simulations, the quantities in Eq. (3.8) are computed in the following way. The front location, x_f, is taken to be the intersection of the reconstructed interface with the x-axis. The front velocity, v_f, is then computed using discrete values of x_f by simple finite differences. Velocities are computed only when the cell which contains the front is of a specified volume fraction; this ensures that the front velocities are all comparable. To find the contact angle, we consider the volumes of the drops. In planar geometry the cross-sectional area is given by $A = R^2(\theta - \sin\theta\cos\theta)$, where R is the radius of the circular cap, while in the axisymmetric case we have $V = (\pi R^3/3)\left(2 - 2\cos\theta - \sin^2\theta\cos\theta\right)$. The front location is given by

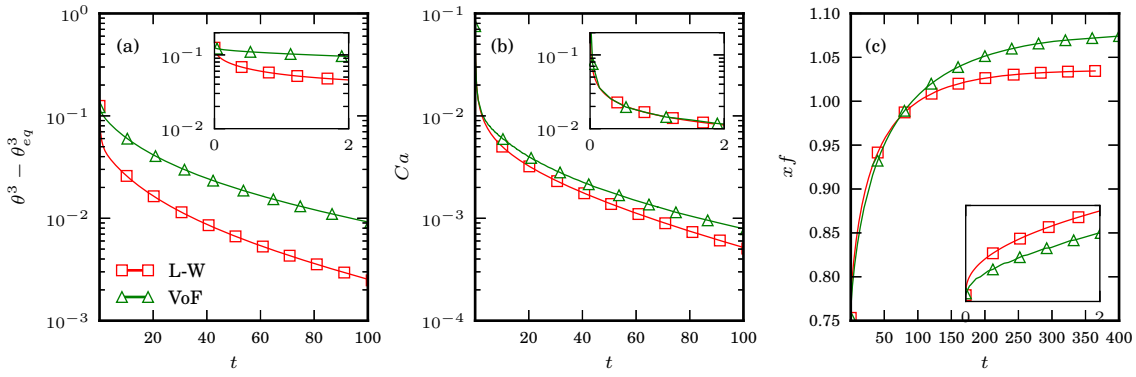

Figure 3.1 Planar drop spreading from an initial contact angle of 30° to an equilibrium contact angle of 15°, with $\Lambda = 0.01$ for long–wave and Volume of Fluid simulations, showing, as a function of time: (a) $\theta^3 - \theta^3_{eq}$, (b) Capillary number Ca, and (c) Front location x_f. Note the different time range in part (c). Insets plot each quantity for $t < 2$.

$x_f = R \sin\theta$, so that fixing the volume V (A in the planar case) yields simple nonlinear equations for the contact angle θ. In the long–wave computations, θ is defined as the slope at the inflection point of the thickness profile $h(x,t)$ near the contact region, i.e. where h is close to h_*.

To illustrate the differences between the results of the models, and to further motivate the comparison with the Cox-Voinov law, Figure 3.1 shows $\theta^3 - \theta^3_{eq}$, Ca, and x_f versus time for the planar drop spreading from 30° to 15° with $\Lambda = 0.01$. In the part (a) we see that θ decreases more rapidly in long–wave for early times, while for intermediate and large times, the trend in both models is similar, although $\theta^3 - \theta^3_{eq}$ is different in magnitude. The difference in early time behavior is partially explained by the fact that the initial condition, a circular cap, is also the shape of the quasi-static solution for the Volume of Fluid model, while the long–wave drop must relax to its quasi-static shape, which is parabolic (except in the contact line region where it matches smoothly h_*). Another possible reason for the different behavior for early times may be due to the inertial effects that are not included in the long–wave model.

The inset in Figure 3.1(b) shows that the behavior of Ca is similar in both models for early times, and although Ca is somewhat smaller for the long–wave model, both evolutions share similar trends. Figure 3.1(c) shows the front location as a function of time. As mentioned above, the final equilibrium shapes are different for long–wave and Volume of Fluid, and consequently, their equilibrium values of x_f differ as well.

In order to compare the results with the Cox-Voinov law, we consider three cases: a small contact angle drop spreading from $\theta_i = 30^\circ$ to $\theta_{eq} = 15^\circ$ already considered in Figure 3.1; a larger contact angle drop spreading from $\theta_i = 45^\circ$ to $\theta_{eq} = 30^\circ$; and a drop retracting from $\theta_i = 30^\circ$ to $\theta_{eq} = 45^\circ$. For each case, we consider two slip lengths, one large, $\Lambda = 0.046875$, and one small, $\Lambda = 0.01$ (the former value is chosen for convenience, since it is exactly 12 times the minimum cell size in the Volume of Fluid simulations). These cases will be analyzed for both planar and axisymmetric drops. For the planar drops, the volume per unit length, i.e., area, is held constant at $A \approx 0.21$, while for the axisymmetric case the volume is held at $V \approx 0.15$, both corresponding to an initial front location $x_f = 0.6$ for $\theta_i = 45^\circ$.

Figure 3.2 shows $\theta^3 - \theta_{eq}^3$ versus Ca for the planar drop. Both models show a similar trend. A transient initial period where Ca rapidly decreases while θ changes very little is reflected in the flat regions at the far right of each curve. This is followed by the spreading phase where θ relaxes to equilibrium and Ca is smaller than approximately 0.1. The most obvious difference between the curves resulting from the two models is that the long–wave curves are generally shifted to the right (meaning, e.g., that for a given θ, the drops spread or retract faster under the long–wave model). This shift can be traced back to the differences in the initial evolution of θ for the two models.

The dashed lines shown in Figure 3.2 are the best fits of the functional form given by Eq. (3.8). The resulting exponent, b, is given in Table 3.1; It turns out

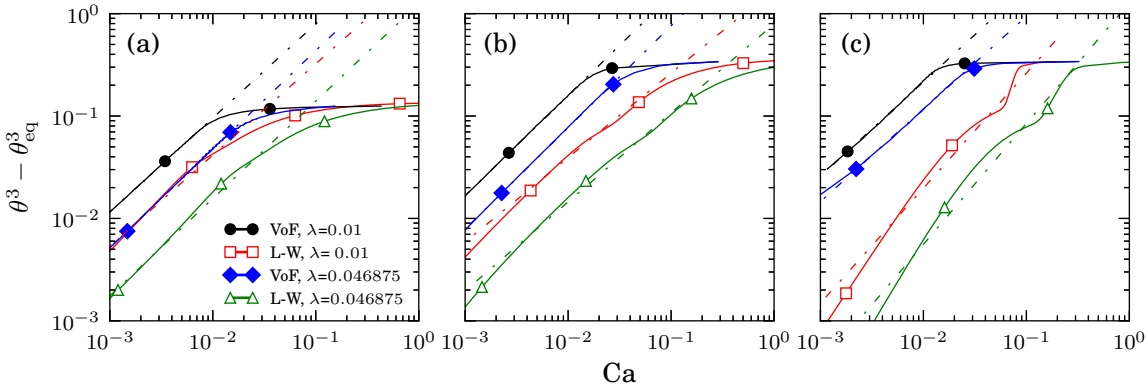

Figure 3.2 Planar drop spreading and retracting for the long–wave and Volume of Fluid models for various slip lengths. The following cases were considered: (a) drop spreading from an initial contact angle of 30° to 15°; (b) drop spreading from 45° to 30°; (c) a drop retracting from 30° to 45°. The dashed line show the best fits to the data of the form specified by Eq. (3.8). The definitions of the symbols used are given in the part (a) of this and the following figures.

$0.9 < b < 1.0$ for the Volume of Fluid model. For the long–wave simulations, $b \approx 1$ for the $(\theta_i, \theta_{eq}) = (30°, 15°)$ and $b \lesssim 0.9$ for the $(45°, 30°)$ spreading drop. For retracting drops, long–wave results give $1.1 < b < 1.2$, but we also note that the retracting drop is not well described by the power law prescribed by Eq. (3.8).

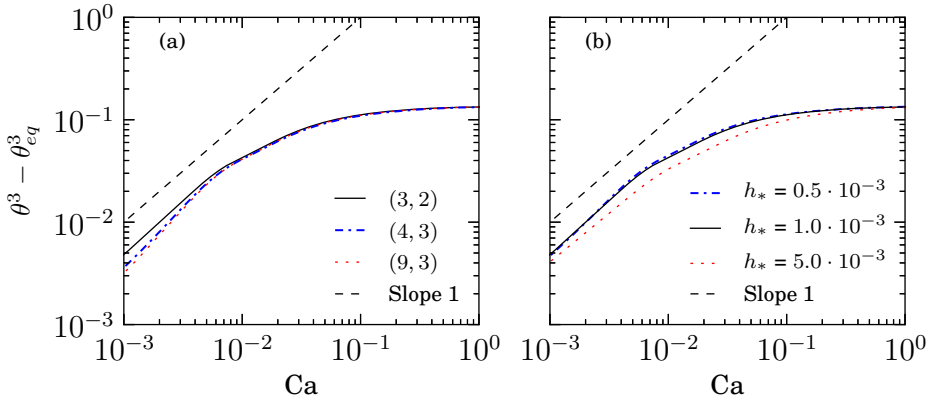

Figure 3.3 Effects of h_* and the exponents (m, n) on the relation between Ca and θ for the planar $(30°, 15°)$ spreading drop with $\Lambda = 0.01$: (a) for different h_* and $(m, n) = (3, 2)$; (b) for different pairs (m, b) and $h_* = 10^{-3}$.

There are two parameters in the long–wave model that do not appear in Volume of Fluid simulations, namely, the equilibrium thickness, h_*, and the pair of exponents

Table 3.1 Values of b Resulting From Fitting the Evolution of Planar Drops with a Spreading Law of the Form $\theta^3 - \theta_{eq}^3 \propto Ca^b$, for Long–Wave and Volume of Fluid Simulations.

	Volume of Fluid	long–wave
30°-15°, slip 0.01	0.92	0.89
30°-15°, slip 0.046875	0.96	0.95
45°-30°, slip 0.01	0.98	0.82
45°-30°, slip 0.046875	0.99	0.87
30°-45°, slip 0.01	0.92	1.1
30°-45°, slip 0.046875	0.90	1.2

(m, n). It is a natural question to ask whether these quantities influence the long–wave results. Figure 3.3 shows that their influence is very weak. In particular, we see that values of h_* smaller than 10^{-3} do not affect the presented results; additional simulations (not shown for brevity) suggest that the exact value given to h_* is not relevant as long as $h_* \ll \Lambda$. The influence of the exponents (m, n) is minor as well, although one may note that the pair $(3, 2)$ gives the slope closer to unity for small Ca than the other two pairs of exponents.

Figure 3.4 shows $\theta^3 - \theta_{eq}^3$ versus Ca for an axisymmetric drop. The computed exponent, b, is given in Table 3.2. Similarly to the planar case, we find that the power law behavior with $b = 1$ describes well the Volume of Fluid simulations for spreading as well as for retracting drops, and the long–wave simulations for spreading drops. For retracting drops, the long–wave curves are not well described by the power law dependence prescribed by Eq. (3.8), viz. Figure 3.4(c).

Remarks:

• It is appropriate to comment on the value of a in Eq. (3.8). Recall the rapid reduction in $\theta^3 - \theta_{eq}^3$ found in the long–wave simulations for early times, see

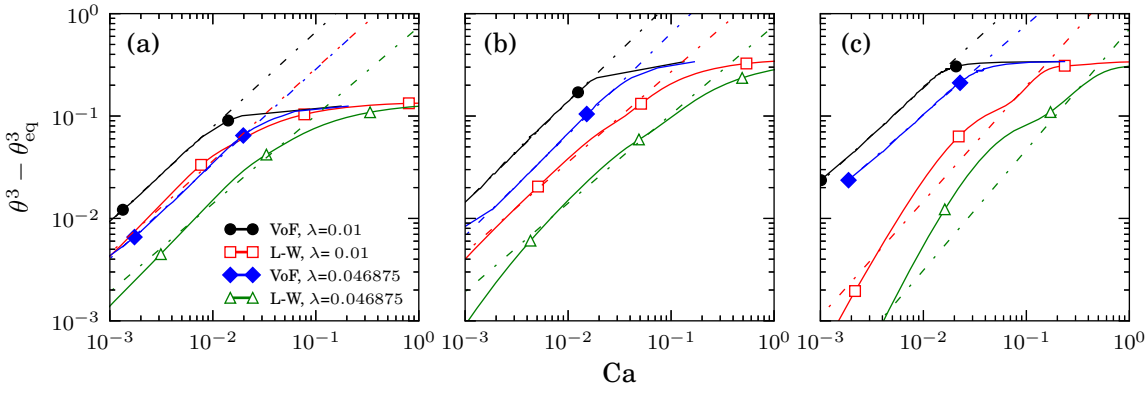

Figure 3.4 Axisymmetric drop spreading and retracting for the long–wave and Volume of Fluid models for various slip lengths. The following cases were considered: (a) drop spreading from an initial contact angle of 30° to 15°; (b) drop spreading from 45° to 30°; (c) a drop retracting from 30° to 45°. The dashed line shows the best fits to the data of the form specified by Eq. (3.8).

Figure 3.1(a). This reduction, together with (approximate) power law behavior for late times, ($b \approx 1$), requires that Ca is larger in the long–wave model, for equivalent θ. In terms of Eq. (3.8), a must be smaller for long–wave drops, so direct comparison of a between the two models is not appropriate. This finding suggests that the interpretation of the length scales appearing in Eq. (3.7) has to be different; we further discuss these length scales below. Here we also note that the exact values of a are difficult to extract accurately from the present data, and this is one of the reason we have so far concentrated on b, which can be found much more accurately, and in addition is not influenced by the differences in the early time evolution.

• Recent works [10, 30] consider the asymptotic limit of spreading drops in the small slip and contact angle limit, including discussion of the length scales entering into the Cox-Voinov law, Eq. (3.7). The approach followed suggests that $h_M \propto x_f$, and $h_m \propto \Lambda/\theta_{eq}$. As $\theta \to \theta_{eq} \ll 1$, volume conservation gives $x_f \propto \theta_{eq}^{-1/(d+2)}$, (where again $d = 0, 1$ for planar and axisymmetric geometry, respectively); from this one finds that $h_M/h_m \propto \theta_{eq}^{(d+1)/(d+2)}/\Lambda$. We briefly discuss how our results compare to this prediction.

Table 3.2 Values of b Resulting From Fitting the Evolution of Axisymmetric Drops with a Spreading Law of the Form $\theta^3 - \theta_{eq}^3 \propto Ca^b$, for Long–Wave and Volume of Fluid Simulations.

	Volume of Fluid	long–wave
30°-15°, slip 0.01	0.93	0.90
30°-15°, slip 0.046875	0.92	0.86
45°-30°, slip 0.01	0.98	0.88
45°-30°, slip 0.046875	0.99	0.87
30°-45°, slip 0.01	0.92	1.13
30°-45°, slip 0.046875	0.88	1.18

1. Figures 3.2 and 3.4 show that increasing Λ shifts both long–wave and Volume of Fluid curves downward a similar amount on the log-log plot, suggesting that both models share similar dependence on Λ for both planar and axisymmetric drops, consistently with [30].

2. For both planar and axisymmetric drops, we observe in Figure. 3.2 and 3.4 that for spreading drops, the difference between the long–wave and Volume of Fluid curves increases for larger θ_{eq}. Careful inspection of the figures suggests that this increase is due to the fact that the Volume of Fluid curves shift upwards as θ_{eq} is increased, while this shift (if any) is less pronounced for the long–wave curves. The dependence of Volume of Fluid results on θ_{eq} is consistent with [30].

3. Both models are more sensitive to variations of Λ than to those of θ_{eq}, again consistently with the asymptotic results [30].

3.3.1 Spreading of a Perfectly Wetting Drop

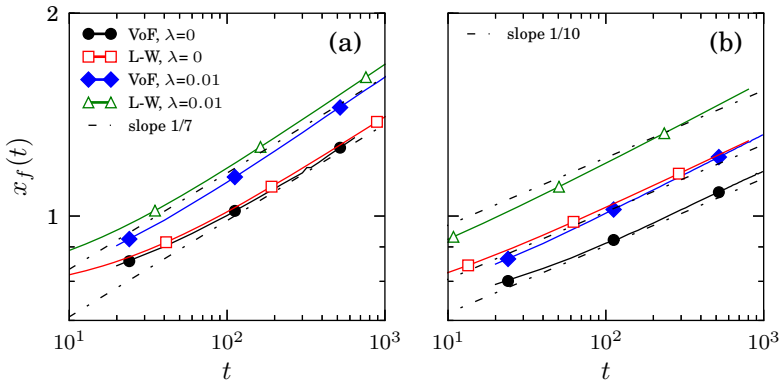

Figure 3.5 Front location as a function of time, $x_f(t)$, for a perfectly wetting drop ($\theta_{eq} = 0$) in long–wave and Volume of Fluid simulations: (a) planar case; (b) axisymmetric case. The dashed lines show the exponent, δ, predicted by Tanner's law for each case.

We carry out here a second comparison between Volume of Fluid and long–wave simulations now for perfectly wetting drops (i.e. $\theta_{eq} = 0$). Under no-slip condition, the spreading drops are expected to follow an intermediate asymptotic behavior [8] for large t represented by a self-similar thickness profile whose contact line position, x_f, obeys the Tanner's law [88],

$$x_f(t) = \xi_f t^{\delta} \tag{3.9}$$

Here, ξ_f is a coefficient related to the thickness profile, and $\delta = 1/(7 + 3d)$, so that we have $\delta = 1/7$ for a planar drop, and $\delta = 1/10$ for an axisymmetric one [22]. When slip is included, the flow is no longer strictly self-similar due to the addition of this new length scale to the problem [8]. However, it has been shown that this effect is not strong if Λ is much smaller than the average thickness of the drop, and a quasi self-similar solution can be obtained [42]. We will assume that this effect is negligible here at least for the time scales considered.

The simulations are performed using three different slip lengths ($\Lambda = 0,\ 0.01,\ 0.046875$) for both planar and axisymmetric drops. Here, we consider $\Lambda = 0$ in addition

to non-zero values so to be able to see clearly the influence of Λ on reaching the asymptotic regime described above. Considering $\Lambda = 0$ requires few adjustments in our computations which we now briefly describe. In the long–wave model, we simply put $\Lambda = 0$ in Eq. (3.4). Now the only additional length scale introduced in the problem is h_*; the results (weakly) depend on this quantity, as discussed in some details in an earlier work [25]. In Volume of Fluid simulations, a numerical slip on the order of the mesh size is always present, leading to a mesh-size prewetting layer ahead of the contact line when $\theta_{eq} = 0$. Clearly, this computational feature suggests that one may expect an influence of the numerical resolution on the results [70]; to optimize the computational cost, we limit the minimum mesh size to $1/2^8$ units. At this resolution, the effect of the mesh is found to be negligible on the results we present below. For the remainder of this section, we will calculate the front location for Volume of Fluid drops as the point of inflection of the fluid profile, rather than as the intersection of the reconstructed interface with the substrate.

Table 3.3 Exponents for the Power Law of the Front Position, $x_f(t)$, in the Perfectly Wetting Case ($\theta_{eq} = 0$). The Results are Given in Fractional Form to Help Comparison with the Tanner's law Exponent δ, 1/7 and 1/10, for the Planar and Axisymmetric Case, Respectively.

Case	δ_{VoF}	δ_{L-W}
Planar, slip 0.046875	1/6.0	1/6.0
Planar, slip 0.01	1/6.3	1/6.2
Planar, no-slip	1/6.2	1/6.6
Axisymmetric, slip 0.046875	1/7.2	1/7.7
Axisymmetric, slip 0.01	1/8.5	1/8.1
Axisymmetric, no-slip	1/9.4	1/9.0

Similarly to the calculations carried out for non-zero θ_{eq}, we start with drops of a given initial contact angle, θ_i, and let the drops spread freely. Figure 3.5 shows the front location as a function of time, $x_f(t)$. For clarity, we show in this figure the results for $\Lambda = 0,\ 0.01$ only. Dashed lines show profiles proportional to $t^{1/7}$ (Figure 3.5(a)) and $t^{1/10}$ (Figure 3.5(b)); the behavior of no-slip simulations is seen to agree with these powers reasonably well for large times. To go beyond visual comparison, we compute the value of δ in Eq. (3.9) from both models by a least squares fitting over a range of times when δ is approximately constant. Table 3.3 shows the values of δ obtained. The long–wave and Volume of Fluid calculations yield similar exponents for all slip lengths considered, and both show that δ decreases for smaller Λ, approaching the asymptotic values.

3.4 Collapse of Liquid Rings

As a final comparison, we consider the problem of a collapsing ring, motivated by our desire to consider a geometry that is more complex than the one of a drop, but that still allows for identifying clearly the differences between the models. In addition, we will use this problem to more explicitly demonstrate the influence of slip on the dynamics.

The ring is defined by its internal and external radii, r_{int} and r_{ext}, respectively, as well as by the radius, R, of its circular cross section. Thus, the liquid is initially inside the region described by

$$0 \leq y \leq -R\cos\theta + \sqrt{R^2 - (r - r_0)^2} \tag{3.10}$$

where $r_0 = (r_{ext} + r_{int})/2$ is the mean radius, $r^2 = x^2 + z^2$ with $r_{int}\cos\phi \leq x \leq r_{ext}\cos\phi$ and $r_{int}\sin\phi \leq y \leq r_{ext}\sin\phi$ $(0 < \phi < 2\pi)$, and θ is the contact angle.

The radius, R, is chosen to be the same as that in previously considered axisymmetric drops ($R \approx 3.5,\ 1.4,\ 0.8$, for $\theta_{eq} = 15°,\ 30°$, and $45°$, respectively),

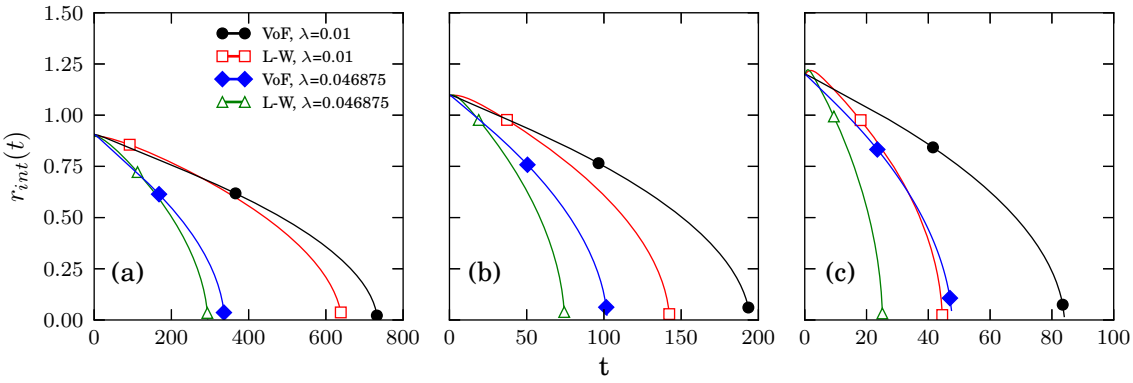

Figure 3.6 Inner radius, $r_{int}(t)$, for long–wave and Volume of Fluid simulations of a collapsing ring: (a) $\theta_{eq} = 15°$; (b) $\theta_{eq} = 30°$; (c) $\theta_{eq} = 45°$.

and the mean radius, r_0, is held constant at $r_0 = 1.8$. In our setup, we consider rings with equal initial contact angles, θ_i, at the internal and external radii, and both equal to the equilibrium angle for static axisymmetric drops, θ_{eq}. However, the ring is not in equilibrium since the curvatures, $1/r_{int}$ and $1/r_{ext}$, yield different capillary pressures which cannot be balanced by the same contact angle [39]. Consequently, the ring develops an inward flow which eventually leads to a collapse into a single central axisymmetric drop. In the present chapter we assume azimuthal symmetry and do not consider fully three dimensional features of the dynamics, which may lead to instabilities and breakup [39].

Figure 3.6 shows the time evolution of the inner radius of the ring for both Volume of Fluid and long–wave simulations. In particular, we will be interested in the time, τ, the collapse takes, defined as the time when the interior radius vanishes. Table 3.4 shows the resulting values of τ, together with the ratio between the results of the two models. We note that this ratio decreases for smaller θ_{eq}, suggesting that the both models predict increasingly similar dynamics for small contact angles. For large θ_{eq} there are, however, significant differences, as can be seen explicitly in Figure. 3.6(a)-(c). We point out that these differences in dynamics cannot be predicted based simply on the thickness profiles. To illustrate this point, Figure 3.7

Table 3.4 Ring Collapse Times, τ_{VoF} and τ_{L-W}, and the Ratio, τ_{VoF}/τ_{L-W}. The First Column Specifies the Equilibrium Contact Angle, θ_{eq}, and the Slip Length, Λ.

Case	τ_{VoF}	τ_{L-W}	τ_{VoF}/τ_{L-W}
15°, slip 0.01	733	641	1.1
15°, slip 0.046875	337	294	1.1
30°, slip 0.01	194	142	1.4
30°, slip 0.046875	102	74	1.4
45°, slip 0.01	84	44	1.9
45°, slip 0.046875	48	25	1.9

shows the profiles resulting from the two models at the times when the inner ring radii are at the same location (parts (a)-(b)), in addition to the equilibrium (long - time) result (part(c)). We see that the corresponding shapes barely differ, but still lead to considerably different dynamics.

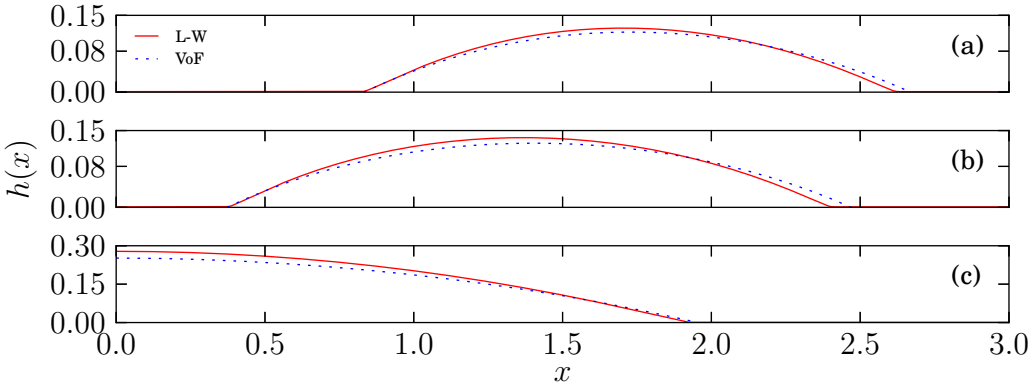

Figure 3.7 Ring profiles resulting from Volume of Fluid and long–wave simulations. (a) and (b) show the profiles at the times when the inner radii are at the same location for both models, and (c) shows the equilibrium solution.

Regarding the influence of slip length, note that Figure 3.6 shows that a smaller Λ leads to a larger collapse time, with slip playing a similar role in both models. Additional more precise observations can be made: for both Volume of Fluid and long–wave simulations, τ approximately halves when Λ increases by a factor close to four, viz. Table 3.4. This would suggest that a dependence $\tau \sim \Lambda^{-0.5}$ could be expected (see dashed line in Figure 8). In fact, a similar behavior is obtained when we consider the linear stability analysis (LSA) of a contracting ring within long–wave approach [39], by recalling that the collapse time, τ, can be related to the inverse of the growth rate for the azimuthally symmetric mode, ω_0. Figure 3.8 shows that the LSA predicts a dependence of τ on Λ that is not too far from what is found in simulations. The overestimate of τ computed using the LSA is as expected, since the presented estimate is based on the value of ω_0 computed at $t = 0$ and therefore does not include an increase of collapse speed as the ring decreases in size.

3.5 Numerical Validation

In our Volume of Fluid simulations, the solution was calculated on an adaptive mesh refined on the drop surface to a resolution of $\Delta = 1/2^8$, while parts of the domain far from the surface were refined to $1/2^4$. To test the convergence of the method, we present the case when the planar drop spreads from $\theta_i = 30^\circ$ to $\theta_{eq} = 15^\circ$. The average relative difference is calculated as

$$\mathrm{Avg}_\Delta = \frac{1}{t_{max}} \int_0^{t_{max}} \frac{|x_f(t) - x_{ref}(t)|}{x_{ref}(t)} dt$$

where x_{ref} is the drop radius computed with $\Delta = 1/2^8$, and x_f is computed with $\Delta = 1/2^5$, $1/2^6$, and $1/2^7$. We restrict our attention to a representative portion of the drop spreading, so that t_{max} is the time it takes for the drop radius to be within 1% of its equilibrium value, as computed using $\Delta = 1/2^8$. Figure 3.9 plots Avg_Δ and shows that mesh effects are negligible when compared to the drop radius.

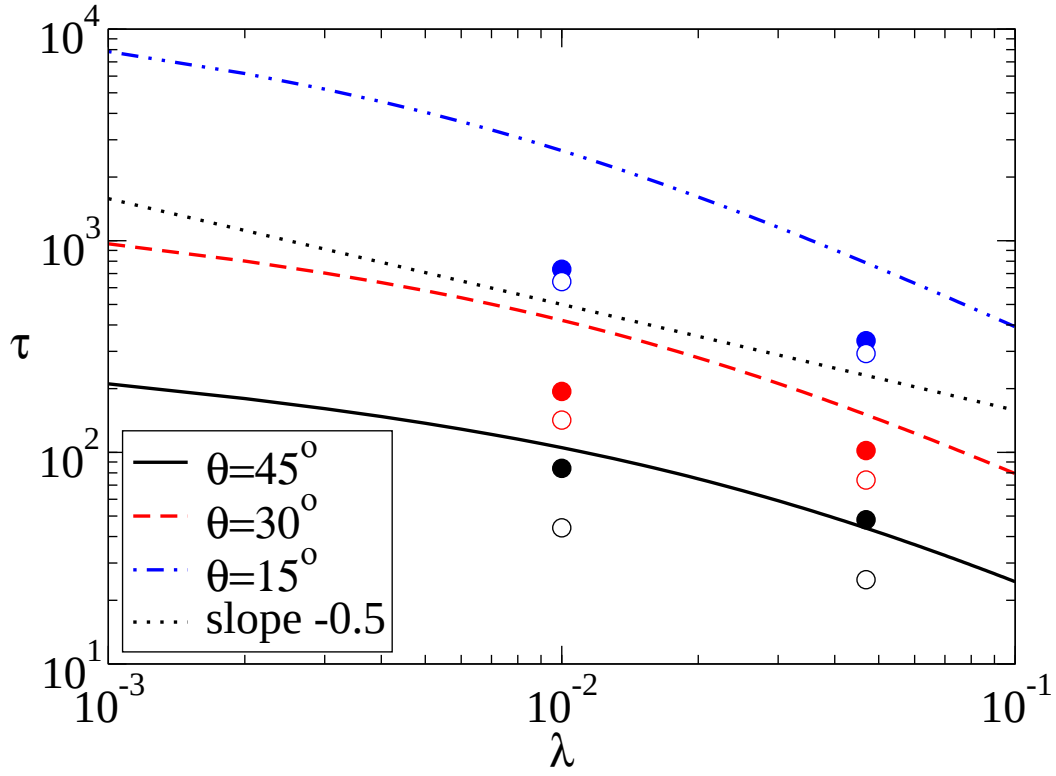

Figure 3.8 Collapse times, τ, of rings. Solid lines show the inverse of the growth rate, ω_0, of the azimuthally symmetric mode obtained from the linear stability analysis; filled/hollow circles show τ_{VoF} and τ_{L-W}, respectively.

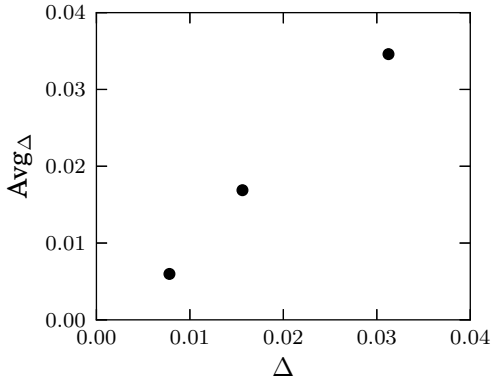

Figure 3.9 Relative error for planar spreading drop. The error is computed as the average relative difference between the front location compared to the one found using $\Delta = 1/2^8$.

Hocking and Rivers [46] derived an asymptotic solution for the radius of a spreading drop. In their derivation, the flow is governed by the Stokes equations, and the effects of gravity are ignored. Additionally, the condition on the solid substrate is assumed to be the Navier slip condition (see Eq. (2.4)), where the slip length is taken to be small relative to the drop size. No limitations on the contact angle are imposed. Their solution yields the following ordinary different equation (ODE) for the drop radius, x_f

$$2\frac{dx_{f_a}}{dt} = \frac{G(\theta) - G(\theta_{eq})}{\ln(x_f) - \ln(\Lambda) - Q_O(\theta) + Q_i(\theta_{eq})} \tag{3.11}$$

where

$$G(\theta) = \int_0^\theta \frac{\vartheta - \sin\vartheta\cos\vartheta}{\sin\vartheta} d\vartheta$$

The functions Q_O and Q_i were computed by interpolating Table 1 in [46]. The contact angle, θ, is related to the drop volume and front location through conservation of volume, so that Eq. (3.11) can be solved using standard ODE solvers.

We present the case of the axisymmetric drop spreading from 45° to 30°. In order for Eq. (3.11) to apply, the denominator must be greater than 0, so for our parameters we find the condition that $\Lambda \lesssim 0.03$. We thus choose $\Lambda = (0.028,\ 0.016,\ 0.008,\ 0.004)$.

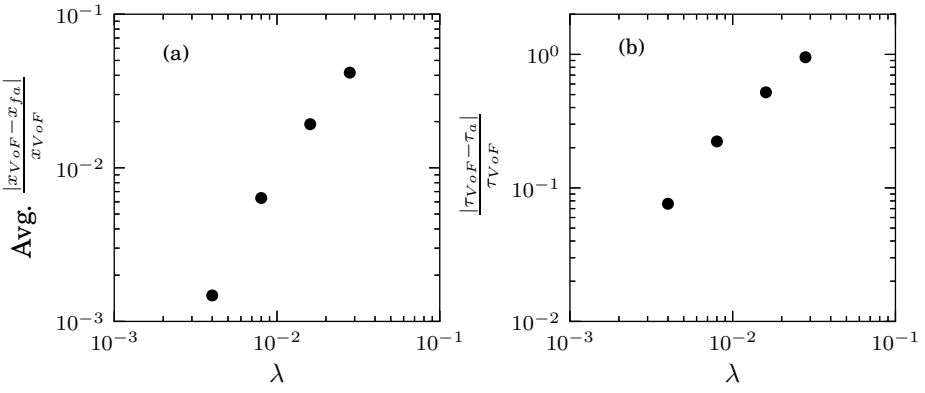

Figure 3.10 Comparison of Volume of Fluid simulations with asymptotic solution [46] for a drop spreading from 30° to 15° as a function of the slip length: (a) the average relative difference between the front locations; (b) the relative difference in spread times.

The drop radius was computed using the Volume of Fluid solver, $x_{f_{VoF}}$, and the asymptotic solution, x_{f_a}, for each slip length. The average relative difference between numerical and asymptotic solution was computed by the integration

$$\text{Avg}\frac{|x_{f_{VoF}} - x_{f_a}|}{x_{f_{VoF}}} = \frac{1}{t_{max}} \int_0^{t_{max}} \frac{|x_{f_{VoF}} - x_{f_a}|}{x_{f_{VoF}}} dt$$

where t_{max} is again chosen so that $x_{f_{VoF}}$ is within 1% of its equilibrium value. Note that the time it takes for the Volume of Fluid solution to reach equilibrium is Λ-dependent, so that the comparison is carried out over appropriate ranges for each Λ considered.

Figure 3.10(a) shows the relative difference between the two results. We see that the front locations agree well in the limit of small Λ. Another comparison that can be carried out involves considering the difference in the time scales. We compute the spread times as the time it takes the Volume of Fluid solution and the asymptotic solution to reach within 1% of the respective equilibrium values; denote these τ_{VoF} and τ_a. The relative difference between the two is computed as

$$|\tau_{VoF} - \tau_a|/\tau_{VoF}$$

Figure 3.10(b) shows the relative difference of the spread times. For larger Λ, the asymptotic solution predicts that a drop spreads much faster, compared to the simulation results. However, for small Λ, the difference in spreading times is less than 10% of τ_{VoF}, and on average the relative difference in the computed front locations is on the order of 10^{-3}.

To conclude, we find that the results of the simulations are fully converged for the grid resolutions implemented. Furthermore, the location of the front as a function of time agrees very well with existing asymptotic results for a spreading drop. The Volume of Fluid based solver thus allows for accurate simulations of contact angle driven spreading phenomena.

3.6 Conclusions

In this chapter, we report on a comparison between direct solutions of the Navier-Stokes equations computed using a Volume of Fluid method, and the long–wave based simulations. We consider two simple geometries, drops and rings, with the goal of avoiding complexities that are associated with more complicated geometries. To further facilitate the comparison, we consider the flow regime characterized by low Reynolds and capillary numbers, where long–wave theory is expected to apply, and implement Navier slip condition in both models with the same goal.

For partially wetting drops, characterized by non-zero equilibrium contact angle, θ_{eq}, the comparison is carried out by considering consistency with the asymptotic Cox-Voinov law. While in general our findings are as expected - that long–wave theory agrees well with the Volume of Fluid results and the Cox-Voinov law for small θ_{eq} - we also uncover additional features of the results, summarized here: (i) the deviations of long–wave results from the behavior expected based on the Cox-Voinov law and Volume of Fluid simulations is particularly strong for retracting drops, and in azimuthal geometry; (ii) the initial stages of spreading or retracting differ significantly

between the models, for all considered θ_{eq}; (iii) the degree of agreement between the two models is not influenced by the values assigned to the slip length, Λ - in other words, slip influences both models in a similar manner. To our knowledge, these findings have not been reported in the literature.

For perfectly wetting drops, with $\theta_{eq} = 0$, both models are found to agree well with the predictions of Tanner's law in the case of no-slip. Non-zero slip length modifies the results and introduces deviations from Tanner's law as expected; an important finding here is that the two models agree well with each other for non-vanishing slip.

When the two models are applied to collapse of a liquid ring, the results are found to be in good agreement for small θ_{eq}, while for larger θ_{eq}, the collapse time under long–wave simulations is as much as twice as fast relative to the one found using Volume of Fluid simulations. Again, the slip length has little effect on the degree of comparison of the two models.

While in this chapter we consider only a classical long–wave formulation, it would be of interest to explore whether the recently proposed improvements of this formulation (see, e.g., [79]), lead to significant differences. Additionally, in situations where the evolution of the liquid is more complex, the influence of the differences between the long–wave model and direct simulations is a topic which warrants further investigation.

CHAPTER 4

ON THE INFLUENCE OF INITIAL GEOMETRY ON THE EVOLUTION OF LIQUID FILAMENTS

4.1 Introduction

The long–wave model of Chapter 3 has been widely applied in the study of the breakup of liquid metallic nanofilms [54, 34]. As we discussed in Chapter 3 however, the long–wave model begins to show distinct weaknesses when the contact angle becomes $O(1)$; for the liquid metallic nanofilms in these experiments the contact angle is almost 90° [34]. In this chapter, we will discuss some particular initial geometries for nanofilms which appear to require full direct simulations in order to model. This requirement is due to the fact that the initial conditions which can be considered in experiments can be placed far from fluid equilibrium, and when this is combined with the properties of liquid metals implies nonvanishing inertial contributions.

Synthesis and assembly on the nano-scale is one of the most important goals of contemporary science and technology, see e.g. [33]. While there are a large number of examples involving a variety of different fluids where self and directed assembly is relevant, we focus here on one particular example which is finding important applications: nano-scale metallic particles. With metal films, a recently developed technique is the irradiation with laser pulses or electron-beams, leading to fast liquefaction. While in the liquid phase, the metal film becomes unstable and breaks up into drops which solidify and remain on the substrate as solid particles. The understanding of this instability development is the main focus of this paper.

One commonly considered geometry in the experiments is the one of a filament deposited on a solid substrate. In the context of metal films, a liquid filament itself does not even have to be deposited: it is sufficient to deposit a metal strip of a

rectangular cross section, liquefy it, and let the capillary forces drive the evolution. Such a setup has been recently demonstrated experimentally by [34], who consider a geometry consisting of long, thin, strips with thicknesses of tens of nanometers, widths of hundreds of nanometers, and lengths of tens of microns. When liquefied by laser pulses of typical duration of tens of nanoseconds, these strips quickly retract into filaments that then break up into drops, where the spacing of the drops is not uniform, but instead obeys a distribution consistent with the prediction of the classical Rayleigh–Plateau analysis. This mechanism of breakup can be explained surprisingly well by an analogy with the Rayleigh–Plateau analysis of the breakup of a free standing fluid jet, modified by the presence of substrate, as discussed in [54]. Following the analysis in [54], [34] show that varying the width of the deposited metal strip by a sinusoidal perturbation of a well defined wavelength can be used to produce an array of uniformly spaced particles, as long as this imposed wavelength is unstable, based on the Rayleigh–Plateau instability analysis. They show that perturbing by stable (short) wavelengths leads to distances between the particles that are nonuniform and not related to the imposed perturbation. In this paper, we explore whether one could overcome this limitation by appropriately choosing the initial fluid geometry.

Before discussing this question further, we outline briefly the basic framework determining the stability of liquid jets. The classical Rayleigh–Plateau linear stability analysis predicts that radial sinusoidal perturbations of a standing jet of radius R, with wavenumber $k = 2\pi/\lambda$, and small amplitude, grow or decay with the growth rate, ω, specified by

$$\omega^2 = \frac{\gamma}{\rho R^3}\left(kR(1-k^2R^2)\frac{I_1(kR)}{I_0(kR)}\right) \tag{4.1}$$

where γ is the surface tension, ρ the density, and I_0 and I_1 the modified Bessel functions [29, 69]. This result predicts a critical wavelength, λ_c, below which modes

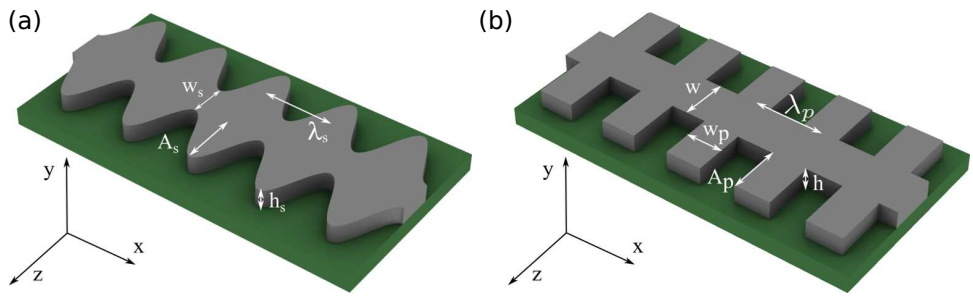

Figure 4.1 Two perturbation geometries for assembling arrays of nanoparticles: (a) sinusoidal initial geometry and (b) rectangular-wave initial geometry. The rectangular-wave geometry consists of a central strip of width w and height h; the perpendicular protrusions have an amplitude A_p, width w_p, and period λ_p.

are stable, as $2\pi R$. Rayleigh [69] derived the growth rate when the effects of viscosity are ignored; we should note, however, that the critical wavenumber predicted based on the Rayleigh–Plateau analysis remains unchanged when considering viscous effects [26]. We also note that Eq. (4.1) applies to small amplitude varicose modes of any waveform, as these can be decomposed into sinusoidal component modes via a Fourier transform.

The presence of a substrate naturally modifies Eq. (4.1). Viscous and viscointertial limits of the dispersion relation for a filament on a substrate are derived by [13]. The LSA based on long–wave theory demonstrates that λ_c is modified only slightly by the presence of the substrate, showing a weak dependence on the contact angle (the angle at which the interface between the liquid phase and an ambient phase, such as a surrounding vapor, meets a solid surface) [54, 34, 19, 21]. Several methods for calculating λ_c for a filament on a substrate are compared in [21]; importantly, for a contact angle of $\pi/2$, the critical wavelength remains exactly the same as that predicted by the Rayleigh–Plateau analysis.

As mentioned above, the Rayleigh–Plateau driven breakup limits how closely spaced particles can be based on the critical wavelength. To overcome this limitation, in an experimentally focused study, [72] introduce a rectangular-wave type perturbation form. The initial geometry consists of a central strip of width w and

height h, to which perpendicular protrusions are attached, with amplitude A_p, width w_p, and period λ_p, as illustrated in Figure 4.1 (b). Such a structure can be compared with a strip whose cross sectional area is given by

$$\Omega_{eff} = h(w + 2A_p w_p/\lambda_p) = \Omega_0 + 2A_p h w_p/\lambda_p$$

where Ω_0 is the cross sectional area of the main strip (without protrusions), and Ω_{eff} is the average cross sectional area obtained when the total amount of liquid (including protrusions) is distributed evenly over a wavelength λ_p. We call Ω_{eff} an effective cross sectional area. In [72], this rectangular-wave type of geometry is found to lead to a one-dimensional array of particles spaced by λ_p/p, for $p \geq 1$.

The focus of this chapter is to use computational tools to uncover the influence of the initial geometry on the instability development. While our results are general and apply to any setup such that the initial geometry can be controlled, for definitiveness we chose relevant length and time scales as well as material parameters corresponding to metal filaments of nano-scale thickness, as in [72]. We computationally investigate the effects of varying parameters on conditions for which the breakup occurs and demonstrate that not only is it possible to destabilize the structure when $\lambda_p < \lambda_c(\Omega_{eff})$, but it is also possible to destabilize a structure when $\lambda_p < \lambda_c(\Omega_0)$. That is, despite the additional liquid added into the system by the protrusions, we can actually induce the strip to break up with a period less than its own critical wavelength, leading, as a final outcome, to particles spaced much closer than that would appear possible by considering the Rayleigh–Plateau predictions. This finding is surprising and also potentially very useful, since in many applications, it is desirable to have closely spaced particles [62]. Our results show that nonlinear effects are crucial in determining the size and spacing of the final drops.

The rest of this chapter is organized as follows. In Section 4.2, we outline the simulation setup. The results are given in Section 4.3, including description

of the basic instability mechanism, classification of various end states uncovered by the simulations, and dependence of the results on the parameters defining the perturbations. In Section 4.4, we discuss in more details some crucial aspects of the instability mechanism. The conclusions and the outline of future work are presented in Section 4.5.

4.2 Setup

Figure 4.1 (b) shows our initial geometry, which is a flat strip with a rectangular-wave edge perturbation similar to the one considered by [72]. The geometry consists of what we refer to as a 'central strip' defined by

$$\{(x, y, z)|\ y < h,\ z < w/2\}$$

and 'protrusions' defined by

$$\{(x, y, z)|\ y < h,\ |z| < (w/2 + A_p),\ |x - n\lambda_p| < w_p/2, \text{ for } n \in \mathbb{Z}\}$$

Throughout this chapter, we take the central strip to be specified by $h = 10$ nm and $w = 100$ nm. As described above, experimental studies begin by depositing metal in prescribed geometries such as a strip with an edge perturbation, and then liquefying these structures with laser pulses. While in the experiments the metal geometries may be going through repeated melting and solidification, in this study we neglect the effects of phase change, and furthermore assume that temperature variation of material parameters (viscosity, density, surface tension) is not crucial for the purpose of understanding the main mechanisms leading to instability. In addition to the experimental evidence discussed below, these approximations are motivated by our desire to focus on the influence of the initial geometry on instability development in a general setting. In the particular case of laser-irradiated metals, thermal simulations [34] suggest that the phase change itself happens on a very fast

time scale. A simplified model addressed by [90] also indicates that the heating of nanometallic films takes place rapidly, leading to a sharp, short lived peak in the temperature. In the present study, we are essentially assuming that during the time metal is in liquid phase we can ignore temperature variations. This approach is supported further by the fact that the constant temperature model has generally been very successful in modeling the breakup of nanometallic films [34, 54, 72]. With these simplifications, the evolution of the initial structure is thus governed by the Navier–Stokes equations for an isothermal fluid. We consider an initial geometry that is far from equilibrium, and rapidly evolves to what we refer to as its 'end state'.

As discussed in more detail below, the computational solver we use requires the presence of two fluids, and therefore we consider two phases that are immiscible and incompressible, separated by an interface: metal in its liquid phase, and the ambient phase. The governing equations under these assumptions become the two-phase Navier-Stokes equations We model this system by means of two phases: the liquid phase represents the liquid metal, and the vapor phase is an ambient phase which is taken to be insignificant. The governing equations are the dimensional Navier-Stokes equations, Eq. (2.1)-(2.2), For our simulations, we use the physical values of liquid nickel (Ni) used in [72], so that $\rho_l = 7905$ Kg/m^3, $\mu_l = 0.0047$ Pa·s, and $\gamma = 1.781$ N/m. The values of μ_v and ρ_v are chosen to minimize the effects of the ambient phase; we discuss these values further when the numerical methods are described. We note that Eq. (2.1) does not include the effects of the disjoining pressure. Previous models of similar problems, based on long–wave theory, included the disjoining pressure to model partial wetting and the linear stability of the interface, as discussed by [54]. In this chapter, partial wetting is introduced by the method described for 3D in Chapter 2. Furthermore, we expect that the interfacial instability due to the disjoining pressure effects is weak compared to other effects; a rough estimate shows that the breakup time of a uniform 10 nm film by the

disjoining pressure is considerably longer than the evolution time of the structures we consider here (see the linear stability analysis in [24]). Our current model and computational methods were previously shown to result in good qualitative agreement when compared to the experimental results in [72].

On the solid substrate, we impose the Navier slip boundary condition given by Eq. (2.4). Experimental results for various fluids and substrates have generally reported significant slip on surfaces with large contact angles [16], with a range of possible slip lengths depending on the surface topography and chemistry [65]. Often, a slip length on the order of 100 nm is reported for systems with contact angles ranging from 95° to 105° [16, 53, 65]. [3] also show that the slip is large in the present system by comparing the Navier-Stokes solutions with molecular dynamics simulations of nano-scale metal films by [37]. In this chapter, we briefly survey the effects of varying slip, but unless noted otherwise, we take $\Lambda = 60$ nm. This particular value of slip length is motivated by the work of [72], where good agreement between the simulation results and the experimental data was obtained for this value of Λ. We also set the contact angle to 90° for all the results, since this simplifies the numerical implementation considerably. We note that in a previous study, very good agreement with experiments was found when using this value of contact angle in the simulations [72]. Furthermore, similar experiments reported in [34] show an equilibrium contact angle of 88°, very close to the value used in this chapter.

To present the considered model in a more general setting, we rewrite Eq. (2.1)-(2.2) in a dimensionless form. We take the scales as $L = w = 100$ nm, and $\mathcal{T} = 1$ ns, based on the typical in plane dimensions and the observed retraction times. We

define the following dimensionless quantities

$$\begin{aligned} \tilde{\mathbf{x}} &= \frac{\mathbf{x}}{L} & \tilde{t} &= \frac{t}{\mathcal{T}} \\ \tilde{\rho} &= \frac{\rho}{\rho_l} & \tilde{\mu} &= \frac{\mu}{\mu_l} \\ \tilde{\mathbf{u}} &= \frac{L}{\mathcal{T}}\mathbf{u} & \tilde{p} &= \frac{\mathcal{T}}{\mu_l}p \\ \tilde{\kappa} &= \kappa L & \tilde{\delta_s} &= \delta_s L \\ \mathrm{Re} &= \frac{\rho_l L^2}{\mu_l \mathcal{T}} & \mathrm{Ca} &= \frac{\mu_l L}{\gamma \mathcal{T}} \end{aligned}$$

With these scales, our dimensionless equations are

$$\mathrm{Re}\,\tilde{\rho}\left(\partial_{\tilde{t}}\tilde{\mathbf{u}} + \tilde{\mathbf{u}}\cdot\tilde{\nabla}\tilde{\mathbf{u}}\right) = -\tilde{\nabla}\tilde{p} + \tilde{\nabla}\cdot\left(\tilde{\mu}\left(\tilde{\nabla}\tilde{\mathbf{u}} + \tilde{\nabla}\tilde{\mathbf{u}}^T\right)\right) + \mathrm{Ca}^{-1}\tilde{\kappa}\tilde{\delta_s}\mathbf{n} \tag{4.2}$$

$$\tilde{\nabla}\cdot\tilde{\mathbf{u}} = 0 \tag{4.3}$$

For our choice of parameters, the Reynolds number and capillary number are, respectively, $\mathrm{Re} \approx 16.8$, $\mathrm{Ca} \approx 0.26$, so the evolution takes place in a regime with a moderate dominance of inertial and surface tension effects over viscosity. The relevance of inertial effects, as well as the fact that contact angles involved are large, support the use of the direct numerical modeling as described next.

We directly solve the Navier-Stokes equations using Gerris. Spatial discretization is carried out using an adaptive octree; our adaptive mesh resolves the interface at a resolution of approximately 1 nm, and regions of high curvature are resolved to approximately 0.5 nm. The simulations that we present in Section 4.3-4.4 are insensitive to any further refinements in the mesh. In order to minimize the effect of the ambient phase, we set $\mu_v = 0.01\mu_l$ and $\rho_v = 0.2\rho_l$. This choice of ρ_v is a compromise between minimizing the influence of the ambient fluid and the computational cost of having very large differences between the ρ_l and ρ_v. For all the computations, we only simulate a half of the period due to symmetry, so that $0 \leq x \leq \lambda_p/2$. Simulations with a computational domain of a full period were run for

selected cases, and no difference was observed when compared with the half period simulations. In subsequent figures, we will often mirror the domain when we plot the simulations results, so that one or more periods are visible.

The partial wetting of Ni on the silicon dioxide (SiO_2) substrate is modeled by imposing a mirror condition on T, equivalent to a 90° contact angle. The limitation of imposing a 90° contact angle is not intrinsic to the Volume of Fluid method [2], however the numerical implementation of this contact angle is considerably simpler (and also arbitrary contact angles are not currently implemented in Gerris). Since the contact angle in the experiments [72] is very close (88°), the use of this simplification is well justified.

When a long strip of width $w = 100$ nm and height $h = 10$ nm is placed on a surface, it rapidly retracts to a half cylinder, which we call a filament, of radius $r_0 = \sqrt{2wh/\pi} \approx 25$ nm; we remind the reader that this value of r_0 remains constant throughout this chapter, since it describes the radius of the half cylinder corresponding to the central strip alone (without perturbation). Eq. (4.1) therefore predicts that the critical wavelength of the central strip is approximately 160 nm. This result is consistent with the Volume of Fluid simulations; we find that a half-cylindrical filament of radius r_0 is unstable when perturbed by a sinusoidal mode of small amplitude and a wavelength greater than approximately 160 nm, and stable for smaller perturbation wavelengths. This result is insensitive to the slip length Λ; we tested the critical wavelength of such filaments with $\Lambda = 10$ nm, $\Lambda = 60$ nm, and a free slip boundary condition (equivalent to $\Lambda \to \infty$ limit, and also to a standing jet), and found the critical wavelength to be the same to an accuracy of about 1%. We therefore use Eq. (4.1) to calculate the critical wavelength for filaments throughout this chapter. While Eq. (4.1) strictly applies only to small perturbations, we will show below that at least in the present setting it also describes stability of sinusoidal perturbations, even if they are not small.

4.3 Results

We first investigate the case $\lambda_p = 150$ nm, below the critical wavelength, $\lambda_c = 2\pi r_0 \approx 160$ nm, which is predicted by the Rayleigh–Plateau analysis for the central strip. Figure 4.2 (a) shows the breakup for $A_p = 110$ nm and $w_p = 75$ nm. The cross section shows the pressure distribution in the liquid as it breaks up. The initially imposed shape quickly evolves, resulting in a low pressure bulge at the protrusion centers, $(x, z) = (n\lambda_p, 0)$, adjacent to which are higher pressure areas on all sides ($t = 0.5$ ns). As the protrusions collapse, the bulge accumulates more liquid, while higher pressure necks form between the bulges, $(x, z) = (n + 1/2)\lambda_p$ ($t = 1.0$ ns); we note that at this point, the protrusions have collapsed to introduce a perturbation with considerable negative curvature at the necks; in the present case the forces leading to breakup overpower this stabilizing curvature. Eventually the necks pinch off ($t = 1.5$ ns), and the bulges form separate drops with a center to center spacing equal to λ_p, with each drop containing all of the liquid per λ_p ($t = 10$ ns).

We can contrast the described evolution with the one of a sinusoidal shape perturbation, with the same λ_p and total liquid volume. Figure 4.2 (b) shows the results at same times as shown in Figure 4.2 (a). For sinusoidal perturbations, the evolution follows a similar path initially, with the protrusions retracting towards the central strip, and the half-cylindrical necks forming between the bulges centered on $(x, z) = (n\lambda_p, 0)$. However, we see that the pressure gradient is smaller between the bulges and the adjacent portions of the structure ($t = 0.5$ ns). The protrusions collapse more quickly, resulting in a structure resembling a half-cylindrical filament perturbed by a large amplitude sinusoidal perturbation of wavelength λ_p ($t = 1$ ns). Ultimately, the mode decays, and the end state is a filament, as one would expect based on the Rayleigh–Plateau stability predictions.

We can make a few broad rationalizations of the origin of the difference between the results obtained using sinusoidal and rectangular-wave perturbations. First, we

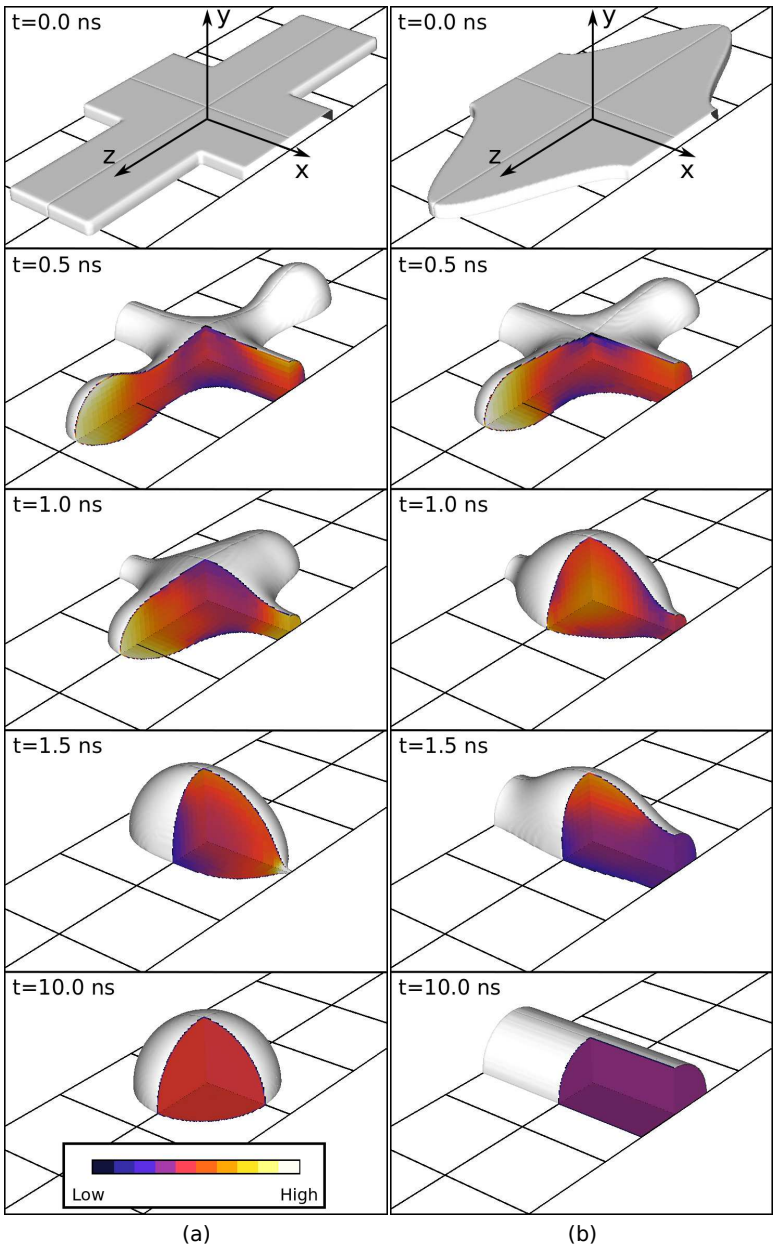

Figure 4.2 Time evolution and the pressure distribution for the rectangular-wave and sinusoidal geometries with a perturbation wavelength of 150 nm: (a) rectangular-wave perturbed strip with $A_p = 110$ nm, $w_p = 75$ nm (see also Movie (2) in Supplementary Material) and (b) sinusoidally perturbed strip of the same volume as in (a) with $w_s = 100$ nm, $A_s = 110$ nm; see Figure 4.1 for the definition of all geometric quantities. Each box is 75 nm by 75 nm, and the pressure scale is the same for both figures.

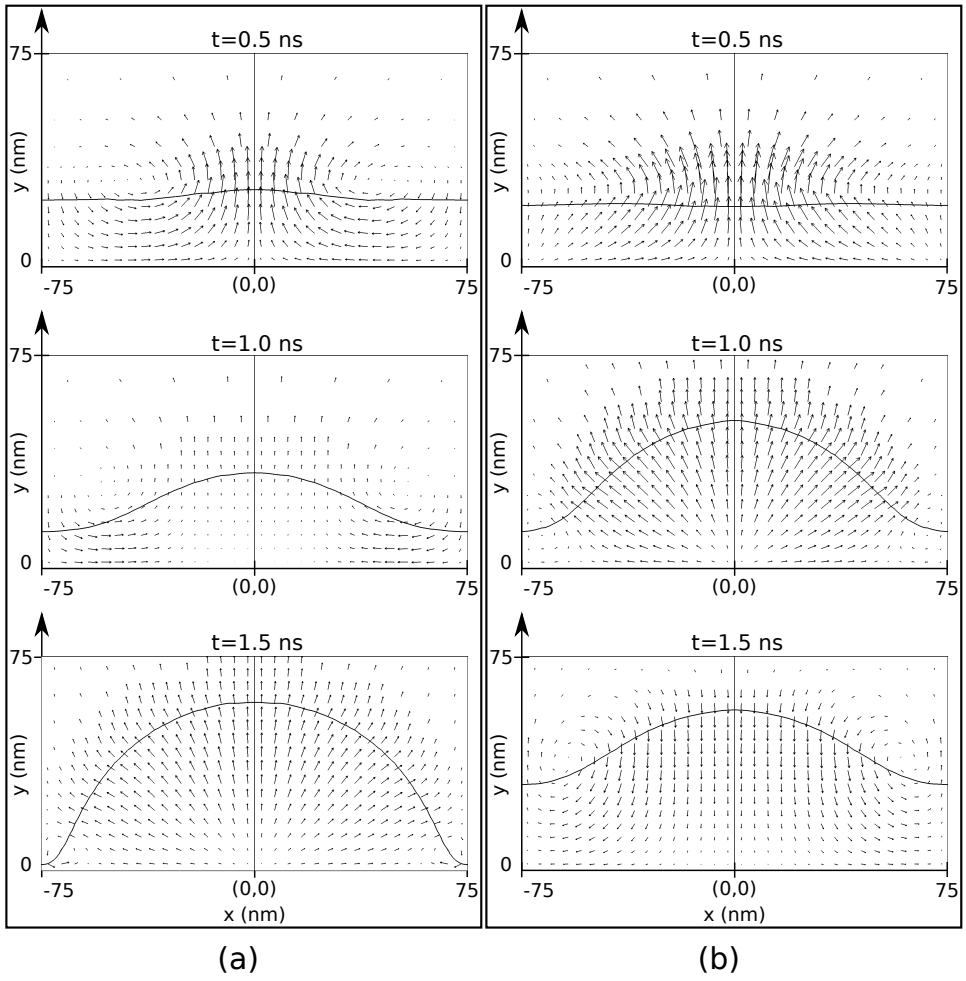

Figure 4.3 Time evolution of the velocity field in the $z = 0$ plane for times $t = 0.5$, 1.0, and 1.5 ns, for (a) the rectangular-wave, and (b) sinusoidal geometries. The respective parameters are the same as in Figure 4.2. The solid curve shows the interface. The arrows show the velocity in both the liquid and ambient phases.

observe that the protrusion collapses more slowly for the rectangular-wave geometry, as the liquid is distributed evenly along the protrusion, sustaining a lower relative pressure in the bulge (compare $t = 1$ ns results in both cases). However, even before the protrusion collapses, we see in Figure 4.2 that at 0.5 ns, there is a relatively higher pressure near $x = (n + 1/2)\lambda_p$. We conjecture that the difference between the evolution of the two considered geometries is due to the different initial curvatures, and consequently Laplace pressures, at $x = (n + 1/2)\lambda_p$. Ignoring the effects of viscosity, the Laplace pressure gives the pressure jump across the interface as $\gamma\kappa$. For the rectangular-wave geometry, the initial curvature in the x-z plane is zero at the midpoint between the protrusions; however, the sinusoidal geometry leads to a negative curvature in the x-z plane, and therefore to a decrease in the Laplace pressure, stabilizing the strip.

In addition to the rectangular waveform perturbation, we have considered the breakup of other initial configurations, which we mention here only briefly. We find that triangle waveform patterns (with a base attached to the central filament) break up similarly to sinusoidal type geometries and so do not display the richness of behavior as the rectangular waveform perturbation. If a vertex of a triangular perturbation is connected to a filament, a breakup occurs at the vertex, without influencing stability of the filament. Therefore, it appears that a rectangular waveform perturbation is the most obvious one if the goal is to modify the stability properties of the central filament.

Figure 4.3 plots the velocity field of each geometry from Figure 4.2 in the plane $z = 0$, for $x \in (-\lambda_p/2, \lambda_p/2)$, where again $\lambda_p = 75$ nm. For the rectangular-wave geometry (Figure 4.3 (a)), at $t = 0.5$ ns, a vortex has developed at the interface approximately midway between the origin and the centers of the necks, draining the liquid away from $x = \pm 75$ nm and into the low pressure bulge centered at $x = 0$. This trend continues for $t = 1.0$ ns, with the velocity being comparatively small outside

of the necks. For $t = 1.5$ ns, the necks have almost completely vanished; however small vortices near $x = \pm 75$ nm continue to drive the flow out of the neck regions until rupture occurs. Meanwhile, for the sinusoidal geometry (Figure 4.3 (b)), at $t = 0.5$, the vortex that is seen for rectangular-wave geometry is not observed; while a small component of the velocity field towards $x = 0$ is present, the overall trend is predominantly in the positive y-direction. The difference between the rectangular-wave and the sinusoidal geometry is more stark for $t = 1.0$ ns, where the bulge that has developed at $x = 0$ is expanding along the x-axis, while the velocity is relatively small near $x = \pm 75$ nm. At $t = 1.5$ ns, the sinusoidal geometry shows a velocity field directed in the negative y-direction, and away from $x = 0$, so that the system is relaxing to a cylindrical geometry.

Next, we consider the evolution of the rectangular-wave structure when varying the size of the protrusions. Figure 4.4 shows the structures characterized by the same dimensions as in Figure 4.2, except that in Figure 4.4 (a), $A_p = 100$ nm, and in Figure 4.4 (b), $A_p = 300$ nm. When A_p is too small, the structure does not break up, meaning that there is a critical amplitude, A_c, below which breakup does not occur. For small A_p, the protrusions collapse too quickly, so that the low pressure region in the junction is not sustained long enough for breakup to occur. The existence of A_c is consistent with the Rayleigh-Plateau stability predictions, since for sufficiently small A_p, linear stability should hold independently of the perturbation shape. On the other hand, when A_p is sufficiently large, a secondary breakup occurs, such that the protrusions form separate side-drops that then recoalesce to form central drops at $x = n\lambda_p$. A similar situation is observed in experiments [72]. We note (and discuss further below) that for very large A_p, a set of side drops form as the particles do not recoalesce, similar to the two-dimensional array of end drops observed in [72] (see also Movies (1) and (3) in Supplementary Material). A more complete discussion of possible breakup mechanisms is given next; as we will see, there is still a more diverse

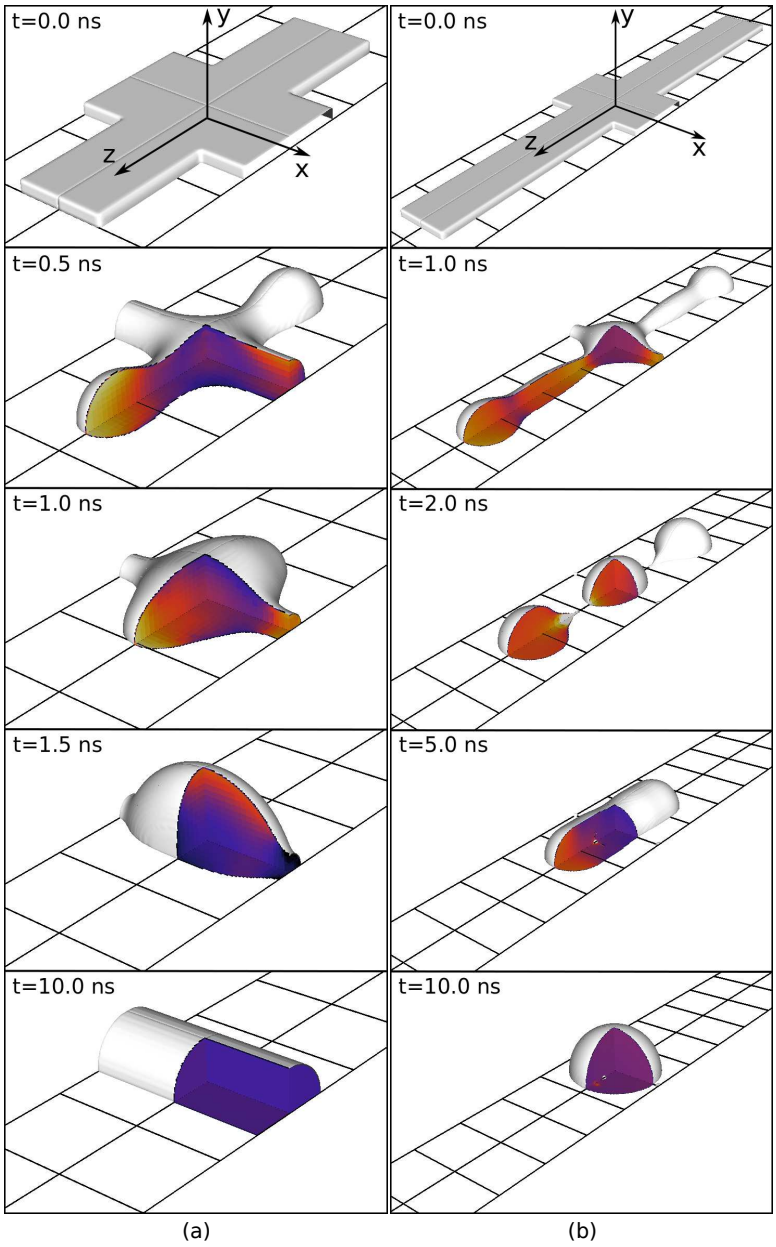

Figure 4.4 Time evolution and the pressure distribution for $\lambda_p = 150$ nm, $w_p = 75$ nm, showing a stable case and a case with secondary protrusion breakup: (a) $A_p = 100$ nm, and (b) $A_p = 300$ nm. Each box is 75 nm by 75 nm, and the pressure scale is the same as in Figure 4.2. Movies (1) and (3) in the Supplementary Material show (a) and (b), respectively.

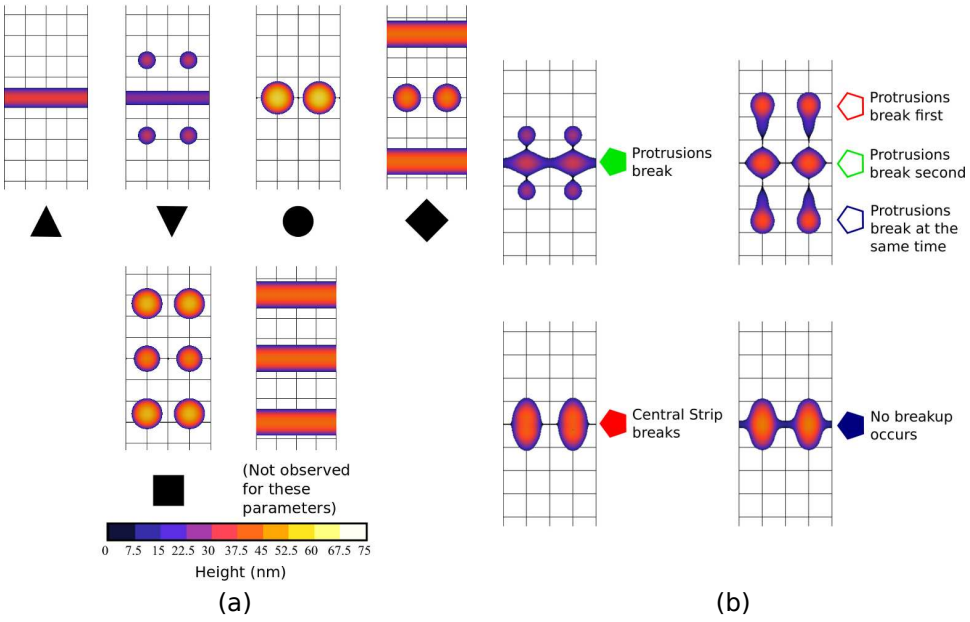

Figure 4.5 (a) Classification of end states resulting from the relaxation of the rectangular-wave geometry defined in Figure 4.1 (b). Each symbol below a sketch of a possible end state is used in the following figures to show that this particular end state is observed. The end state consisting of three parallel filaments is not observed for the parameters considered and is included for completeness. (b) Classification of dynamics. Filled symbols show the cases when either the protrusion breaks, the central strip breaks, or no breakup occurs at any time, and the color of each indicates which of these cases is observed. Hollow symbols show cases when both the central strip and the protrusions of the rectangular-wave break up, and the color shows the order of the breakup scenarios.

range of end states to be described. Animations demonstrating some of the possible dynamics and end states for the rectangular waveform perturbation are presented in Supplementary Material. For now, it is important to emphasize the most interesting point: although perturbations add to the total volume and may therefore be expected to stabilize short wavelengths, their influence may be opposite, leading actually to *instability* at perturbation wavelengths that would be expected to be stable based on the classical Rayleigh–Plateau prediction.

4.3.1 Parametric Dependence

In this section, we explore the dependence of the dynamics on the parameters A_p, w_p, and λ_p. To reduce the number of parameters, unless otherwise noted, we fix $\Lambda = 60$ nm, as well as $w = 100$ nm and $h = 10$ nm.

Figure 4.5 classifies the dependence of the breakup process on w_p and A_p for two wavelengths, λ_p. Figure 4.5 (a) shows the observed end configurations. As shown, a diverse range of end states can be achieved by harnessing this initial geometry. The one-dimensional arrays (circle) and arrays with side drops (square), as also observed in [72], are accompanied by additional configurations such as a filament (triangle), a filament with side drops (inverted triangle), and a one-dimensional array with side filaments (diamond). Although not observed for these parameters, a sixth state, consisting of three parallel filaments, is also possible. We note that within the considered framework, any resulting filaments ultimately should destabilize due to the Rayleigh–Plateau instability mechanism, and an array of drops should form with a distribution according to the prediction of the Rayleigh–Plateau analysis as discussed in [54]. However, this subsequent breakup takes place significantly later than the formation of the filament; Eq. (4.1) suggests that a filament resulting from, say, $A_p = 110$ nm, $\lambda_p = 150$ nm, $w_p = 75$ nm, would take nearly twice as long to break up when compared to the time the filament would take to form (2 ns versus 4.5 ns), and this second phase of the evolution is not considered in this chapter. In the context of liquid metal films, that are in liquid state for a short time, any state discussed here may as well be the final outcome.

Figure 4.5 (b) shows the relevant dynamics of the breakup; our goal is to classify what type of breakup occurs, during any point in the evolution of the structure, even if later on, there is recoalescence. We classify the evolution of this system according to whether the protrusions and/or the central strip break up, and the order in which the breakup occurs. Hollow symbols show that both the protrusion and the central strip

rupture, and the color corresponds to whether the protrusions break off before the central strip ruptures (red symbols), after the central strip ruptures (green symbols), or at approximately the same time as the central strip ruptures (blue symbols). All other cases are shown using filled symbols: blue indicates that no breakup occurs at any time during the relaxation, red that only the protrusions break off, and green that only the central strip ruptures. These breakup scenarios may be followed by a secondary recoalescence of drops to produce the static states discussed above. The end state is not independent of the dynamics; for example, when the end state includes side drops and side filaments, indicated by an inverted triangle, a square, and a diamond in Figure 4.5 (a), this must be accompanied by the protrusions breaking off (filled green, hollow red, hollow green, and hollow blue symbols in Figure 4.5). We find that decoupling the classification of the end states and dynamics will more effectively facilitate discussion of the parametric dependence.

Figure 4.6 (a) summarizes the possible static and dynamic states for $\lambda_p = 150$ nm. Let us first consider an intermediate range of w_p for which a breakup occurs. Within this range, we find that there is a critical amplitude, A_c, below which there will be no breakup and the end state is a filament, and above which the central strip will rupture at some point, as indicated by the color. We find that this critical value, A_c, is about 110 nm for larger values of w_p, and it increases to between 150 and 200 nm as w_p decreases. However, once A_p is above this critical value, there is no further effect on the stability of the central strip. That is, once A_p is sufficiently large, any further increase does not affect whether or not the central strip breaks up at some point in time. For w_p between 65 nm and 95 nm, side drops form when $A_p = 500$ nm; for small w_p ($25 \text{ nm} \lesssim w_p \lesssim 45$ nm), side drops form for smaller A_p, although the strip does not rupture for $w_p = 25$ nm. For large A_p, if side drops do not form, the protrusions introduce a large amount of excess liquid which may prevent

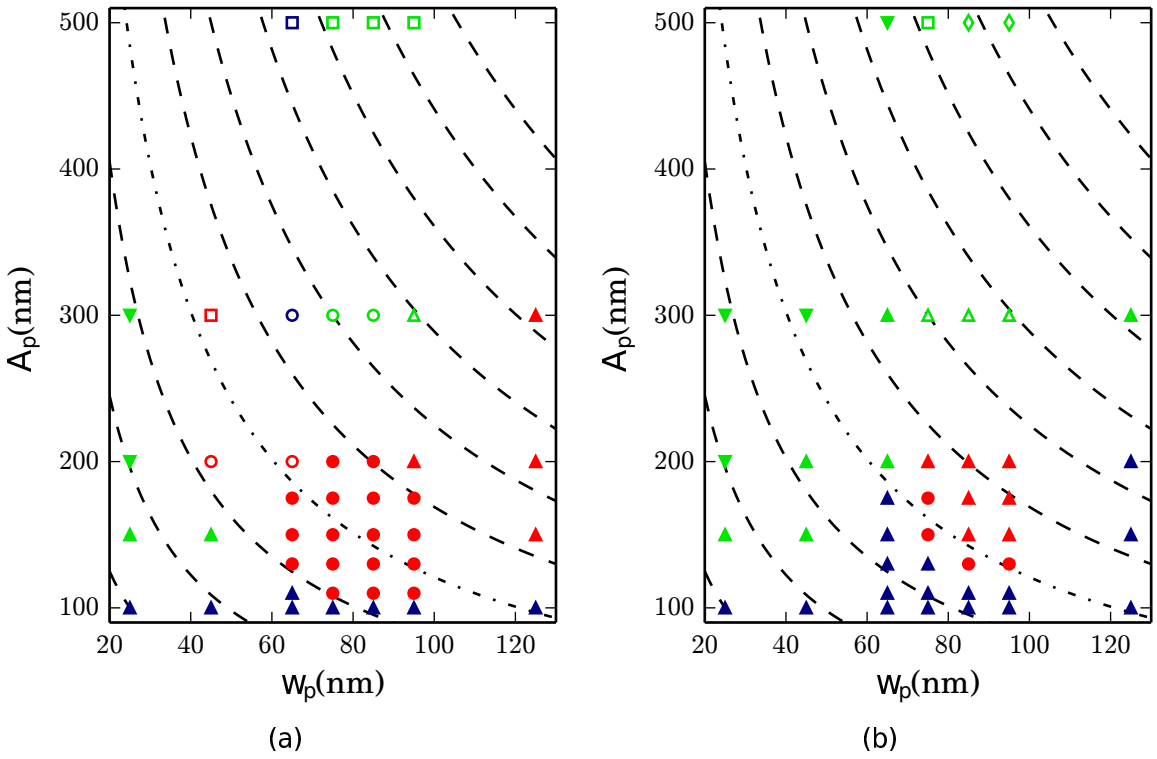

Figure 4.6 Phase plots classifying the dynamics and end states for the relaxation of the geometry shown in Figure 4.1 (b), for two values of λ_p. The symbols shape gives the end state produced by the breakup (Figure 4.5 (a)), while the symbol color classifies the dynamics (Figure 4.5 (b)). (a) $\lambda_p = 150$ nm and (b) $\lambda_p = 130$ nm. The dashed curves show constant effective cross sectional area, Ω_{eff}. The area increases from bottom left to top right.

the formation of a central array, even though the central strip does break up (see for example $w_p = 95$ nm, $A_p = 200$ nm and 300 nm).

The stability of the central strip is also affected by the protrusion width, w_p. For small w_p, such as 25 nm shown in Figure 4.6 (a), the central filament remains stable for all values of A_p, and the protrusions may either not break at all for small A_p, break off and coalesce for larger A_p, or break off and remain separated for even larger values of A_p. For larger w_p (greater than about 45 nm), there exists a critical amplitude, A_c, such that the central filament ruptures. It is interesting to note that for $w_p = 45$ nm and A_p large, the protrusion breaks off first, yet the central strip still ruptures. This may seem counterintuitive, as the protrusions drive the breakup of the central strip. However, in these cases, the time at which the protrusions break is comparable to the time when the central strip breaks, indicating that a sufficiently large perturbation is still imparted to the strip that breakup could occur even in the absence of the protrusion. For very large w_p, such as $w_p = 125$ nm, the central filament remains stable; for large values of A_p, the protrusions break off from the filament at some point of the evolution, but eventually recoalesce.

Figure 4.6 (b) shows the corresponding results for $\lambda_p = 130$ nm. For this smaller λ_p, a much narrower range of parameters allows for the formation of arrays of drops. Instead, we most often find either a filament of liquid, or a filament with side drops. To explain this, first note that for the same value of A_p and w_p, there is a larger effective area, Ω_{eff}, for $\lambda_p = 130$ nm than for $\lambda_p = 150$ nm. Larger Ω_{eff} implies that any drops resulting from breakup will not only be more closely spaced due to the smaller value of λ_p, but also larger in radius, which will tend to lead to recoalescence. Second, as the structure begins its retraction, smaller λ_p implies a larger negative curvature in the x-z plane at $x = (n+1/2)\lambda_p$, which will tend to stabilize the structure. When the central strip does rupture at some point during the retraction, increasing A_p to 500 nm, for large enough w_p, leads to the unique case of a one-dimensional array of drops

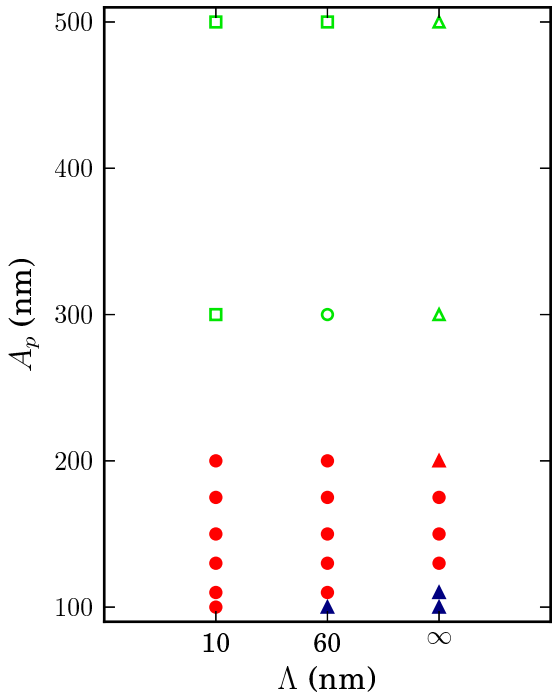

Figure 4.7 Parametric dependence on the slip length Λ for Λ = 10 nm, 60 nm, and ∞ (free slip condition). Symbols and colors indicate the same static states and dynamics as in Figure 4.5. The parameters λ_p and w_p are fixed at 150 nm and 75 nm, respectively.

with side filaments on either side, as the large amount of liquid and narrower spacing leads to the coalescence of the side drops produced by the protrusions breaking off. We note that in addition to λ_p = 130 nm, we also considered λ_p = 110 nm, but for such a small λ we did not find breakup of the central strip for any combination of protrusion parameters. Also, geometries characterized by larger values of λ_p are considered numerically and experimentally in [72]; drops resulting from the breakup of large λ_p geometries tend not to recoalesce, leading to arrays of drops with spacing exactly equal to λ_p, and as λ_p is increased further, further drops may form leading to arrays with spacing of $\lambda_p/2$ or smaller.

Finally, we briefly consider the effects of slip length, Λ, on the results. We consider the effect of Λ only for w_p = 75 nm and λ_p = 150 nm, while permitting A_p to vary; this parameter set is sufficient to demonstrate the main effects of slip on the

dynamics of breakup. Figure 4.7 shows three important consequences of slip on both the dynamic and static states. First, for small A_p, smaller Λ promotes breakup of the central strip; this is due to the fact that, in order for the central strip to break up, the protrusion must not collapse too quickly, so that a smaller slip delays the collapse of the protrusion and allows breakup. Thus, the critical amplitude above which breakup occurs, A_c, increases with Λ. Second, for large A_p, small Λ prevents recoalescence of the side drops with the liquid near $z = 0$, so that an array with side drops is possible for smaller A_p, as indicated by the square symbols. Lastly, large Λ facilitates recoalescence of drops; for the free slip case, note that even when rupture of the central strip occurs, the drops inevitably recoalesce when $A_p > 175$ nm.

4.4 Discussion

4.4.1 Relation to Rayleigh–Plateau Instability Mechanism

One important finding so far is that the chosen rectangular-wave geometry leads to the formation of drops characterized by a spacing that is appreciably smaller than the critical wavelength expected from the prediction of the Rayleigh–Plateau instability analysis. This holds true even if only the cross sectional area of the central strip, Ω_0, is considered: of course, if the total area (including protrusions), Ω_{eff}, is used, the result leads to even higher efficiency when compared to the Rayleigh–Plateau prediction. To be specific, the central strip considered so far has a critical Rayleigh–Plateau wavelength of $\lambda_c(\Omega_0) \approx 160$ nm, and our simulation results find particle formation for $\lambda_p = 130$ and 150 nm. In particular, for $\lambda_p = 150$ nm, parameters leading to the formation of a one-dimensional array of drops (indicated by a circle in Figure 4.6) show $\lambda_c(\Omega_{eff})$ to be 1.5-2 times larger than λ_p.

4.4.2 Role of the Effective Area

Recall Figure 4.6, where we plot dashed curves showing constant Ω_{eff}. Consider first $\lambda_p = 150$ nm, plotted in Figure 4.6 (a). For relatively small Ω_{eff}, (indicated by lines in the lower left corner), it is impossible to destabilize a strip, as either the protrusions must be so thin (small w_p) that they break off without destabilizing effect, or A_p is below the critical value. In the other extreme, for large Ω_{eff} (top right corner), either A_p must be so large that side drops form, or w_p must be so large that no breakup occurs. Thus, only strips with an intermediate range of Ω_{eff} result in one-dimensional arrays of drops. We also note that differing parameters lead to a variety of results for the same Ω_{eff}. Consider the line of constant Ω_{eff} passing near $w_p = 45$ nm and $A_p = 300$ nm (plotted as a dash-dotted line in Figure 4.6 (a)). Large amplitude perturbations permit the formation of a two-dimensional array, as indicated by a square. Moving rightwards along the line, decreasing A_p results in a one-dimensional array (see, e.g., $w_p = 75$ nm and $A_p = 175$ nm), while further reduction in A_p leads to an end state which is a filament (see, e.g., $w_p = 125$ nm and $A_p = 100$ nm).

Figure 4.6 (b) shows the corresponding results for $\lambda_p = 130$ nm. Similarly to Figure 4.6 (a), perturbations of strips with small Ω_{eff} (lower left corner) do not lead to the formation of an array, while perturbations of strips with large Ω_{eff} (upper right corner) result in either a filament or an array of drops with side filaments. Only strips with an intermediate range of Ω_{eff} result in one and two-dimensional arrays. Just as in the $\lambda_p = 150$ nm case, the end state for the same Ω_{eff} depends on the choice of A_p and w_p. To show this, consider the line passing near $w_p = 65$ nm and $A_p = 175$ nm (plotted as a dash-dotted line); we see that only a small range of parameters permits the formation of an array of drops. For larger w_p, breakup of the central strip still occurs, but these drops subsequently recoalesce. Thus, for both $\lambda_p = 130$ nm and 150 nm, Ω_{eff} does not determine the end state, as varying w_p and A_p can completely

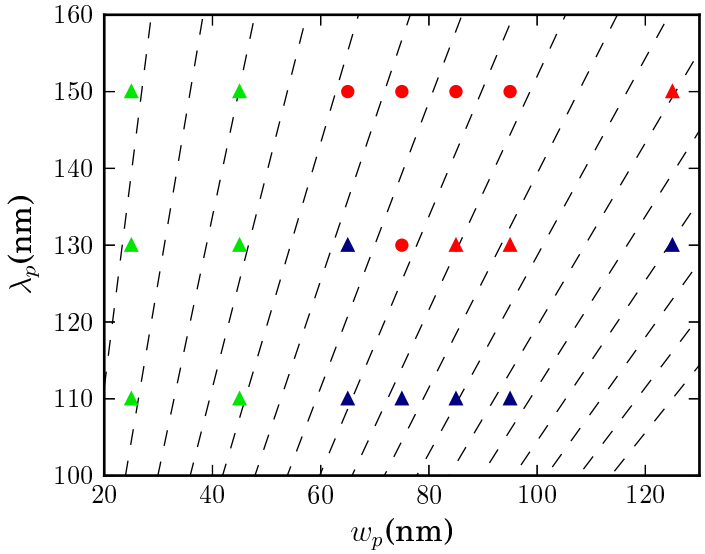

Figure 4.8 Parametric dependence on λ_p and w_p for $A_p = 150$ nm. Symbols and colors indicate the same end states and dynamics as in Figure 4.6. Dashed lines show curves of constant effective cross sectional area, Ω_{eff}. The area increases from bottom right to top left.

change both the type of breakup that occurs, as well as whether or not recoalescence occurs after any breakup.

Next, we discuss the effect of λ_p on the breakup. Figure 4.8 shows (λ_p, w_p) phase diagram for a fixed $A_p = 150$ nm, with curves of constant effective areas, Ω_{eff}. This plot shows that larger λ_p perturbations tend to promote breakup. This holds when moving along lines of constant Ω_{eff} from $w_p = 75$ nm and $\lambda_p = 150$ nm, which results in a one-dimensional array of drops, to $w_p = 65$ nm and $\lambda_p = 130$ nm, where no breakup occurs at all. Similarly, perturbed strips with Ω_{eff} that break up for $\lambda_p = 130$ nm (red symbols) do not break up for $\lambda_p = 120$ nm (blue symbols). As noted above, small Ω_{eff} results in strips that do not break up, so that no breakup occurs for $\lambda_p = 130$ nm, and $w_p \leq 65$ nm. It is worth noting here that λ_p has little effect on the behavior of the protrusions when w_p is fixed. For $w_p \leq 45$ nm, Figure 4.8 shows that for all λ_p, the protrusions break off, as indicated by the green color. On

the other hand, for $w_p \geq 65$ nm, the protrusions do not break off, as indicated by the red and blue colors.

4.4.3 Summary of the Breakup

We are now in the position to summarize the mechanism by which the rectangular-wave geometry breaks up. The primary driving mechanism of the breakup is based on the fact that the cross-shaped geometry near $x = n\lambda_p$ leads to an initial negative x-z curvature, which, as the structure begins its initial retraction, results in the formation of a low pressure bulge. Along the central strip, near $x = (n + 1/2)\lambda_p$, the liquid retracts to a half-cylinder. A positive x-y curvature of magnitude $1/\sqrt{2hw/\pi}$ leads to a large corresponding Laplace pressure at $x = (n + 1/2)\lambda_p$ between two low pressure bulges at $x = n\lambda_p$, and so liquid drains out of the neck into the bulges, leading to breakup.

Figures 4.6 (a) and 4.6 (b) show that neither the end state nor the dynamics are entirely determined by the effective area Ω_{eff}. For strips with a small Ω_{eff}, either the perturbation has a small A_p and it cannot break the strip up, or w_p is so small that the protrusions form side drops, and the strip still does not break up. Strips with large Ω_{eff} may break up, and then either a two-dimensional array forms, or the drops will recoalesce into a filament. Only for strips with an intermediate range of Ω_{eff} is a one-dimensional array of drops a possible end state.

Since the dynamics of the retraction may vary with the same Ω_{eff}, and changing the amount of liquid per wavelength necessarily changes the possible end states, it is necessary to consider any breakup in terms of the dynamics (classification shown by color in Figure 4.6 (a) and Figure 4.6 (b)). The amplitude A_p is only important in that it must be larger than a critical one, A_c, in order for the central strip to break up. For larger values of A_p and a fixed w_p, the central strip does not change its dynamics;

that is, once breakup is possible, any further increase in A_p does not affect whether or not the central strip breaks up at some point in time.

Whenever drops form, it is found that the resulting center to center spacing is always equal to λ_p, and as discussed in Section 4.4.1, λ_p is generally smaller than the smallest possible spacing that can be understood using the Rayleigh–Plateau instability analysis. Thus, a rectangular-wave edge perturbation is a highly effective way of generating arrays of closely spaced drops, far below what would be possible when using the Rayleigh–Plateau driven breakup. However, if λ_p and Ω_{eff} are specified, determined by a desired drop size and spacing for a one-dimensional array, then at least one of w_p and A_p is a free parameter, which can completely change the end state resulting from the breakup.

4.4.4 Formation of Satellite Drops

The end state for a variety of parameters for $\lambda_p = 150$ nm includes small satellite drops between the drops in the central array; no satellite drops are present in the end state when $\lambda_p = 130$ nm. Figure 4.9 (a) shows the snapshots of the drop, for $A_p = 150$ nm, $\lambda_p = 150$ nm, and $w_p = 75$ nm, just prior to breakup (left), and at the end state (right). Prior to the breakup, a very thin filament connects the two drops; after the breakup, there are small satellite drops located at $x = (n + 1/2)\lambda_p$. The formation of these satellite drops is due to the fact that the thin filament breaks up near its ends. Figure 4.9 (b) shows a close up of the connecting filament just prior to (left) and after (right) the breakup. Just prior to the breakup, the connecting filament begins to neck at a point close to the primary drop, which results in the filament breaking up near its ends. After breakup, this filament retracts into a small satellite drop. The size of the satellite drop is therefore determined by the amount of liquid in the connecting filament. Figure 4.9 (c) shows the radius of the satellite drops for all parameters when the central strip breaks up and a satellite drop results,

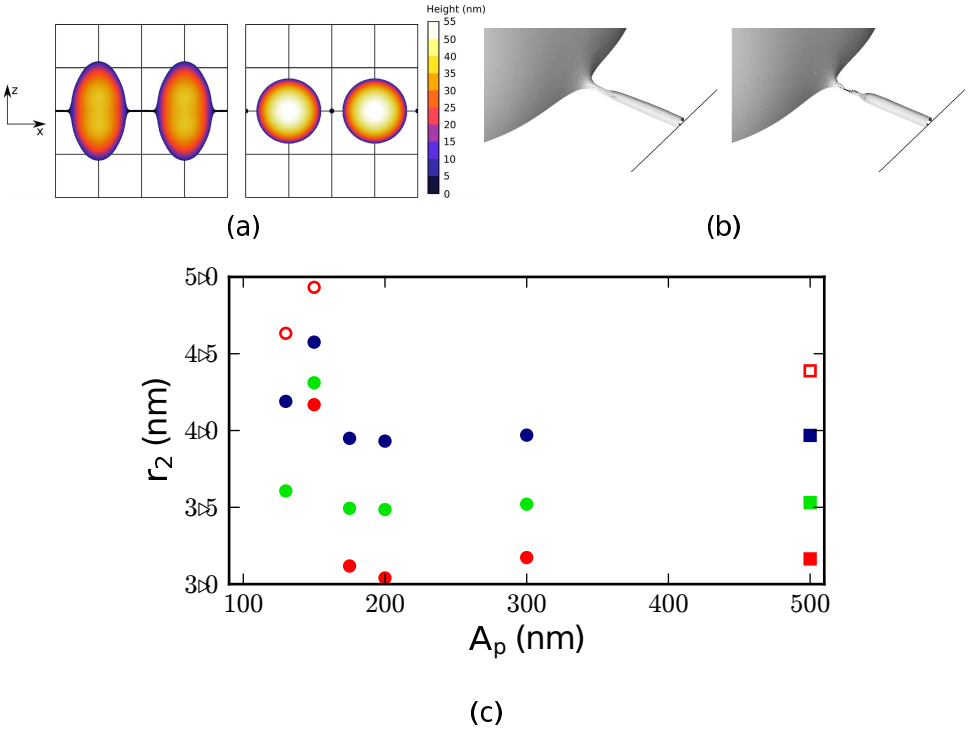

Figure 4.9 (a) Satellite drops for $w_p = 75$ nm and $A_p = 150$ nm. One box is 75 nm by 75 nm. (b) Close up of the breakup of the filament connecting primary drops for $w_p = 75$ nm and $A_p = 150$ nm. Note that a mirror condition is applied at the solid black line, so that this represents half of the filament. (c) Satellite drop radius for $w_p = 65$ nm (red), $w_p = 75$ nm (green), $w_p = 85$ nm (blue), and $w_p = 95$ nm (hollow red). Circles indicate that the equilibrium is a one-dimensional array, and squares that the end state is an array with side drops. For these results, $\lambda_p = 150$ nm.

for $\lambda_p = 150$ nm. In general, larger w_p leads to larger satellite drops. Regarding the influence of A_p, we find that the size of the satellite drop peaks for $A_p = 150$ nm, and is approximately the same for larger values of A_p. We generally find that A_p and w_p influence the formation of different length filaments and consequently the formation of satellite drops of different sizes. We note, however, that the size of satellite drops depend on the nature of the evolution in a complicated manner, whether protrusions break up or not, and/or when they break up. We leave the investigation of this issue for future work.

4.5 Conclusions

In this chapter, we show that the initial geometry of a fluid deposited on a substrate has a strong influence on the morphology of the final patterns that result due to the fluid instability. In particular, we find that appropriate choices of the initial geometry may lead to instabilities even in configurations that are expected to be stable based on the analogy with the Rayleigh–Plateau instability mechanism. Our computational results show that the initial liquid shape strongly influences the distribution of the pressure in the liquid. Therefore, rectangular waveform perturbations, considered in this chapter, lead to evolution that is considerably different from, for example, the one resulting if sinusoidal waveform perturbations are applied.

While the methods that we use are of general validity, we concentrate particularly on recent experiments carried out with liquid metals on nano-scale, where the ability to control the location and size distribution of the resulting nanoparticles is of fundamental interest in applications in the field of nano-assembly. We show that a diverse range of nanoparticle arrays can be observed and that the rectangular-wave geometries perturbed by short wavelengths (shorter than the critical wavelength predicted by the Rayleigh–Plateau instability) exhibit a complex nonlinear evolution. We classify the dynamic behavior as well as the end states for the perturbations that

differ by their aspect ratio and the perturbation wavelengths, λ_p. We demonstrate that it is possible to produce arrays of drops with the spacing, λ_p, as small as half the critical wavelength predicted by the Rayleigh–Plateau instability mechanism. Added complexity is introduced by the fact that the aspect ratio of the introduced perturbations plays an important role: for example, given an 'effective' area, Ω_{eff} (total volume of the liquid per λ_p), a significantly different evolution can be observed for different aspect ratios. Depending on the parameters, one-dimensional arrays of drops for an intermediate range of Ω_{eff} can then be obtained; larger Ω_{eff} tends to produce central arrays of drops with drop arrays on the sides (two-dimensional arrays), while smaller Ω_{eff} structures do not break up. Additional configurations are possible as well, see Figure 4.5 for a complete classification.

One particular feature of the instabilities that are observed in this study is the complex coupling between the dynamics and end configurations, with differing dynamics leading to possibly the same end states, as illustrated in Figure 4.5. Our study demonstrates some, perhaps not obvious, features of the instability development. For example, we find that the perturbation amplitude, A_p, in general has to be larger than a critical value, A_c, for breakup to occur, and for some cases, increasing A_p results in the final state transitioning from a filament, to a one-dimensional array, back to a filament, and into a two-dimensional array of drops. Decreasing λ_p tends to prevent the formation of drops, and for a very small λ_p, the central strip does not rupture at all. The slip length, Λ, is found to have a significant effect on the formation of arrays and the stability of the structures, with a smaller Λ associated with breakup and the formation of arrays, and a larger Λ either preventing the breakup altogether, or leading to recoalescence of the resulting drops after the breakup occurs. Therefore, by varying the geometry and slip, it is possible to obtain, in a controllable manner, a large range of different dynamics, and a variety of end states.

In this chapter we consider a relatively simple liquid geometry, although the evolution dynamics turns out to be far from simple. We leave the consideration of the variation of the contact angle, Reynolds number, and capillary number, to future work. Ongoing work in material science makes these future studies highly relevant.

CHAPTER 5

A VOLUME OF FLUID METHOD FOR SIMULATING FLUID/FLUID INTERFACES IN CONTACT WITH SOLID BOUNDARIES

5.1 Introduction

In the previous chapters, we have discussed the application of Gerris to specific problems involving contact lines and film instabilities. However, as we previously pointed out, a critical component of contact line physics has not previously been taken into account by Volume of Fluid based solvers: the interaction between liquids and solids, consisting of attraction at long ranges and repulsion at short ranges. In this chapter, we present a computational framework for the inclusion of a general fluid/solid interaction in the context of contact line simulation. This approach allows for computing fluid wetting properties (such as equilibrium contact angle) based on first principles, and without restriction to small contact angles.

The motivation for this work are the long–wave models that we have discussed in detail in Chapter 3. By taking into account the liquid/solid interaction in the form of disjoining pressure, in these models the contact angle is an emergent property of the simulation of the underlying physics, and consequently also the film instability that was discussed in Chapter 1. The disjoining pressure formulation which is used includes the van der Waals or electrostatic interactions into the model in the form of a local pressure contribution acting on the fluid/solid interface; however in addition to the simplifying assumptions already embedded in the long–wave model, this fluid/solid interaction term is derived under the assumption of a flat film [14, 15, 20, 48]. Therefore these approaches cannot be trivially extended to the configurations involving large contact angles.

Here, we present a novel approach, based on a Volume of Fluid formulation, which includes the fluid/solid interaction forces into the governing Navier-Stokes equations, without limitations inherent in the long–wave model. This inclusion allows for arbitrary contact angles to be incorporated based on modeling the underlying physics, in contrast to conventional Volume of Fluid methods. The presented approach also leads to the regularization of the viscous stress since the fluid film thickness never becomes zero. Furthermore, our framework can account for additional physical effects, such as instability and breakup of thin fluid films, that would not be described if fluid/solid interaction forces were not explicitly included. We note here that while film rupture can also occur in phase-field based approaches (as in [49]), this seems to be due to the presence of a rather thick interface, and not due to the explicit inclusion of destabilizing fluid/solid interaction forces.

In the present chapter we focus on formulating and discretizing the model, and on discussing issues related to convergence and accuracy. To validate our proposed numerical scheme, we consider two representative examples, involving relaxation and spreading of sessile drops with various contact angles on a substrate. These benchmark cases permit comparison of our results with well established analytical solutions for a particular flow regime. The application of the method to the study of thin film stability including dewetting will be considered in the sequel [56].

The rest of this chapter is organized as follows. We describe the details of the fluid/solid interaction in Section 5.2. In Section 5.3, we describe two finite-volume methods for the discretization of the considered fluid/solid interaction forces. The presentation in these two sections applies to any generic fluids. In Section 5.4 we present a comparison of the two considered discretization methods for equilibrium and spreading drops, for a particular choice of material parameters. In Section 5.5, we give an overview and future outlook.

5.2 Model

Consider a perfectly flat solid substrate covered by two immiscible fluids. There are three relevant interfacial energies: the liquid/solid, γ_{ls}, the vapor/solid, γ_{vs}, and the liquid/vapor, γ, energies. The contact angle is commonly defined as the angle between the tangent plane of the interface between the liquid and vapor phases and the solid substrate at the point where the interface meets the surface. At equilibrium, the contact angle, θ_{eq}, and the surface energies are related by Young's Equation [95]:

$$\gamma_{vs} = \gamma_{ls} + \gamma \cos\theta_{eq} \tag{5.1}$$

If there is a nonzero contact angle at equilibrium, the liquid partially wets the solid surface; if the equilibrium configuration is a flat layer covering the whole substrate, then it fully wets the solid surface. It is also possible for the liquid to be non-wetting, where the liquid beads up into a sphere on the surface. The wetting behavior of the system can be characterized by the equilibrium spreading coefficient, defined by:

$$S_{eq} = \gamma_{vs} - (\gamma_{ls} + \gamma) \tag{5.2}$$

which expresses the difference in energy per unit area between a surface with no liquid, and one with a layer of liquid (what we call 'dry' and 'wet' states, respectively). Wetting is determined by the sign of S_{eq}; partial wetting occurs for $S_{eq} < 0$, and complete wetting for $S_{eq} = 0$ [10].

The above characterization of the contact angle is straightforward for static configurations and at macroscopic length scales. If these assumptions are not satisfied, definitions of contact angles become more complex. In the literature, a distinction is made between the apparent contact angle, θ_{ap}, and the microscopic contact angle, θ_m, distinguished by the distance from the contact line at which the measurement is made [28]. The contact angle resulting from measuring on macroscopic length scales is θ_{ap}, while θ_m is measured at short length scales which are still long enough so that

the continuum limit is appropriate [10, 76, 92]. The microscopic contact angle, θ_m, is often identified with θ_{eq}, which is commonly used in the derivation of spreading laws, such as the classical Cox-Voinov law [92]. It should be noted that the details of the fluid behavior on nano scales in the vicinity of the fluid fronts and associated contact lines are far from being completely understood [10], and the way in which the contact angle arises at small scales is a subject of ongoing research [78].

The surface energies entering Eq. (5.1) and Eq. (5.2) arise due to the van der Waals interaction between the different phases that are relevant on short length scales. Three kinds of van der Waals interactions are usually considered: interactions between polar molecules, interaction of molecules that have an induced polarization, and the dispersion forces [48]. The dispersion interaction is relevant for all molecules, and will be the only one that we consider. A common model for approximating the dispersion interaction of two particles, of phases i and j, centered at $\mathbf{x}_0$ and $\mathbf{x}_1$ is the 12-6 Lennard Jones potential [48]:

$$\phi_{\mathrm{LJ}}(r) = 4\epsilon_{ij}\left(\left(\frac{\sigma}{r}\right)^{12} - \left(\frac{\sigma}{r}\right)^{6}\right) \tag{5.3}$$

This potential has a minimum, ϵ_{ij}, at $r = 2^{1/6}\sigma$, and for simplicity we assume that σ is a constant for any two interacting particles. The center distance between the two particles is given by:

$$r = \sqrt{(x_0 - x_1)^2 + (y_0 - y_1)^2 + (z_0 - z_1)^2}$$

The powers 12 and 6 in Eq. (5.3) correspond to short range repulsion and long range attraction, respectively. For our purposes, we generalize this formulation and use the following form:

$$\phi_{ij}(r) = K^*_{ij}\left(\left(\frac{\sigma}{r}\right)^{p} - \left(\frac{\sigma}{r}\right)^{q}\right) \tag{5.4}$$

Here K_{ij}^* is the scale of the potential well, having units of energy per particle pair interaction. In general, we require only that $p > q$ are integers, such that $q > 3$, for reasons that will become clear shortly.

Our model considers two fluid phases, a liquid phase and a vapor phase occupying the region $y > 0$, interacting with a flat, half infinite, solid substrate (subscript s) in the region $y < 0$. Consider now a particle located at $\mathbf{x}_0 = (x_0, y_0, z_0)$ of phase i (where i is either l or v). The interaction energy between this particle and the substrate per unit volume of the substrate is:

$$\psi_{is}(r) = n_s \phi_{is}(r) \tag{5.5}$$

where n_s is the particle density in the substrate.

We derive the force per unit volume following a similar procedure outlined in [52]. Integrating Eq. (5.5) over the region $y < 0$ yields the following total interaction of a particle in phase i with the substrate:

$$\int_{-\infty}^{0}\int_{\infty}^{\infty}\int_{-\infty}^{\infty} \psi_{is}(r)dxdzdy = 2\pi n_s K_{is}^* \sigma^3 \left[\frac{1}{(2-p)(3-p)} \left(\frac{\sigma}{y_0}\right)^{p-3} - \frac{1}{(2-q)(3-q)} \left(\frac{\sigma}{y_0}\right)^{q-3} \right]$$

Although the van der Waals interaction is not strictly additive, the effects due to non-additivity are usually weak [48], and we ignore them for simplicity.

Multiplying by n_i, the particle density in phase i, we obtain the van der Waals interaction per unit volume of phase i:

$$\Phi_{is}(y_0) = 2\pi n_i n_s K_{is}^* \sigma^3 \left[\frac{1}{(2-p)(3-p)} \left(\frac{\sigma}{y_0}\right)^{p-3} - \frac{1}{(2-q)(3-q)} \left(\frac{\sigma}{y_0}\right)^{q-3} \right] \tag{5.6}$$

We introduce the following parameters:

$$\mathcal{K}_{is} = 2\pi n_i n_s K_{is}^* \sigma^3 \left(\frac{[(p-2)(p-3)]^{q-3}}{[(q-2)(q-3)]^{p-3}} \right)^{\frac{1}{p-q}} \tag{5.7}$$

$$h^* = \left[\frac{(q-2)(q-3)}{(p-2)(p-3)} \right]^{\frac{1}{p-q}} \sigma \tag{5.8}$$

$$m = p - 3 \qquad n = q - 3$$

This simplifies Eq. (5.6) to:

$$\Phi_{is}(y) = \mathcal{K}_{is} \left[\left(\frac{h^*}{y} \right)^m - \left(\frac{h^*}{y} \right)^n \right] \tag{5.9}$$

The quantity h^* is referred to as the 'equilibrium film thickness' and will be considered in more detail below. Note that Eq. (5.9) has an identical form as Eq. (5.4).

The force per unit volume on phase i that results from the potential is computed by taking the gradient of Eq. (5.9):

$$\mathbf{F}_{is}(y) = -\nabla \Phi_{is}(y) = \frac{\mathcal{K}_{is}}{h^*} \left[m \left(\frac{h^*}{y} \right)^{m+1} - n \left(\frac{h^*}{y} \right)^{n+1} \right] \hat{y} \tag{5.10}$$

Here $\hat{y}$ refers to the unit vector $(0, 1, 0)$.

We proceed to derive an expression for θ_{eq} in terms of $\mathcal{K}_{ls}$ and $\mathcal{K}_{vs}$ in Eq. (5.9) according to the microscopic arguments outlined in [14]. Combining Eqs. (5.1) and (5.2), we obtain the following expression for the equilibrium spreading coefficient:

$$S_{eq} = \gamma(\cos\theta_{eq} - 1) \tag{5.11}$$

where S_{eq} is the difference in the energy per unit area between a dry system and a wet system. The total energy required to remove a liquid layer originally occupying $\delta_0 < y < \infty$ and replace it with a layer of the vapor phase is given by:

$$\Delta E = \int_{\delta_0}^{\infty} (\phi_{vs} - \phi_{ls}) dy \tag{5.12}$$

If δ_0 is the smallest distance between particles of the substrate and fluids when they are in contact, Eq. (5.12) specifies the total energy required to completely remove the liquid from the substrate. Even if δ_0 takes a larger value, Eq. (5.12) consistently describes the energy difference between a wet system, and a dry system which consists of a fluid layer of thickness δ_0 wetting the solid substrate.

Performing the integration in Eq. (5.12), we obtain:

$$S_{eq} = (\mathcal{K}_{vs} - \mathcal{K}_{ls})h^* \left[\frac{1}{m-1} \left(\frac{h^*}{\delta_0} \right)^{m-1} - \frac{1}{n-1} \left(\frac{h^*}{\delta_0} \right)^{n-1} \right] \tag{5.13}$$

In order to be in a partial wetting regime, i.e. where there is a non-zero contact angle, we require $S_{eq} < 0$. Based on Eq. (5.13), we find:

1. $\delta_0 > \left(\frac{n-1}{m-1}\right)^{\frac{1}{m-n}} h^*$: In this case, the attractive term in Eq. (5.13) dominates. This leads to a negative spreading coefficient only if $\mathcal{K}_{vs} > \mathcal{K}_{ls}$, so that the vapor phase must experience a greater attraction than the liquid phase in order to be in a partial wetting regime.

2. $\delta_0 < \left(\frac{n-1}{m-1}\right)^{\frac{1}{m-n}} h^*$: In this case, the repulsive term in Eq. (5.13) dominates, and partial wetting is possible when $\mathcal{K}_{vs} < \mathcal{K}_{ls}$.

The first case states that when δ_0 is large, the vapor phase must interact more strongly with the substrate than the liquid phase; the reverse is true when δ_0 is small. For example, the second case must hold for partial wetting of a drop surrounded by a vacuum.

For comparison, the method of imposing the contact angle in long–wave described in Chapter 3 is very similar. In particular, it states that the pressure jump across the flat interface of a film of thickness h is given by

$$p_v - p_l = \Pi(h) \tag{5.14}$$

where $\Pi(h)$ is defined in Eq. (3.5), and p_v and p_l refer to the pressure in the vapor and the liquid respectively. The definition of the parameter h^* in $\Pi(h)$ is identical to that of Eq. (5.13).

Following the example of disjoining pressure, we consider situations such that there is a layer of thickness h^* completely covering the surface even when the fluid is partially wetting. In particular, this means that we assume that $\delta_0 = h^*$, so that in Eq. (5.12), the liquid is removed only to a thickness h^*. This value of δ_0 has the convenient property that it allows for Eq. (5.13) to be simplified, while the presence of a wetting layer over the whole substrate removes the contact line singularity. Plugging $\delta_0 = h^*$ into Eq. (5.13), and substituting in the expression for S_{eq} from Eq. (5.11), we obtain the following expression for the difference between $\mathcal{K}_{vs}$ and $\mathcal{K}_{ls}$ as a function of θ_{eq}:

$$\mathcal{K}_{vs} - \mathcal{K}_{ls} = \frac{\gamma(1-\cos\theta_{eq})}{h^*}\left(\frac{(m-1)(n-1)}{m-n}\right) \tag{5.15}$$

Therefore, only the difference $\mathcal{K}_{vs} - \mathcal{K}_{ls}$ is needed to specify θ_{eq}. Similar formulations appear in the long–wave literature [24, 74]. Note that since Eq. (5.12) assumes that the fluid occupies a half infinite domain in the wet state, Eq. (5.15) is satisfied exactly only in the limit where h^* is vanishingly small relative to the drop thickness.

To summarize, in this section we have formulated a method that allows for the inclusion of fluid/solid interaction forces without the limitations inherent in long–wave theory, such as negligible inertia and small interfacial slope. Next we proceed to discuss numerical implementation.

5.3 Numerical Methods

Equations (5.9) and (5.10) present a difficulty in that they diverge as $y \to 0$. This can be dealt with by introducing a cutoff length, i.e. forcing $\mathbf{F}_{is} = 0$ when y is less than the cutoff. This method has the drawback of making the force discontinuous,

and may lead to poor numerical convergence. For this reason, we introduce a shifted potential:

$$\hat{\Phi}_{is} = \mathcal{K}_{is}\left[\left(\frac{h^*}{y+h_c}\right)^m - \left(\frac{h^*}{y+h_c}\right)^n\right] \tag{5.16}$$

where h_c is some parameter less than h^*. Equation (5.16) removes the singular portion of the potential near $y \to 0$ for a small h_c, and is equal to zero at $y = h^* - h_c$, but otherwise keeps the same functional form. We refer to films occupying $0 \leq y \leq h^* - h_c$ as equilibrium films, and $h^* - h_c$ as the equilibrium film thickness. The force corresponding to Eq. (5.16) is given by

$$\hat{\mathbf{F}}_{is} = \frac{\mathcal{K}_{is}}{h^*}\left[m\left(\frac{h^*}{y+h_c}\right)^{m+1} - n\left(\frac{h^*}{y+h_c}\right)^{n+1}\right]\hat{y} \tag{5.17}$$

Recall the characteristic function χ defined in Chapter 2, which takes the value 1 inside the liquid phase and 0 elsewhere. We can write the total body force more compactly as follows:

$$\hat{\mathbf{F}}_B(y) = \chi\hat{\mathbf{F}}_{ls} + (1-\chi)\hat{\mathbf{F}}_{vs} \tag{5.18}$$

where the interaction strength explicitly depends on the phase through χ, so that $\mathcal{K}(1) = \mathcal{K}_{ls}$ and $\mathcal{K}(0) = \mathcal{K}_{vs}$.

The governing equations for this chapter are Eq. (2.1), subject to an additional force from Eq. (5.17):

$$\rho(\chi)(\partial_t\mathbf{u} + \mathbf{u}\cdot\nabla\mathbf{u}) = -\nabla p + \nabla\cdot\left[\mu(\chi)(\nabla\mathbf{u} + \nabla\mathbf{u}^T)\right] + \gamma\kappa\delta_s\mathbf{n} + \hat{\mathbf{F}}_B(y) \tag{5.19}$$

$$\nabla\cdot\mathbf{u} = 0 \tag{5.20}$$

Letting L be the length scale, and $\mathcal{T}$ the time scale, we define the following dimensionless variables:

$$\begin{aligned} \tilde{x} &= \frac{x}{L} & \tilde{y} &= \frac{y + h_c}{L} \\ \tilde{z} &= \frac{z}{L} & \tilde{t} &= \frac{t}{\mathcal{T}} \\ \tilde{h}^* &= \frac{h^*}{L} & \tilde{h}_c &= \frac{h_c}{L} \\ \tilde{\mathbf{u}} &= \frac{\mathbf{u}\mathcal{T}}{L} & \tilde{p} &= \frac{L}{\gamma} p \\ \tilde{\kappa} &= L\kappa & \tilde{\delta_s} &= L\delta_s \end{aligned}$$

With these scales, and dropping the tildes, the dimensionless Navier-Stokes equations are as follows:

$$We(\chi)(\partial_t \mathbf{u} + \mathbf{u} \cdot \nabla \mathbf{u}) = -\nabla p + \nabla \cdot \left[Ca(\chi)(\nabla \mathbf{u} + \nabla \mathbf{u}^T)\right] + \kappa \delta_s \mathbf{n} + \mathbf{F}_B(y) \quad (5.21)$$

$$\nabla \cdot \mathbf{u} = 0 \quad (5.22)$$

where

$$\mathbf{F}_B(y) = K(\chi)\mathcal{F}(y)\hat{y} = K(\chi)\left[m\left(\frac{h^*}{y}\right)^{m+1} - n\left(\frac{h^*}{y}\right)^{n+1}\right]\hat{y} \quad (5.23)$$

Here, the dimensionless y-coordinate is translated, so that $\mathcal{F}(h^*) = 0$, and the equilibrium film occupies $h_c \leq y \leq h^*$. The (phase-dependent) dimensionless numbers are the Weber number, We, the capillary number, Ca, and the force scale for the van

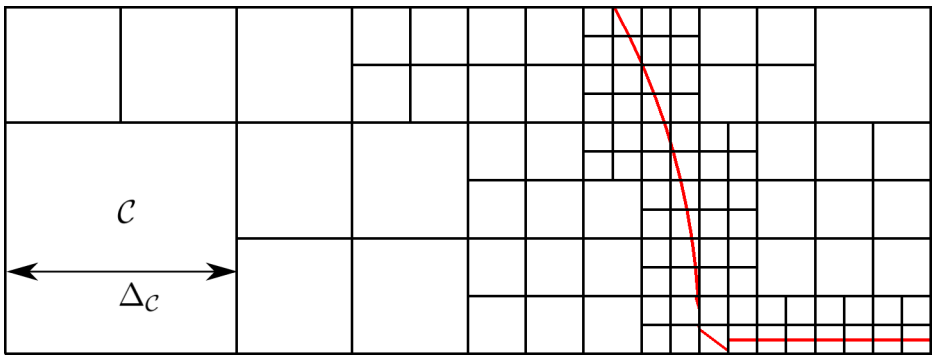

Figure 5.1 Illustration of the quad-tree used to discretize the computational domain. The mesh resolution can be chosen adaptively, so that each cell $\mathcal{C}$ has a corresponding size $\Delta_{\mathcal{C}}$. The red curve shows the piecewise linear reconstruction of the liquid/vapor interface obtained using the Volume of Fluid method.

der Waals interaction, K, given by the following:

$$We(\chi) = \frac{\rho(\chi)L^3}{\mathcal{T}^2\gamma} = \chi We_l + (1-\chi)We_v = \frac{L^3}{\mathcal{T}^2\gamma}\left(\chi\rho_l + (1-\chi)\rho_v\right) \quad (5.24)$$

$$Ca(\chi) = \frac{\mu(\chi)L}{\gamma\mathcal{T}} = \chi Ca_l + (1-\chi)Ca_v = \frac{L}{\gamma\mathcal{T}}\left(\chi\mu_l + (1-\chi)\mu_v\right) \quad (5.25)$$

$$K(\chi) = \frac{\mathcal{K}(\chi)L}{h^*\gamma} = \chi K_{ls} + (1-\chi)K_{vs} = \frac{L}{h^*\gamma}\left(\chi\mathcal{K}_{ls} + (1-\chi)\mathcal{K}_{vs}\right) \quad (5.26)$$

Upon nondimensionalization, Eq. (5.15) yields the following expression for θ_{eq}:

$$\Delta K(\theta_{eq}) := K_{vs} - K_{ls} = \frac{(1-\cos\theta_{eq})}{h^{*2}}\left(\frac{(m-1)(n-1)}{(m-n)}\right) \quad (5.27)$$

Again, the system Eqs. (5.21)-(5.22) is solved using Gerris. A typical adaptive mesh used by Gerris is illustrated in Figure. 5.1; note that we consider the implementation in two spatial dimensions from now onward. In order to develop our method, some more detail about the finite-volume approach is required. The finite-volume method treats each cell $\mathcal{C}$ as a control volume, so that the variables associated with $\mathcal{C}$ represent the volume averaged value of the variable over $\mathcal{C}$. Each cell has a size $\Delta_{\mathcal{C}}$, and center coordinates (x_c, y_c). The Volume of Fluid method tracks the interface implicitly by defining a volume fraction function, $T(\mathcal{C})$, which gives the fraction of the volume of $\mathcal{C}$ occupied by the liquid phase. $T(\mathcal{C})$ is advected by the

fluid flow according to the following equation:

$$\partial_t T + \nabla \cdot (\mathbf{u}T) = 0 \tag{5.28}$$

The value of We and Ca in a cell $\mathcal{C}$ are then represented using an average:

$$We(\mathcal{C}) = We_l T(\mathcal{C}) + We_v(1 - T(\mathcal{C}))$$

$$Ca(\mathcal{C}) = Ca_l T(\mathcal{C}) + Ca_v(1 - T(\mathcal{C}))$$

Here, as before, subscript l corresponds to liquid, and v to the vapor phase.

The exact average of the force over the computational cell, $\mathcal{C}$, is given by:

$$\begin{aligned}\mathbf{F}_B(\mathcal{C}) &= \frac{1}{\Delta_C^2}\int\int_{\mathcal{C}} K(\chi(x,y))\mathcal{F}(y)d\mathcal{C}\,\hat{y} \\ &= \frac{1}{\Delta_C^2}\int\int_{\mathcal{C}} \left[K_{ls}\chi(x,y) + K_{vs}(1-\chi(x,y))\right]\mathcal{F}(y)d\mathcal{C}\,\hat{y}\end{aligned} \tag{5.29}$$

where $\mathcal{F}(y)$ is defined by Eq. (5.23). We detail two possibilities for the discretization of the van der Waals force term in Eq. (5.21). For both of these methods, the force is included explicitly in the predictor step of the projection method.

Method I:

Our first method proceeds by a simple second order discretization of Eq. (5.29):

$$\begin{aligned}\mathbf{F}_I(\mathcal{C}) &= \frac{\mathcal{F}(y_c)}{\Delta_C^2}\int\int_{\mathcal{C}} \left[K_{ls}\chi(x,y) + K_{vs}(1-\chi(x,y))\right] d\mathcal{C}\,\hat{y} \\ &= \left[\frac{\mathcal{F}(y_c)}{\Delta_C^2}K_{ls}\int\int_{\mathcal{C}}\chi(x,y)d\mathcal{C} + \frac{\mathcal{F}(y_c)}{\Delta_C^2}K_{vs}\int\int_{\mathcal{C}}(1-\chi(x,y))d\mathcal{C}\right]\hat{y}\end{aligned}$$

We identify the average of χ over $\mathcal{C}$ with $T(\mathcal{C})$, yielding the following expression:

$$\mathbf{F}_I(\mathcal{C}) = \left[T(\mathcal{C})K_{ls} + (1 - T(\mathcal{C}))K_{vs}\right]\mathcal{F}(y_c)\,\hat{y} \tag{5.30}$$

However, we note that the accuracy of this simple method can deteriorate at low mesh resolutions because $\mathcal{F}$ has a large gradient as $y \to 0$. Consider a cell such that

$T(\mathcal{C}) = 1$. To a first approximation, the error in Eq. (5.30) is given by:

$$\begin{aligned}\mathcal{E} = |\mathbf{F}_B(\mathcal{C}) - \mathbf{F}_I(\mathcal{C})| &= \left| K_{ls}\frac{\Delta_C^2}{24}\mathcal{F}''(y_c) + o(\Delta_C^2) \right| \\ &\approx \frac{\Delta_C^2}{24}\frac{K_{ls}}{h^{*2}}\Bigg| m(m+1)(m+2)\left(\frac{h^*}{y}\right)^{m+3} \\ &\qquad -n(n+1)(n+2)\left(\frac{h^*}{y}\right)^{n+3}\Bigg|\end{aligned}$$

To show that this can lead to large errors, consider the error when $\Delta_{\mathcal{C}} = h^* - h_c$, in a cell with center at $y_c = (h^* + h_c)/2$, i.e. for a cell along the bottom boundary when h^* is just barely resolved. The error in this cell is:

$$\begin{aligned}\mathcal{E}_1 = \frac{(1-h_c/h^*)^2}{24}K_{ls}\Bigg| & m(m+1)(m+2)\left(\frac{2}{1+h_c/h^*}\right)^{m+3} \\ & -n(n+1)(n+2)\left(\frac{2}{1+h_c/h^*}\right)^{n+3}\Bigg|\end{aligned}$$

The lower bound of this error can be shown to be:

$$\mathcal{E}_1 > \frac{(1-h_c/h^*)^2}{24}K_{ls}\left(m(m+1)(m+2) - n(n+1)(n+2)\right)$$

Since $m \geq n+1$, we can bound this further by:

$$\mathcal{E}_1 > \frac{(1-h_c/h^*)^2}{8}K_{ls}m(m+1) \tag{5.31}$$

Note that $\mathcal{E}_1$ is not the discretization error, but the error found for a fixed grid size.

Recalling that Eq. (5.27) implies that K_{ls} is proportional to $1/(h^*)^2$, so if h_c is significantly smaller than h^* the errors are quite large unless Δ_C is much smaller than h^*. Furthermore, h^* is generally small relative to the length scale of the drop considered in Eq. (5.13), so that the mesh size required to accurately resolve the right hand side of Eq. (5.29) will increase the computational cost.

Method II:

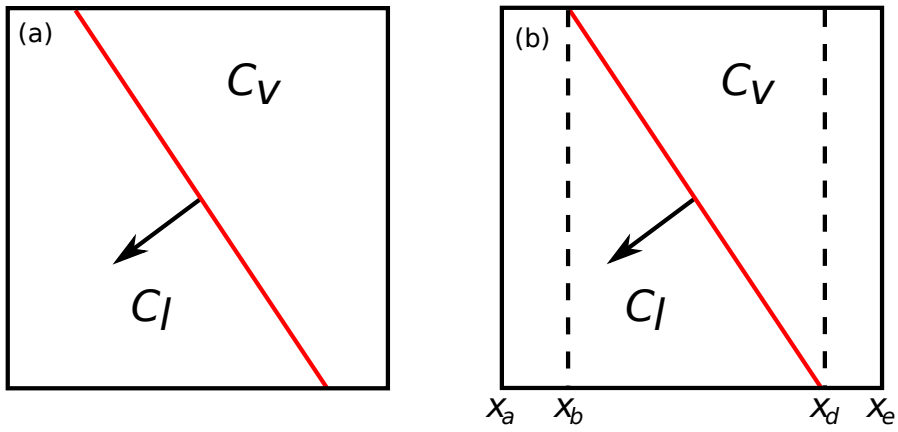

Figure 5.2 Illustration of a cell with $0 < T(\mathcal{C}) < 1$: (a) cut cell divided into regions C_l and C_v entirely occupied by the liquid and vapor phases, respectively, and (b) illustration of the regions of integration of a cut cell. The linear reconstruction of the interface from the Volume of Fluid method is shown by the red line.

Since Eq. (5.23) gives an exact formula for the force per unit volume in a single phase, much of the simplification used in deriving Eq. (5.30) is unnecessary. For the second method, we take advantage of this fact to more accurately approximate Eq. (5.29). First, note that it is trivial to integrate Eq. (5.29) when $T(\mathcal{C}) = 1$ or $T(\mathcal{C}) = 0$. Moreover, the Volume of Fluid method gives additional information beyond just the fraction of the cell occupied by the liquid phase; using the reconstructed interface, we have an approximation of the portion of the cell which is occupied by the liquid phase as well. Therefore, we introduce the following alternative method. Consider a cell $\mathcal{C}$ with center (x_c, y_c), where $0 < T(\mathcal{C}) < 1$, so that the Volume of Fluid method yields a linear reconstruction of the interface in the cell. This interface divides the cell into a region occupied by the liquid phase, C_l, and a region occupied by the vapor phase, C_v (see Figure 5.2). We can write a general algorithm to integrate over these regions, yielding the following expression for the average force on cell $\mathcal{C}$:

$$\mathbf{F}_{II}(\mathcal{C}) = \left[\frac{\mathcal{K}_{ls}}{\Delta_C^2}\int\int_{C_l}\mathcal{F}(y)dxdy + \frac{\mathcal{K}_{vs}}{\Delta_C^2}\int\int_{C_v}\mathcal{F}(y)dxdy\right]\hat{y} \tag{5.32}$$

We briefly outline the general process to perform the integrations over C_l and C_v. Let the Volume of Fluid reconstructed interface in the cell be given by $\mathbf{M}\cdot\mathbf{x} = \alpha$,

where $\mathbf{M} = (M_x, M_y)$ is a normal pointing into the liquid phase. We only present the problem of integrating over C_l, since C_v involves an analogous procedure. If $|M_x| < \xi$, for a small tolerance ξ, the interface is approximately horizontal; thus the integration of $\mathcal{F}(y)$ over C_l becomes:

$$\frac{1}{\Delta_C^2}\int\int_{C_l}\mathcal{F}(y)dxdy = \frac{1}{\Delta}\int_{y_c-\Delta/2}^{y_c-\Delta/2+T\Delta}\mathcal{F}(y)dy$$

On the other hand, if $|M_y| < \xi$, the interface is approximately vertical, and the integration over C_l becomes:

$$\frac{1}{\Delta_C^2}\int\int_{C_l}\mathcal{F}(y)dxdy = \frac{T}{\Delta}\int_{y_c-\Delta/2}^{y_c+\Delta/2}\mathcal{F}(y)dy$$

We can now proceed to provide general formulas when $|M_y| > \xi$ and $|M_x| > \xi$. Since $\mathcal{F}(y)$ is independent of x, the sign of the interfacial slope is irrelevant, so, without loss of generality, suppose that $M_x/M_y > 0$. Define the following values:

$$\begin{aligned}
x_a &= x_c - \Delta_C/2 \\
x_b &= \max\left(\frac{-M_y(y_c+\Delta_C/2)+\alpha}{M_x}, x_c-\Delta_C/2\right) \\
x_d &= \min\left(\frac{-M_y(y_c-\Delta_C/2)+\alpha}{M_x}, x_c+\Delta_C/2\right) \\
x_e &= x_c + \Delta_C/2
\end{aligned}$$

If $M_y < 0$, the integration over C_l can be expressed as follows:

$$\frac{1}{\Delta_C^2}\int\int_{C_l}\mathcal{F}(y)dxdy = \frac{1}{\Delta_C^2}\left[(x_b-x_a)\int_{y_c-\Delta/2}^{y_c+\Delta/2}\mathcal{F}dy + \int_{x_b}^{x_d}\int_{y_c-\Delta/2}^{-M_x/M_yx+\alpha/M_y}\mathcal{F}dydx\right] \quad (5.33)$$

On the other hand, if $M_y > 0$, the integration over C_l is given by:

$$\frac{1}{\Delta_C^2}\int\int_{C_l}\mathcal{F}(y)dxdy = \frac{1}{\Delta_C^2}\left[\int_{x_b}^{x_d}\int_{-M_x/M_yx+\alpha/M_y}^{y_c+\Delta/2}\mathcal{F}dydx + (x_e - x_d)\int_{y_c-\Delta/2}^{y_c+\Delta/2}\mathcal{F}dy\right] \quad (5.34)$$

Thus, in two dimensions, the general process of integration reduces to integration over two regions. Note again that $\mathcal{F}(y)$ is known exactly, so that the integrals in Eqs. (5.33)-(5.34) can be computed exactly, in contrast to the large error for Method I in Eq. (5.31). Therefore, we conclude that regarding approximation of Eq. (5.29), Method II is superior. For example, for a single phase fluid, or when the interface is flat, Eq. (5.32) is exact. We will consider both Method I and Method II in what follows and discuss their performance.

Our computational domain is rectangular, with $x \in (0, x_{max})$ and $y \in (h_c, y_{max})$. Throughout the remainder of the chapter, we will impose a homogeneous Neumann boundary condition on all boundaries for the pressure, p. For the velocity field, we will apply a homogeneous Neumann boundary condition at all boundaries except $y = h_c$, where we will apply one of the following two boundary conditions; the no-slip, no-penetration condition by setting $\mathbf{u}$ to 0 on the substrate:

$$(u, v)|_{y=h_c} = (0, 0)$$

or a free-slip condition by:

$$\partial_y u|_{y=h_c} = 0 \quad v|_{y=h_c} = 0$$

The boundary condition for the van der Waals force is straightforward. At $y = h_c$, we set

$$\mathbf{F}_{I,II}|_{y=h_c} = K_{ls}\mathcal{F}(h_c)$$

At $y = y_{max}$, we set

$$\mathbf{F}_{I,II}|_{y=y_{max}} = K_{vs}\mathcal{F}(y_{max})$$

The boundary condition for the volume fraction, T, is again homogeneous Neumann on all boundaries, except on the bottom boundary, where we apply

$$T|_{y=h_c} = 1$$

which is equivalent to taking the bottom boundary to always be wetted with the liquid phase.

5.4 Results

In this section, we consider simulations of the full Navier-Stokes equations in which contact angles have been imposed using the van der Waals force, which is included using Methods I and II described in Section 5.3. Our simulation setup consists of a drop on an equilibrium film, initially at rest, which then relaxes to equilibrium under the influence of the van der Waals force. We compare Methods I and II for a drop which is initially close to its equilibrium contact angle, as predicted by Eq. (5.27), as well as for a spreading drop which is initially far from its equilibrium. Furthermore, we consider the effect of equilibrium film thickness for small, intermediate, and large contact angles, using Method II.

In simulations, drops are surrounded by an equilibrium film of thickness $\bar{h^*} := h^* - h_c$ defined by $y < h^*$, where h_c is the amount the force is translated by in Eq. (5.17). The initial profile is given by the following:

$$\left\{(x, y) : x^2 + (y + R\cos\theta_i - h^*)^2 < R^2 \text{ or } y < h^*\right\} \tag{5.35}$$

Here R is chosen so that the total area of the circular cap is equal to $A_0 = \pi 0.75^2/2$. The quantity θ_i is the initial contact angle of the drop. In all simulations, we fix the

ratio of these length scales so that $h^* = 2h_c$. Various values of the exponents m and n in Eq. (5.23) can be found in the literature, in particular $(m, n) = (9, 3),\ (4, 3),\ (3, 2)$ have been used in the context of the disjoining pressure in thin films [18, 40], the former corresponding to the 12-6 Lennard Jones potential. In this chapter we will restrict our attention to $(m, n) = (3, 2)$, which was shown to lead to favorable agreement with experiments involving liquid metal films [40]. Different exponents may affect the structure of the contact line region and the pressure distribution, but do not impact significantly the results presented here.

There are four contact angles that we consider in this section. The initial contact angle, θ_i, as in Eq. (5.35), specifies the angle formed by the tangent of the initial circular profile with the equilibrium film at the point where they meet. The (time dependent) apparent contact angle is denoted θ, and the numerical equilibrium angle θ_{num} is the value of θ when the system under consideration is in equilibrium; θ is measured by a circle fit procedure described below. Finally, we refer to the imposed contact angle, θ_{eq}, which we use to specify $K_{vs} - K_{ls}$ via Eq. (5.27); the only relevant quantity is the difference between K_{vs} and K_{ls}, but for definiteness, we set $K_{vs} = 1.1\Delta K(\theta_{eq})$ and $K_{ls} = 0.1\Delta K(\theta_{eq})$. The value of θ_{eq} differs from θ_{num} in simulations because h^* is small but non negligible relative to the thickness of the drop.

We measure θ according to the following procedure. A drop has a circular cap shape that transitions smoothly to the equilibrium film. We define the contact angle in this context in the following way: let $\pm x_{inf}$ represent the points of inflection of the drop profile. We perform a least squares fit of a circle to the profile over the interval $(-x_{inf}, x_{inf})$. The point at which the fitted circle intersects the equilibrium film is called the contact point (in three dimensions, this is the contact line). θ is measured as the angle the fitted circle makes with the equilibrium film at the contact point.

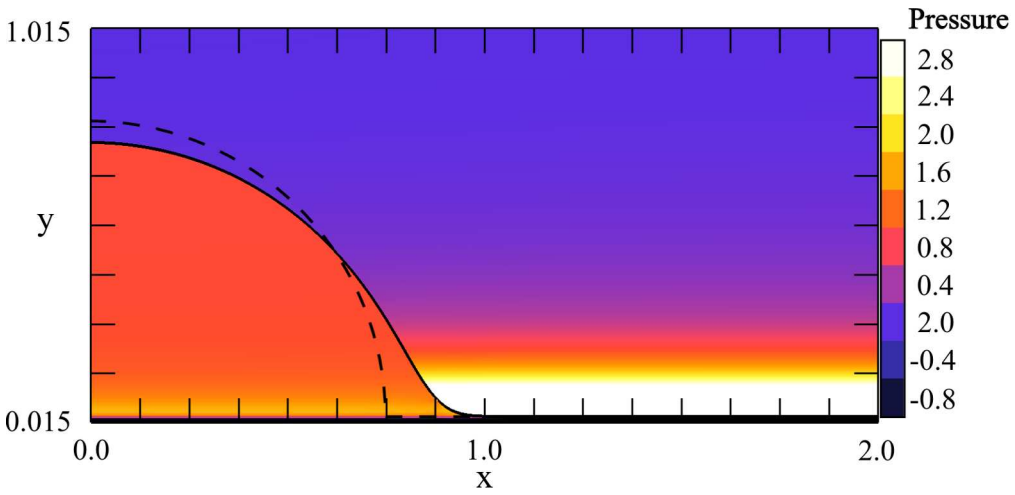

Figure 5.3 Pressure distribution for a drop with $\theta_{eq} = \pi/2$, $h^* = 0.03$, at equilibrium. The pressure is normalized by the (non-dimensional) capillary pressure of the equilibrium drop, which is given by the curvature of the interface far from the contact point, where it is approximately circular. The solid black curve shows the Volume of Fluid reconstructed interface, and the dashed curve is the initial profile; $\Delta = 1/256$.

We first investigate a static drop, with $h^* = 0.03$ and $\theta_i = \pi/2$, which is then allowed to relax to its equilibrium shape. The dimensionless numbers are set to be $We_l = We_v = Ca_l = Ca_v = 0.05$. We set the material parameters to be the same in both fluid phases in order to restrict our attention to a smaller parameter space, so that we can focus on the properties of Methods I and II. Note that since the expression determining θ_{eq}, Eq. (5.27), does not depend on the fluid parameters, this choice does not affect the equilibrium shape. The computational domain is $(x, y) \in [0, 2] \times [h_c, 1 + h_c]$; the domain is resolved at a constant resolution. A no-slip boundary condition is imposed on the solid boundary, $y = h_c$.

Figure 5.3 shows such a drop at equilibrium (with the contact angle imposed using Method II). The equilibrium film has negative pressure with very high absolute value, and its thickness at equilibrium differs from $\bar{h}^*$ by about 3%. With this h^*, there is a noticeable difference between the true equilibrium contact angle found by simulations, θ_{num}, and the imposed angle θ_{eq}. The effect of h^* on the equilibrium drop shape will be considered below.

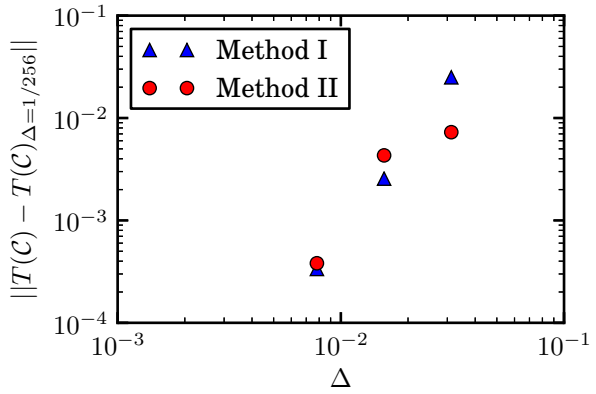

Figure 5.4 The convergence of the L^1 norm of the difference between $T(\mathcal{C})$ at Δ and $\Delta = 1/256$, for a drop at equilibrium with $\theta_{eq} = \pi/2$, $h^* = 0.03$, with a uniform mesh size Δ.

Figure 5.4 shows the convergence for Methods I and II for a uniform mesh. Simulations are run until time $t = 1.75$, with a constant time step of $\Delta t \approx 2.8 \times 10^{-5}$; the stability constraint due to the explicit discretization of the surface tension dominates in this velocity regime, and this time step ensures that this constraint is satisfied for all resolutions we consider (see [67]). For two sets of volume fractions T_1 and T_2 such that T_2 is computed on a quad-tree Q with mesh-size Δ_Q, the L^1 norm is computed according to the following formula:

$$||T_1(\mathcal{C}) - T_2(\mathcal{C})|| = \sum_{\mathcal{C} \in Q} |T_1(\mathcal{C}) - T_2(\mathcal{C})| \Delta_Q^2 \tag{5.36}$$

In this case $\Delta_Q = 1/256$, and $T_1(\mathcal{C})$ is equal to T_1 on the largest cell containing $\mathcal{C}$. For reference, $\Delta = 1/32$ is about h^*, so that the low resolution case is not even resolving the equilibrium film. Both methods perform comparably well at $\Delta = 1/64, 1/128$, with Method I converging slightly faster. However, at low resolutions, $\Delta = 1/32$, Method II performs significantly better.

We now move onto the question of how a drop behaves when θ_i is far from θ_{num}. The initial shape of the drop is as above, with $h^* = 0.03$, $R = 0.75$, so that $\theta_i = \pi/2$. At $y = h_c$, we use free-slip since it allows the drop to reach its steady

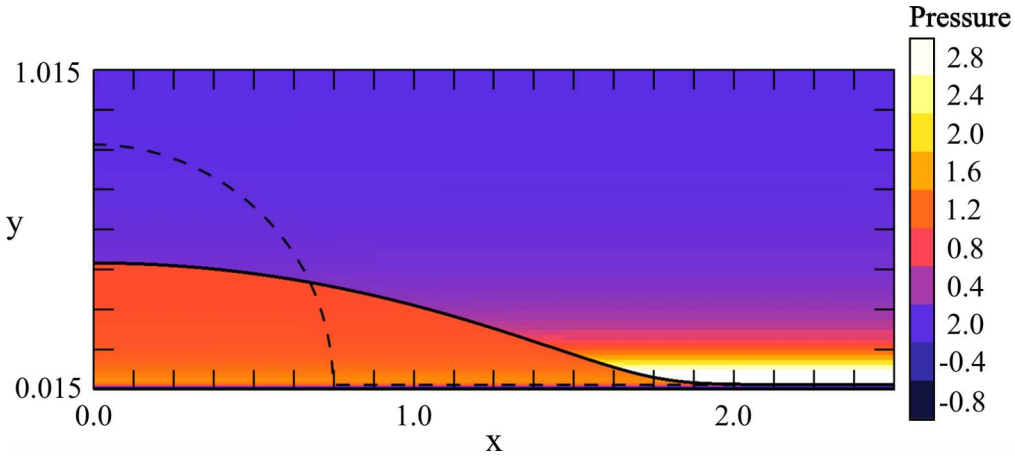

Figure 5.5 Pressure distribution for a drop at equilibrium with $\theta_{eq} = \pi/6$. Initially, $\theta_i = \pi/2$, and the drop spreads to its equilibrium configuration, defined by $\theta_{eq} = \pi/6$. The initial profile is shown by the dashed curve. As in Figure 5.3, the pressure is normalized by the capillary pressure of the equilibrium drop; $\Delta = 1/256$.

state more quickly, reducing computational time. The simulation domain is $(x, y) \in [0, 4] \times [h_c, 1 + h_c]$. For these simulations, we will set $We_l = We_v = Ca_l = Ca_v = 1$. We note that even with this choice of parameters, the dimensionless contact point speed is sufficiently small so that surface tension effects still dominate over viscous effects (or precisely speaking, the capillary number defined based on the speed of the contact point is still small). As before, we use the same material parameters for both phases, and note that, provided that the capillary number is small, varying the ratios between the phases will only affect the relaxation time; we will expand on this point below. Here, we impose a small contact angle of $\theta_{eq} = \pi/6$. Unlike the above, we use an adaptive mesh which refines regions to a level of Δ_{max} near the liquid/vapor interface, or if there is a high gradient in $\mathbf{F}_B$. We will vary Δ_{max} in what follows to study the convergence with respect to the maximum resolution. Figure 5.5 shows the initial and equilibrium profiles and pressure distribution when the drop reaches equilibrium, computed using Method II. The pressure inside the liquid phase is near unity, while the pressure in the vapor phase just above the equilibrium film

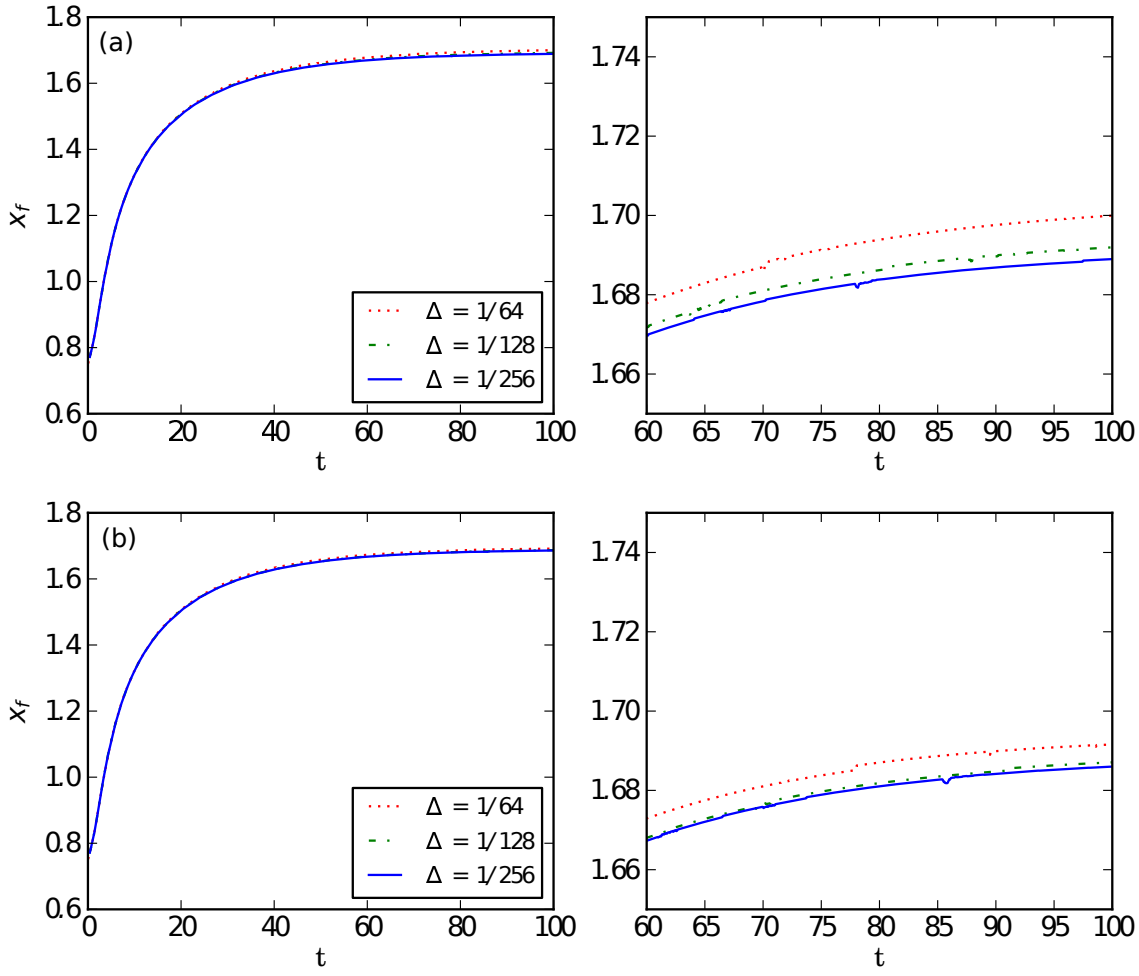

Figure 5.6 Front location for the spreading drop for varying resolution for (a) Methods I and (b) Method II. The maximum mesh resolution is $\Delta_{max} = \Delta$.

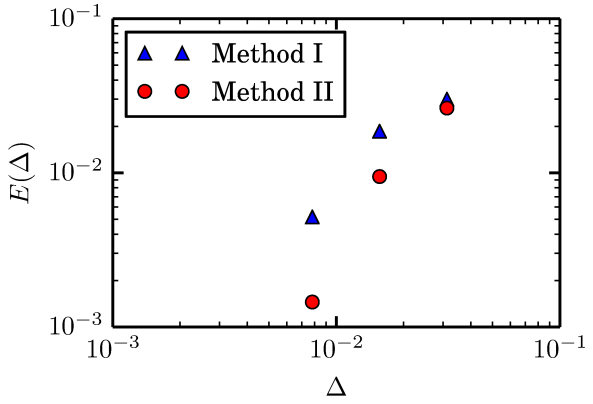

Figure 5.7 Convergence of the front location of spreading drops, for Methods I and II, where the error is estimated according to Eq. (5.37).

is five times the capillary pressure. The equilibrium contact angle in Figure 5.5 is $\theta_{num} \approx \pi/7$.

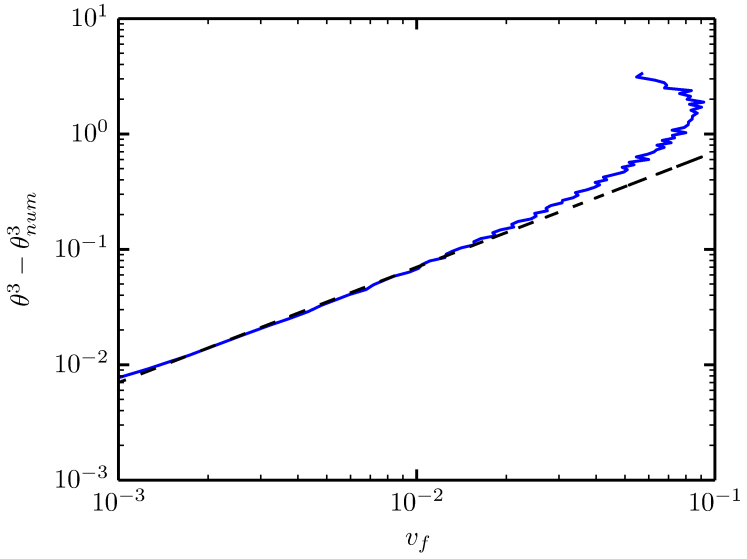

Figure 5.8 Cox-Voinov law for the spreading drop. The blue (solid) curve shows simulation results for a drop spreading from $\theta_i = \pi/2$ to equilibrium, with an imposed contact angle of $\theta_{eq} = \pi/6$ using Method II. The black (dashed) line is proportional to v_f, and the agreement with the blue (solid) curve shows that the drop spreading approximately satisfies the Cox-Voinov law.

Figure 5.6 shows the front locations for the spreading drops as a function of time for Method I and Method II. Both methods show broadly similar results, with Method II appearing to slightly outperform Method I in terms of convergence. In order to compute the convergence, we calculate the error as:

$$E(\Delta)_{I,II} = \frac{1}{100}\int_0^{100} |x_f(t)_\Delta - x_f(t)_{\Delta=1/256}|dt \tag{5.37}$$

Here $x_f(t)_\Delta$ is the front location computed with $\Delta_{max} = \Delta$, and $x_f(t)_{\Delta=1/256}$ is the front location computed with $\Delta_{max} = 1/256$. Figure 5.7 shows the errors. Method II displays significantly better convergence for the front location as a function of time.

We briefly compare the qualitative behavior of the spreading drop to the well known Cox-Voinov law [92], discussed in Chapter 3. For a drop displacing another

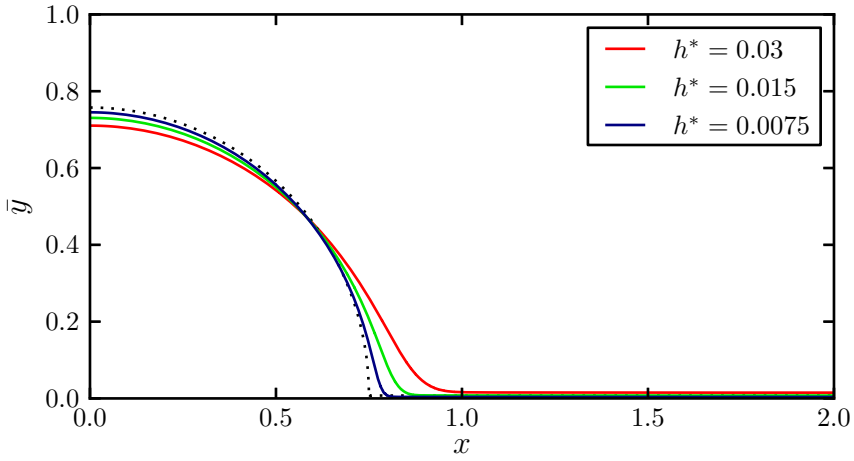

Figure 5.9 Equilibrium profiles with $\theta_{eq} = \theta_i = \pi/2$ for various values of h^*. The black (dotted) profile shows the initial condition for $h^* = 0.015$. We plot $\bar{y} = y - h_c$ so that for each curve the y range is $(0, 1)$.

immiscible fluid on a solid surface, the speed of the contact point, v_f, is related to θ_i and θ_{num} to leading order by [17]:

$$\theta^3 - \theta_{num}^3 \propto v_f \tag{5.38}$$

Note that Eq. (5.38) is derived under the assumption that $\mu_l v_f/\sigma \ll 1$, i.e. that the capillary number defined using the front velocity is small. Provided that one is in this regime, the choice of material parameters only impacts the constant of proportionality in Eq. (5.38). Figure 5.8 shows v_f versus $\theta^3 - \theta_{num}^3$ using Method II, for $\Delta_{max} = 1/256$. The blue (solid) line shows the numerical results, and the black (dashed) line shows the slope expected if the Cox-Voinov law is obeyed. We see that after initial transients v_f decreases with $\theta^3 - \theta_{num}^3$, and the drop spreading approximately satisfies the Cox-Voinov law for $v_f \in (10^{-2}, 10^{-3})$.

Next, we turn our attention to the precise value of the contact angle. As shown in Figure. 5.3 and 5.5, the actual equilibrium contact angle, θ_{num}, is generally smaller than the imposed angle θ_{eq}. This is due to the fact that Eq. (5.27) is derived under the assumption of small h^*, while in our simulations the ratio of drop radius and h^*

Table 5.1 Dependence of θ_{num} on h^*. We Calculate θ_{num} Using a Circle Fit. The Third Column gives the Relative Difference Between θ_{num} and θ_{eq}. The Fourth Column is the L^1 Norm of the Difference Between the Initial Volume Fractions $T_i(\mathcal{C})$ and the Equilibrium $T_f(\mathcal{C})$.

h^*	θ_{num}	$\lvert\theta_{num} - \theta_{eq}\rvert/\theta_{eq}$	$\lvert\lvert T_i(\mathcal{C}) - T_f(\mathcal{C})\rvert\rvert$
0.03	1.37	0.125	0.05
0.015	1.47	0.066	0.03
0.0075	1.53	0.025	0.009

is about 25. To confirm the above statement, we analyze in more detail the resulting contact angles as h^* is varied. We set $\theta_{eq} = \pi/2$ using Method II, and the resolution is fixed at a uniform $\Delta = 1/256$. The value of h^* varies over 0.03, 0.015, and 0.0075. The initial condition is imposed with $\theta_i = \pi/2$ as in Eq. (5.35). The drop is again permitted to relax to its equilibrium with a fixed time step for 1.75 units of time. Figure 5.9 shows the equilibrium profiles for various values of h^*. The black (dotted) profile is the initial condition for $h^* = 0.015$, and is included as a reference. As h^* is decreased, the equilibrium profiles are characterized by contact angles closer to θ_{eq}.

We quantify the dependence of θ_{num} on h^* in Table 5.1. As before, we compute the contact angle θ_{num} using a circle fit of the drop after 1.75 units of time, at a fixed time step for all simulations. As h^* is reduced, the calculated θ_{num} approaches $\theta_{eq} = \pi/2$. The relative difference between θ_{num} and θ_{eq} reduces with h^* approximately linearly. These measures however depend on the accuracy of the estimation of θ_{num}; to analyze the convergence more directly, we compare the volume fractions of the initial condition, $T_i(\mathcal{C})$, with the equilibrium state $T_f(\mathcal{C})$, using an L^1 norm computed as Eq. (5.36). Initially, $\theta_i = \theta_{eq}$, so this comparison provides a measure of the difference between θ_{num} and θ_{eq}. This difference again decreases approximately linearly with h^*.

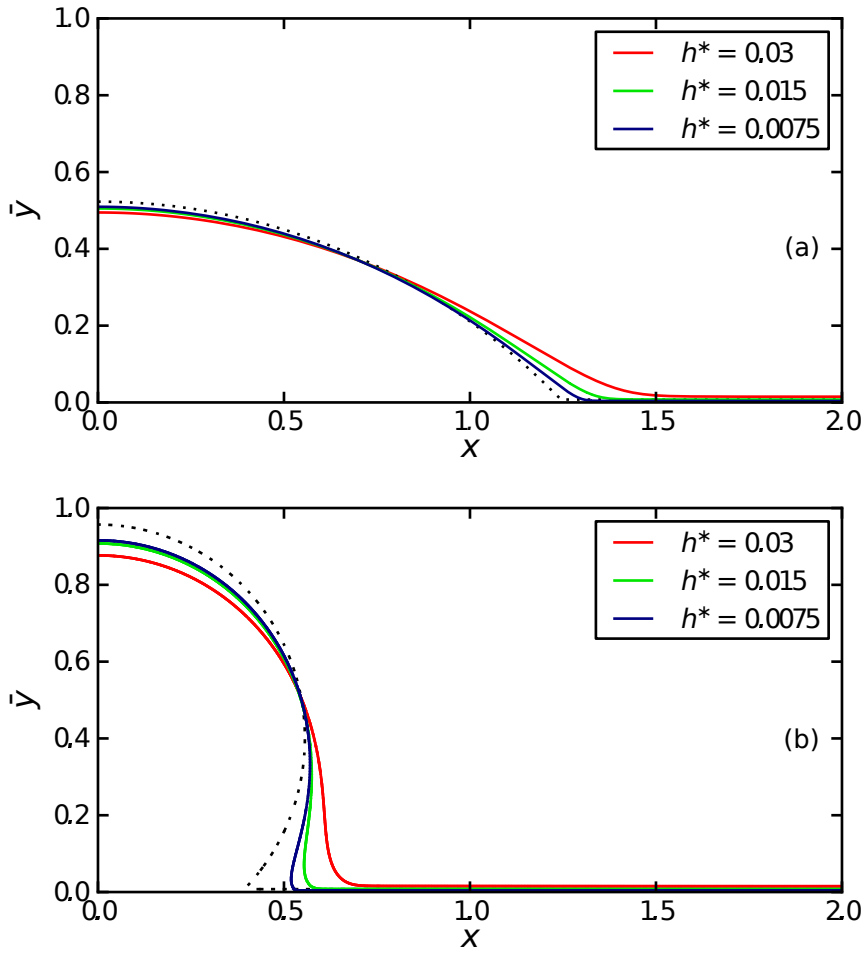

Figure 5.10 Dependence of the drop profile at equilibrium on h^* for (a) $\theta_{eq} = \pi/4$ and (b) $\theta_{eq} = 3\pi/4$. The black (dotted) profile shows the initial condition for $h^* = 0.015$. As in Figure 5.9, we plot $\bar{y} = y - h_c$ so that for each curve the y range is $(0, 1)$.

Finally, we consider the effects of varying h^* for θ_{eq} other than $\pi/2$. Figure 5.10 (a) shows the equilibrium drop profiles for $\theta_{eq} = \theta_i = \pi/4$ and varying h^*, and Figure 5.10 (b) shows the same for $\theta_{eq} = \theta_i = 3\pi/4$. For $\theta_{eq} = \pi/4$, as h^* decreases, the profile quickly converges to the initial condition and hence the contact angle to θ_{eq}, as seen by the comparison of the black (dotted) curve with that of $h^* = 0.0075$ in Figure 5.10 (a). For $\theta_{eq} = 3\pi/4$, it can be seen that even for $h^* = 0.0075$, the drop profile still shows some difference between θ_{num} and θ_{eq}. Nonetheless, this plot demonstrates a central advantage of our methods: θ_{num} larger than $\pi/2$ can be simulated with the van der Waals force.

5.5 Conclusions

In this chapter, we have described a novel approach for including the fluid/solid interaction forces, into a direct solver of the Navier-Stokes equations with a Volume of Fluid interface tracking method. The model does not restrict the contact angles to be small, and therefore, can be used to accurately model wetting and dewetting of fluids on substrates characterized by arbitrary contact angles. We study the problem of a two-dimensional drop on a substrate and compare the results with the Cox-Voinov law for drop spreading. These validations and results illustrate the applicability of our proposed method to model flow problems involving contact lines. Furthermore, our approach has the desirable property of regularizing the viscous stress singularity at a moving contact line since it naturally introduces an equilibrium fluid film.

We have considered two alternative finite-volume discretizations of the van der Waals force term that enters the governing equations to include the fluid/solid interaction forces. These two methods are complementary in terms of their accuracy and the ease of use, and therefore the choice of the method could be governed by the desired features of the results. In particular, Method I discretizations can be straightforwardly extended to the third spatial dimension. However, we have shown

that, when implementing Method I, to guarantee accurate results, sufficient spatial resolution of the computational mesh must be used. We also show that Method II does not suffer accuracy deterioration at low mesh resolutions, and is therefore, superior to Method I, and furthermore outperforms Method I for spreading drops at all resolutions, albeit being more involved to implement.

The presented approach opens the door for modeling problems that could not be described so far, in particular dewetting and associated film breakup for fluids characterized by large contact angles. Furthermore, the model permits the study of the effects of additional mechanisms, such as inertia. We will consider these problems in future work.

CHAPTER 6

A REDUCED PRESSURE VOLUME OF FLUID METHOD FOR FLUID/SOLID INTERACTION: CONTACT LINES AND FILM RUPTURE

6.1 Model

In this chapter, we will return to the computational method which was presented in Chapter 5, and develop and apply a significant improvement to it. The basis of this method is to rewrite the governing equations (Eq. (5.19)) according to a *reduced pressure* formulation, which permits the body force to be transformed into a surface force. As we will demonstrate, this dramatically improves the computational performance, and permits the study of systems, whose simulation would have been impractical using the method in Chapter 5.

During the discussion in Chapter 5, an important drawback arose: while Gerris permits the use of an adaptive mesh, the large pressure gradients in the vicinity of the substrate required high resolutions. In all of the results in that chapter, the computational mesh was either uniform, or resolved everything which was near the substrate at higher resolutions, irrespective of whether there were any interesting dynamics in those regions. A second, relatively minor, drawback was the introduction of the cutoff height h_c, below which the fluid/solid interaction was not computed in order to avoid the singularity int the force term (Eq. (5.10)). Both of these problems can be completely avoided through a refinement of the method.

Our setup closely follows the one considered in Chapter 5, consisting of two fluid phases occupying the region $y > 0$, interacting with a solid substrate occupying $y < 0$. Each particle of fluid phase i interacts with the solid substrate by means of

Eq. (5.9), which we rewrite as follows for clarity:

$$\Phi_{is}(y) = \mathcal{K}_{is}\left[\left(\frac{h^*}{y}\right)^m - \left(\frac{h^*}{y}\right)^n\right] = \mathcal{K}_{is}F(y) \tag{6.1}$$

The governing equations are the same as Eq. (5.19):

$$\rho(\chi)\frac{D\mathbf{u}}{Dt} = -\nabla p + \nabla\cdot\left[\mu(\chi)\left(\nabla\mathbf{u} + \nabla\mathbf{u}^\top\right)\right] + \gamma\kappa\delta_s\mathbf{n} - \nabla\left(\mathcal{K}(\chi)F(y)\right) \tag{6.2}$$

Equation (6.2) is subject to the incompressibility condition, Eq. (2.2). We apply the no-slip, no-penetration condition, Eq. (2.3) at the solid surface, $y = 0$, throughout this chapter. We have rewritten the interaction strength in terms of the characteristic function according to the following:

$$\mathcal{K} = \mathcal{K}_{ls}\chi + \mathcal{K}_{vs}(1-\chi)$$

We pursue a different nondimensionalization of Eq. (6.2) than that used in Chapter 5, In order to nondimensionalize, Eqs. (6.2)-(2.3), we introduce the length scale L, and define the time scale as the capillary time:

$$\mathcal{T} = \frac{\mu L}{\gamma}$$

The dimensionless variables are defined as follows:

$$\begin{aligned}
\tilde{x} &= \frac{x}{L} & \tilde{y} &= \frac{y}{L}\\
\tilde{z} &= \frac{z}{L} & \tilde{t} &= \frac{t}{\mathcal{T}}\\
\tilde{h}^* &= \frac{h^*}{L} & \tilde{\mathbf{u}} &= \frac{\mathbf{u}\mathcal{T}}{L}\\
\tilde{p} &= \frac{Lp}{\gamma} & \tilde{\kappa} &= L\kappa\\
\tilde{\rho} &= \frac{\rho}{\rho_l} & \tilde{\mu} &= \frac{\mu}{\mu_l}\\
\tilde{\delta_s} &= L\delta_s
\end{aligned}$$

With these scales, and dropping the tildes, the dimensionless Navier-Stokes equations are as follows:

$$\frac{1}{Oh^2}\rho\frac{D\mathbf{u}}{Dt} = -\nabla p + \nabla\cdot\left[\mu(\nabla\mathbf{u}+\nabla\mathbf{u}^T)\right] + \kappa\delta_s\mathbf{n} - \nabla\left(K(\chi)F(y)\right) \tag{6.3}$$

where

$$Oh = \frac{\mu}{\sqrt{\rho_l\gamma L}}$$

and $K(\chi)$ is the same as in Eq. (5.26) Here, Oh is the Ohnesorge number, and the length scale, L, is chosen according to the problem under consideration. The variables ρ and μ take the value of 1 in the liquid phase, and ρ_v/ρ_l or μ_v/μ_l in the vapor phase, respectively.

The solution of Eq. 6.3 was discussed extensively in Chapter 5. The two methods described in that chapter we refer to here as "body force methods", which we abbreviate B–F throughout this chapter; although these methods discretized the liquid/solid interaction term differently, they were found to be substantially similar in their overall properties, and for our purposes here, may be treated interchangeably. For definiteness, when we refer to the "body force method" in this chapter, we exclusively refer to Method II from Chapter 5. In that chapter, we found that the liquid/solid term presents a challenge owing to the fact that it diverges as $y \to 0$. Consequently, when using B–F methods, regions of the domain near the substrate require high resolutions in order to obtain reasonably accurate results. This significantly limits the use of adaptive meshes; adaptive meshes can dramatically improve the performance of Navier-Stokes simulations by using higher resolution meshes only in regions of the domain where such accuracy is necessary to capture the dynamics. In two dimensions, simple problems are feasible, however in three dimensions the computational cost of resolving so much of the domain is impractical.

In this section, we show that the computational task is dramatically simplified by reformulating the body force term in Eq. (6.3) as a force which acts only on the interface. First, we define $p^* = p + K_l\chi F(y) + K_v(1-\chi)F(y)$, so that

$$-\nabla p^* = -\nabla p - (K_l\chi + K_v(1-\chi))\nabla F + (K_v - K_l)\delta_s \mathbf{n} F(y)$$

where $\delta_s \mathbf{n} = \nabla\chi$, in a distributional sense. Substituting into Eq. (6.3), we obtain what we refer to as the reduced pressure formulation:

$$\frac{1}{Oh^2}\rho\frac{D\mathbf{u}}{Dt} = -\nabla p^* + \nabla\cdot\left[\mu(\nabla\mathbf{u} + \nabla\mathbf{u}^T)\right] + (\kappa + KF(y))\delta_s\mathbf{n} \tag{6.4}$$

where $K = (K_v - K_l)$ (note that only this difference is relevant, rather than individual value of each K). We refer to numerical solutions of Eq. (6.4) as obtained using the "reduced pressure method" throughout this chapter, and occasionally abbreviate this as R–P. The liquid/solid interaction gives rise to the contact angle, as we discussed at length in Chapter 5. Equation (5.15), in the present notation, becomes

$$K = \frac{(1-\cos\theta_{eq})}{h^*}\left(\frac{(m-1)(n-1)}{m-n}\right) \tag{6.5}$$

As before, the contact angle is measured via a circle fit; at equilibrium, the contact angle that is measured by this procedure is termed θ_{num}. There is, in general, a difference between θ_{num} and θ_{eq}, however this difference tends to vanish with smaller h^*.

In addition to the contact angle, the liquid/solid interaction gives rise to another phenomenon that we consider in depth in this chapter, which is the spontaneous rupture of a thin liquid film. Our account of film rupture comes from [24], which studied the rupture of films in the context of long–wave theory. As discussed in more detail in Chapter 3, the Navier-Stokes equations can be simplified into an equation for the liquid film thickness under the following assumptions:

1. The flow is characterized by a horizontal length scale, x_c, and a vertical length scale, h_c, such that $h_c \ll x_c$.

2. Interfacial slopes, $\nabla_{x,z} h$, are vanishingly small; here $\nabla_{x,z}$ reduces to ∂/∂_x in 2D, and is the gradient in x and z in 3D.

3. Inertial effects are negligible ($Re \ll 1$.)

The second assumption has the important corollary that the contact angles are small. We discussed the use of liquid/solid interaction terms in the long–wave model in Chapters 3 and 5; the disjoining pressure term given by Eq. (3.5) in the notation of this chapter takes the form

$$\Pi(h) = KF(h) \tag{6.6}$$

The dimensionless long–wave equation corresponding to Eq. (6.3) is given by [74, 75]

$$3h_t + \nabla_{x,z} \cdot (h^3 \nabla_{x,z} \nabla^2 h) + \nabla_{x,z} \cdot \left[h^3 \nabla_{x,z} KF(y)\right] = 0 \tag{6.7}$$

(note that Eq. (6.7) is formally identical to Eq. (3.4).) A linear stability analysis shows that if the initial film thickness is h_0, and this is perturbed by a mode with infinitesimal amplitude, ϵ, of the form $\exp(i(kx + lz))$, then the initial perturbation will grow or decay with a growth rate

$$\beta = \frac{h_0^3 (k^2 + l^2)(k_c^2 - (k^2 + l^2))}{3} \tag{6.8}$$

where k_c is the critical wavenumber, given by

$$k_c^2 = -\frac{K}{h_0} \left[m \left(\frac{h^*}{h_0} \right)^m - n \left(\frac{h^*}{h_0} \right)^n \right] \tag{6.9}$$

Note that if $k_c^2 < 0$, then $\beta < 0$, and there is no instability for any wavenumber. If $k_c^2 > 0$, all modes with wavenumber $k < k_c$ are unstable, and those with $k > k_c$ are

stable. Associated with Eq. (6.8) is a wavenumber of maximum growth, k_{max}, and the corresponding maximum growth rate, β_{max}, given by:

$$k_{max} = \frac{k_c}{\sqrt{2}} \tag{6.10}$$

$$\beta_{max} = \beta(k^2 + l^2 = k_{max}^2) = \frac{k_c^4}{12} \tag{6.11}$$

We will frequently make reference to the wavelength of maximum growth, defined by $\lambda_{max} = 2\pi/k_{max}$. Equations (6.9) - (6.11) imply the following important features of instability:

1. The wavenumber of maximum growth, k_{max}, scales with $\sqrt{1-\cos\theta_{eq}}$. Large contact angles imply larger k_{max}, and a corresponding decrease in λ_{max}.

2. The maximum growth rate, β_{max}, scales with $(1-\cos\theta_{eq})^2$. Large contact angles dramatically increase the growth rate of the dominant mode, and thus reduce the time it takes for films to break up.

In order to facilitate discussion, we will occasionally refer to the Reynolds number and the Capillary numbers based on the timescale of the breakup; we define these as

$$Re = \frac{\rho L^2 \beta_{max}}{\mu} \qquad Ca = \frac{\mu L \beta_{max}}{\gamma} \tag{6.12}$$

The reduced pressure method discussed in this chapter shows three important strengths. First, it possesses the most important feature of the body force method discussed in Chapter 5: that is, by including long range liquid/solid interactions, spontaneous film breakup can occur, described by the LSA above. Such breakups are particularly important at the nanoscale; see for example [40]. The second major advantage of this method is that by absorbing the entire contribution of the liquid/solid interaction into a surface force, the main weakness of the body force method is avoided. That is, as discussed previously, B–F methods limit the usefulness

of an adaptive mesh due to the singular liquid/solid interaction, while the reduced pressure method effectively converts this force into a y dependent modification of the curvature term, and thus no additional resolution is required away from the interface. Full advantage may be taken of adaptive meshes, in contrast to body force methods. Third, the reduced pressure method is relatively simple to implement, owing to the fact that it is essentially a modification of the curvature term in the Navier-Stokes equations.

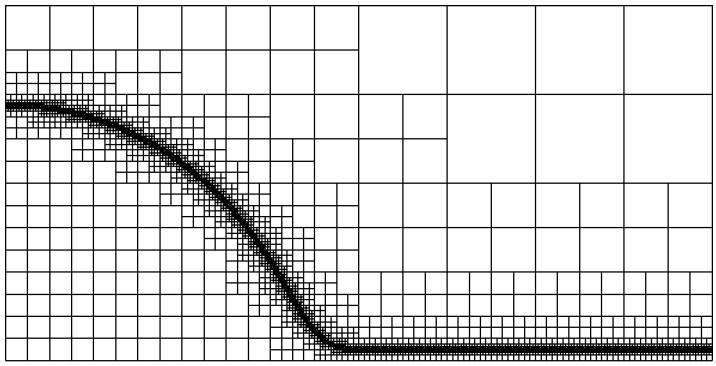

Figure 6.1 Illustration of the adaptive mesh used throughout this chapter. The interface is the only portion of the domain that it is necessary to resolve at high resolution, due to the fact that the fluid/solid interaction is included as an interfacial force.

We solve Eq. (6.4) using the software package Gerris [67], described in detail in [66]. The mesh consists of a quad tree (in 2D) or an octree (in 3D), that decomposes the domain into square control volumes, which we refer to as cells (see Figure 6.1). We use an adaptive mesh for all simulations, refining the interface to a resolution of Δ_{max}, and lower resolutions far away from the interface. We implement the R–P method in Gerris according to the following procedure: replace the interface curvature κ, approximated at cell centers, by

$$\kappa \leftarrow \kappa + KF(y)$$

Table 6.1 Comparison of the Convergence in Mesh Between the Reduced Pressure Method (R–P) and Method II Described in Chapter 5 (B–F). Δ is the Smallest Cell Size Used in the Simulations, and the Second and Third Columns Give the Error Measured as the L^1 Norm of the Difference Between the Equilibrium Profile and the Profile Calculated with $\Delta = 1/2^8$.

Δ	R–P	B–F
$1/2^5$	6.1×10^{-2}	7.0×10^{-3}
$1/2^6$	2.6×10^{-3}	4.3×10^{-3}
$1/2^7$	8.0×10^{-4}	3.8×10^{-4}

Here y is the y-coordinate of the center of mass of the liquid in the computational cell. Note that the R–P method is not specific to Volume of Fluid - it can be used with any solver of the two phase Navier-Stokes equations.

6.2 Results

6.2.1 Contact Angles

We first demonstrate that the method under consideration can yield contact angles as accurately as the methods presented in Chapter 5. To show that this is the case, we reproduce simulations of drops in that chapter, by simulating 2D drops, with $Oh = (0.05)^{-1/2}$, and the initial fraction is set to be the following:

$$\{(x, y) : x^2 + (y + R\cos\theta_i - h^*)^2 < R^2 \text{ or } y < h^*\}$$

Thus the initial profile is a circular cap sitting on top of an equilibrium film, of thickness h^*, such that it intersects this film with angle θ_i. The value of R is chosen so that the total area of the circular cap is equal to $A_0 = \pi 0.75^2/2$. For simplicity, for our first tests, we set $\theta_{eq} = \theta_i = \pi/2$. The drop is then allowed to relax to equilibrium, and we measure θ_{num} via the circle fit method described in Chapter 5.4. Since for

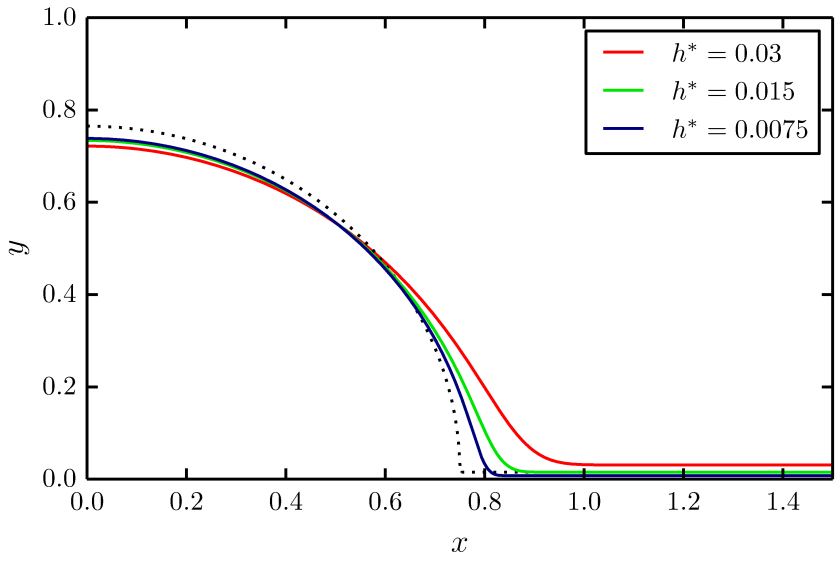

Figure 6.2 Effect of h^* on the profile when $\theta_i = \theta_{eq} = \pi/2$. The dotted line shows the initial profile for $h^* = 0.015$.

small h^*, θ_{num} is close to θ_{eq}, the drop profile at this equilibrium is close to its initial condition.

Table 6.1 compares the convergence of the equilibrium drop profile as a function of the minimum mesh size, for drops simulated using the reduced pressure method and the body force method of Chapter 5. The reduced pressure simulations are resolved to a resolution $\Delta_{max} = \Delta$ on an adaptive mesh as shown in Figure 6.1, while the body force method simulations are refined uniformly with mesh size Δ. The error is measured as the L^1 norm of the error in the profile shape. The equilibrium film thickness is $h^* = 0.03$. Despite the fact that the body force simulations were run with a uniform mesh, the reduced pressure method performs comparably well in convergence in mesh to the body force method when Δ is small.

Figure 6.2 shows simulation profiles obtained using the reduced pressure method, again with $\theta_{eq} = \theta_i = \pi/2$. The profiles at equilibrium are shown for $h^* = 0.03$ in red , $h^* = 0.015$ in green, and $h^* = 0.0075$ in blue. The initial condition for $h^* = 0.015$ is shown by the black dotted line, showing the profile of a drop with

Table 6.2 Comparison of the Influence of h^* on θ_{num}, Between the Reduced Pressure Method (First Column) and Body Force Method (Second Column) Described in Chapter 5. The Second and Third Columns are θ_{num} Calculated for the Respective Simulations. The Two Methods Similarly Approach the Value of $\theta_{eq} = \pi/2$.

h^*	R–P	Body Force
0.03	1.36	1.37
0.015	1.45	1.47
0.0075	1.49	1.53

contact angle θ_{eq}. The smooth transition from the drop profile to the equilibrium film is clearly visible; as h^* is reduced, the equilibrium profiles approach those of a drop with contact angle θ_{eq}.

Table 6.2 shows the measured values of θ_{num} as h^* is varied for the B–F and R–P methods; as in Tab. 6.1, $\theta_{eq} = \theta_i = \pi/2$. While the values differ slightly between the two methods, as h^* is reduced, θ_{num} becomes closer to θ_{eq}. The difference in θ_{num} between R–P and B–F methods is expected to be due to the fact that the R–P simulations were run with an adaptive mesh, while the B–F simulations were run with a uniform mesh.

The reduced pressure method behaves comparably to the body force method in 2D in its ability to model the contact angle. However, it comes with the potential for dramatically improved performance, due to fact that the layer of fluid near the substrate does not necessarily need to be highly resolved. For example, for the drops simulated in Tab. 6.1, with the timestep fixed at 10^{-5}, at $\Delta = 1/2^6$ the reduced pressure method takes approximately 14% as much CPU time as the body force method; at $\Delta = 1/2^7$, the reduced pressure method has approximately 5% the runtime. This is because, for each timestep, the number of computations each method incurs is $O(N)$, where N is the number of cells. However, the adaptive mesh

illustrated in Figure 6.1 involves approximately $O(1/\Delta)$ cells, while a uniform mesh has $O(1/\Delta^2)$ cells. Simple adaptive meshes were used in Chapter 5, improving the performance of the body force method, however higher resolution is still required at a layer of nonzero thickness near the substrate, and a similar complexity can still be expected as with uniform meshes. The complexity difference is similar in 3D, where the R–P method should scale as $O(1/\Delta^2)$ and a B–F method should scale as $O(1/\Delta^3)$.

The $O(1/\Delta^3)$ complexity of the B–F methods renders them impractical in terms of the requisite computational time; for this reason, we do not consider a comparison of the R–P and B–F methods in 3D. The reduced complexity of the R–P method permits the study of more complicated phenomena. In the following sections, we will study the breakup of films in two and three dimension.

6.2.2 Film Instability

As discussed in Section 6.1, the liquid/solid interaction can lead to the spontaneous rupture of thin liquid films. We study this breakup by means of the LSA of Eq. (6.7). Equation (6.7) itself is only expected to describe the flow in the regime satisfying the assumptions outlined in Section 6.1, and the LSA only applies to the growth rate of unstable, infinitesimally small modes for early times. In this section, we compare the predictions of the LSA analysis to simulations of unstable films with low inertia during the earliest stages of breakup, which is a regime where the LSA is expected to apply. We quantify the boundaries of the regime where the LSA applies, and its implication for using the LSA to describe these flows.

We vary h_0 and θ_{eq} in order to investigate the effect on the instability. It is important to note that Eq. (6.8) is valid even for large θ_{eq}, since θ_{eq} only enters into Eq. (6.7) through the disjoining pressure; during the early stages of instability we consider in this section, large values of θ_{eq} do not lead to large interfacial slopes, and the LSA still applies. We set $Oh = 0.45$, which leads to $Re \approx 0.23$ and $Ca \approx 0.09$,

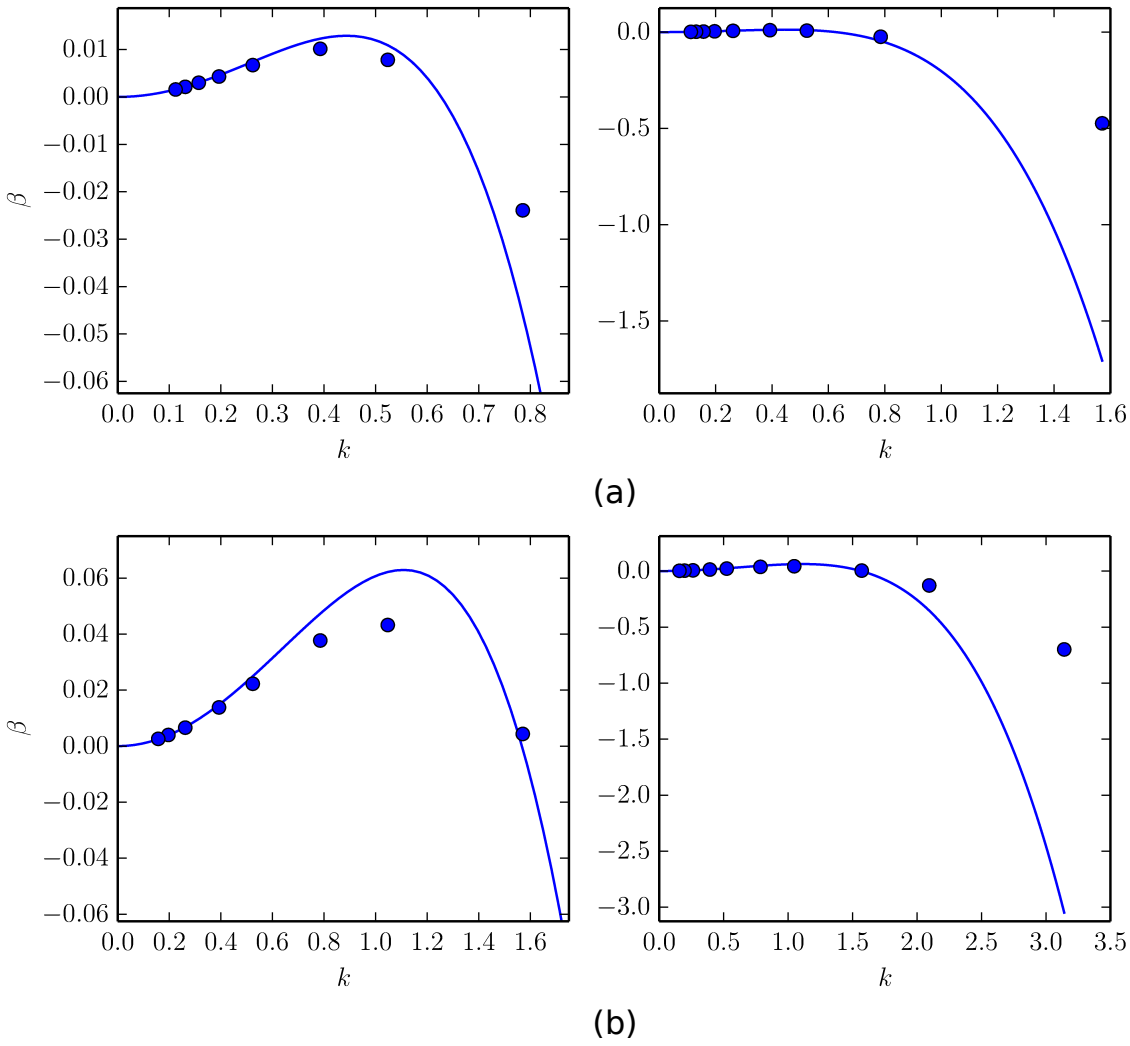

Figure 6.3 Comparison between the dispersion curve predicted by LSA of the long–wave model (blue solid curve) and the growth rate observed in R–P simulations (symbols), with $\theta_{eq} = \pi/2$, for (a) $h_0 = 0.25$, and (b) $h_0 = 0.125$. The plots on the right are the same as the left plots, except the range is larger. Significant difference is apparent except when k is small, and the disagreement increases with k. Reduction in h_0 does not reduce this difference.

so that the simulations are of flows with negligible inertia. All simulations in this section are 2D, and the initial region occupied by the liquid phase (i.e., $T = 1$) is between $y = 0$ and $h = h(t = 0, x) = h_0\epsilon\cos(kx)$, where $\epsilon = 0.02$. For all simulations in this section, we set $h^* = 0.12$.

In 2D, the dispersion relation (Eq. 6.8) is

$$\beta = \frac{h_0^3 k^2 \left(k_c^2 - k^2\right)}{3} \tag{6.13}$$

We estimate the growth rate of a perturbation in the linear regime by first finding the interval over which the growth is exponential. We then fit exponential growth curves to the time dependent minimum and maximum of the interface profile, and the approximate growth rate is taken to be the average of the growth rate of these two curves. For early times, the interface of the film is a single-valued film thickness, and we represent the piecewise linear reconstructed interface from the Volume of Fluid method by $y = h(t, x)$; this function is sampled at a discrete set of times and points in space. We define the quantities $\eta_{min}(t) = \ln(\min_x h(t, x))$, and $\eta_{max}(t) = \ln(\max_x h(t, x))$. We then calculate an interval $I_{fit} = (t_0, t_1)$ such that each of these functions is approximately linear in t over I_{fit}. Finally, we calculate for each function $\eta_{min,max}(t)$ a least squares fit

$$a_{min,max} t + b_{min,max},$$

and set the approximate growth rate as

$$\beta_{num} = \frac{a_{min} + a_{max}}{2}. \tag{6.14}$$

Figure 6.3 compares two different initial thicknesses, $h_0 = 1$ (Figure 6.3 (a)) and $h_0 = 0.5$ (Figure 6.3 (b)), and the predicted (solid curve) growth rate with the measured (blue circles) growth rates for each thickness. When the wavenumber k is small, the LSA and the measured growth rate are very close; however for larger k, there is a significant difference. This difference appears for both values of h_0. We conjecture that the differences is due to the fact that the long–wave assumption no longer holds for larger k; Eq. (6.7) requires that the characteristic length scale x_c and the characteristic film thickness h_c obey $h_c/x_c \ll 1$. In Figure 6.3 (b), however, the

relevant film thickness is $h_0 = 0.125$, and the relevant length scale is $2\pi/k_{max} = \lambda_{max}$. The "small parameter" then is h_0/λ_{max}, which in this case is $O(0.1)$, which may not be sufficiently small.

The results of Figure 6.3 suggest an important conclusion with regards to the validity of the LSA: a reduction in the film thickness, all other things being equal, can not transition the system to a long–wave regime, because the relevant length scales become shorter as well. The ratio of the relevant film thickness, h_c, and length scale, x_c is given by:

$$\frac{h_c}{x_c} = \frac{h_0}{\lambda_{max}} = \frac{1}{2\pi}\sqrt{-Kh_0\left[m\left(\frac{h^*}{h_0}\right)^m - n\left(\frac{h^*}{h_0}\right)^n\right]} \tag{6.15}$$

This expression is decreasing as h_0 is increased when

$$h_0 > h^*\left[\frac{m(m-1)}{n(n-1)}\right]^{m-n}$$

In particular, this means that reducing h_0 actually implies that long–wave approximation is less accurate, except when h_0 is nearly as small as h^*.

Equation (6.15) implies that a reduction in θ_{eq} can improve agreement with long–wave theory. This is due to the fact that the parameter K is proportional to $(1 - \cos\theta_{eq})$, so as $\theta_{eq} \to 0$ so does h_0/λ_{max}. We compare simulation results in the linear regime with the LSA as θ_{eq} is varied in Figure 6.4. The solid curves show the prediction of the LSA, while the blue circles show values from simulations. For each θ_{eq}, we approximate the wavenumber of maximum growth, which is shown by the vertical solid line in each figure. The vertical dash-dotted line shows k_{max} from Eq. (6.10). As predicted by Eq. (6.15), a reduction in θ_{eq} improves agreement with the LSA considerably. For larger θ_{eq}, the LSA predicts a faster growth rate, and predicts a larger value of λ_{max}.

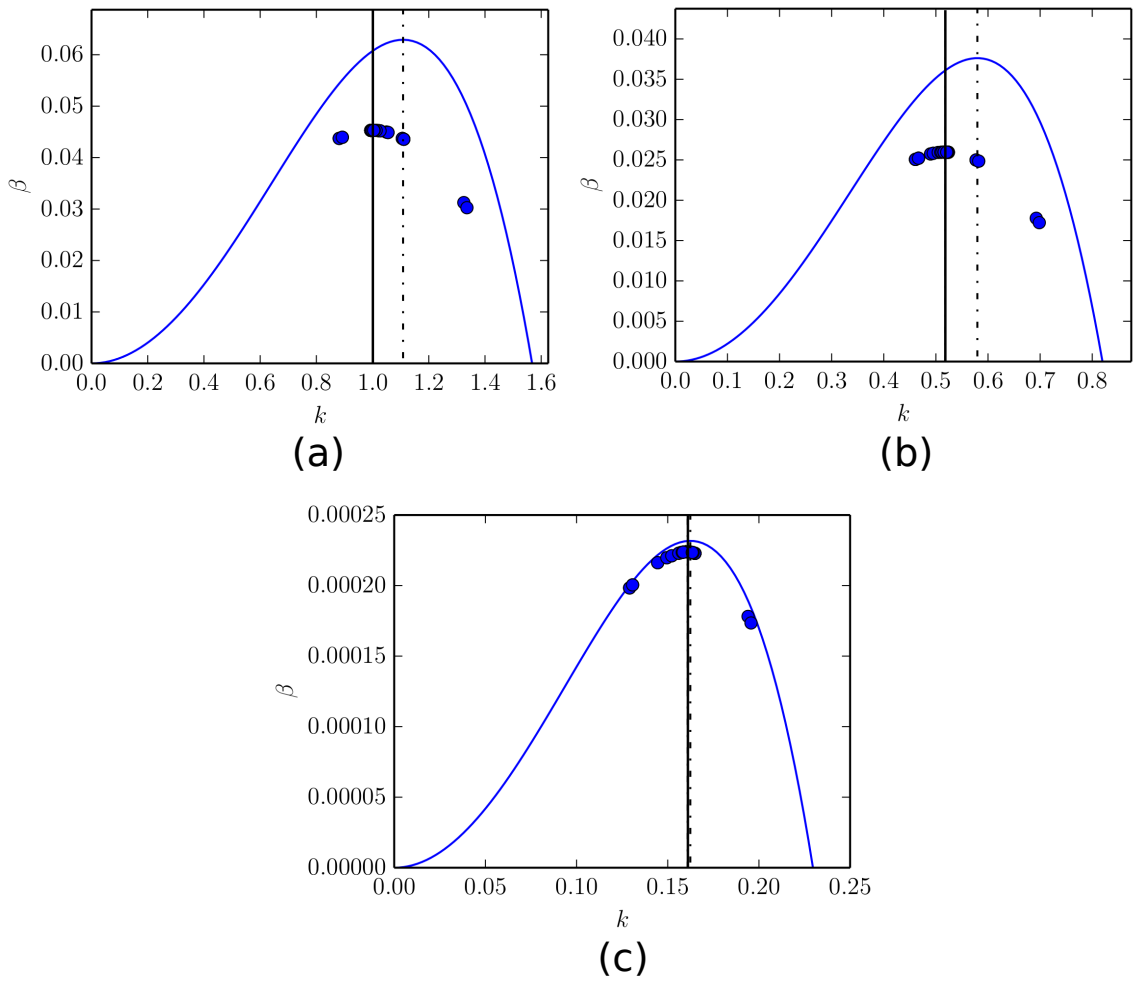

Figure 6.4 Comparison between the dispersion curve predicted by LSA (blue solid curve), and the growth rate observed in simulations (symbols) for θ_{eq}, for $h_0 = 1$, and (a) $\theta_{eq} = 3\pi/4$, (b) $\theta_{eq} = \pi/2$, and (c) $\theta_{eq} = \pi/6$. The wavenumber of maximum growth is approximated using a bisection method, and is shown by the solid vertical lines; the vertical dash dotted lines show the value of k_{max} from Eq. (6.10). Smaller θ_{eq} leads to significantly improved agreement between LSA and simulations.

6.3 Nonlinear Evolution: Film Breakup

In Section 6.2.2, we compared the predictions of the LSA with numerical simulations of the full equations in the linear regime. In this section, we consider the process of film rupture, and subsequent evolution into drops. Our goal is to describe the length scales of the breakup, and their relationship with the value of λ_{max} predicted by the LSA. Moreover, we extend our study to 3D, and find differences in the breakup process with respect to 2D simulations. We find that while the initial phase of breakup can

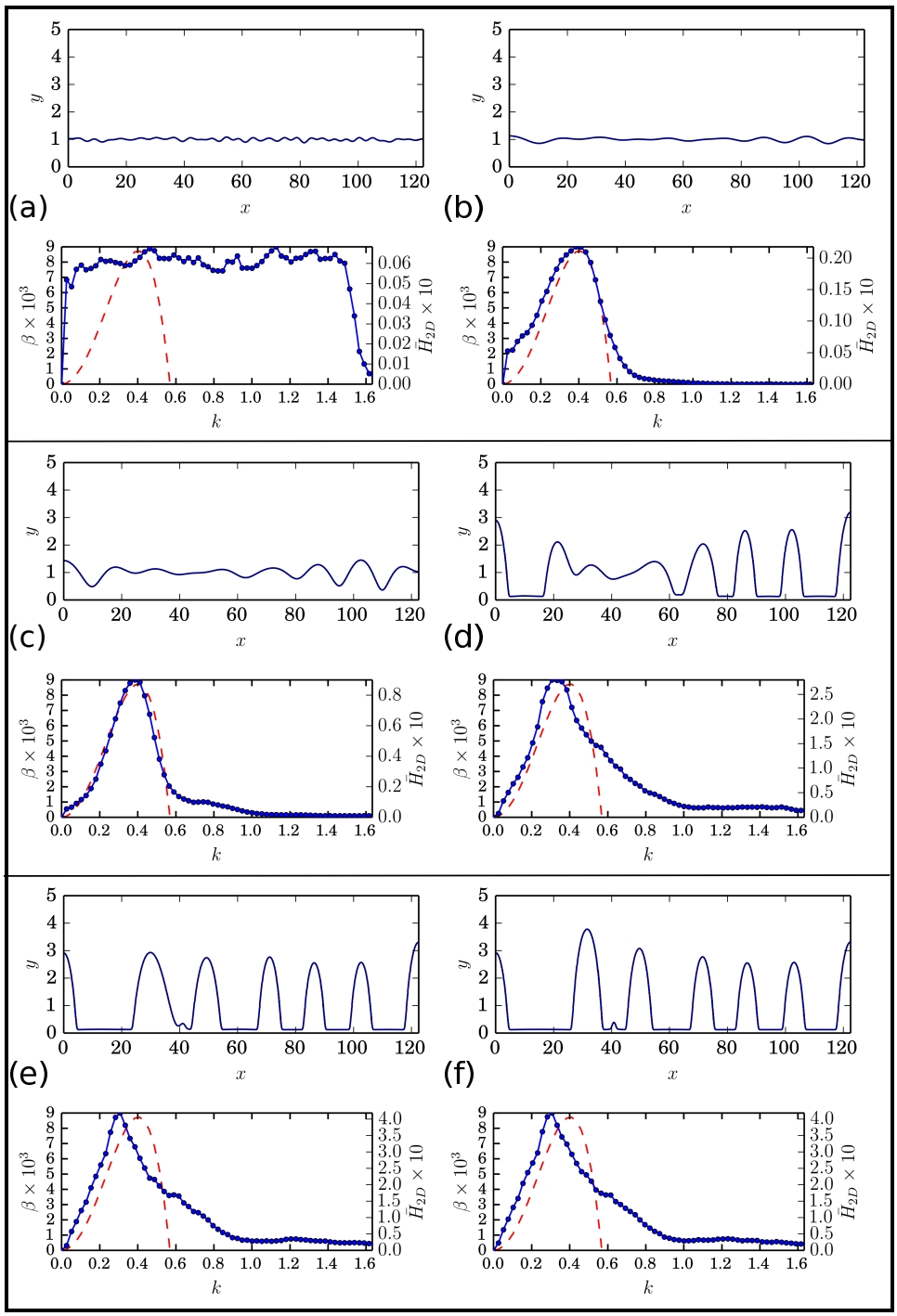

Figure 6.5 Time evolution of a representative simulation of film breakup in 2D for t = (a) 0, (b) 179, (c) 357, (d) 536, (e) 715, (f) 882. The parameters are $h_0 = 1$, $Oh = 0.487$, and $\theta_{eq} = 0.439\pi$; the solid blue curve shows the fluid interface. The associated Fourier spectrum, averaged over 20 instances, is shown below each image.

be understood by the LSA, the end state, consisting of drops, is characterized by a length scale different from that predicted by the LSA, and is influenced by the contact angle, Ohnesorge number, and whether we consider 2D or 3D films.

The inspiration for our study is derived again from work on self assembly of nanoparticles via the dewetting of a thin film. The particular geometry we initially study is a flat metallic film liquefied by laser pulses, as considered in [40]. A film such as this ruptures due to the liquid/solid interaction; consequently, the spacing of the resulting drops is dictated by the length scales associated with this instability mechanism. The simplest possibility is that the mode with the largest growth rate in the linear regime, that is the mode with wavelength λ_{max}, would dominate the breakup, and consequently that the end drops would be spaced with a center to center spacing roughly equal to λ_{max}. Direct numerical simulations reveal that the center to center drop spacing is generally larger than λ_{max}.

In order to choose a reference parameter set, we simulate copper films, studied experimentally and theoretically in [40]. The viscosity, density, and surface tension are taken to be the values of liquid copper at its melting point. We set L to be equal to the reference film thickness, taken to be 8 nm. The Ohnesorge number is $Oh = 0.487$. The simulations that we present in this section are for a film of thickness $h_0 = 1$; we also simulated films with $h_0 = 0.5$, and these behaved similarly. The equilibrium film thickness is set to be $h^* = 0.1225$, and $\theta_{eq} = 79^\circ \approx 0.439\pi$. Note for these parameters, the Reynolds and Capillary numbers defined in Eq. (6.12) are, respectively, $Re \approx 0.04$, $Ca \approx 0.009$, and $\lambda_{max} \approx 15.6$, and $\lambda_c \approx 11.0$.

We begin by studying the 2D film. The computational domain is $(x, y) \in (0, 122.5) \times (0, 43.125)$ (the exact value of the domain size is due to the fact that the parameters used to run the simulation are scaled differently from the dimensionless numbers described here, and the domain height and width are integers in the simulation). The initial film thickness is $h_0 + \zeta$, where ζ is a perturbation of the

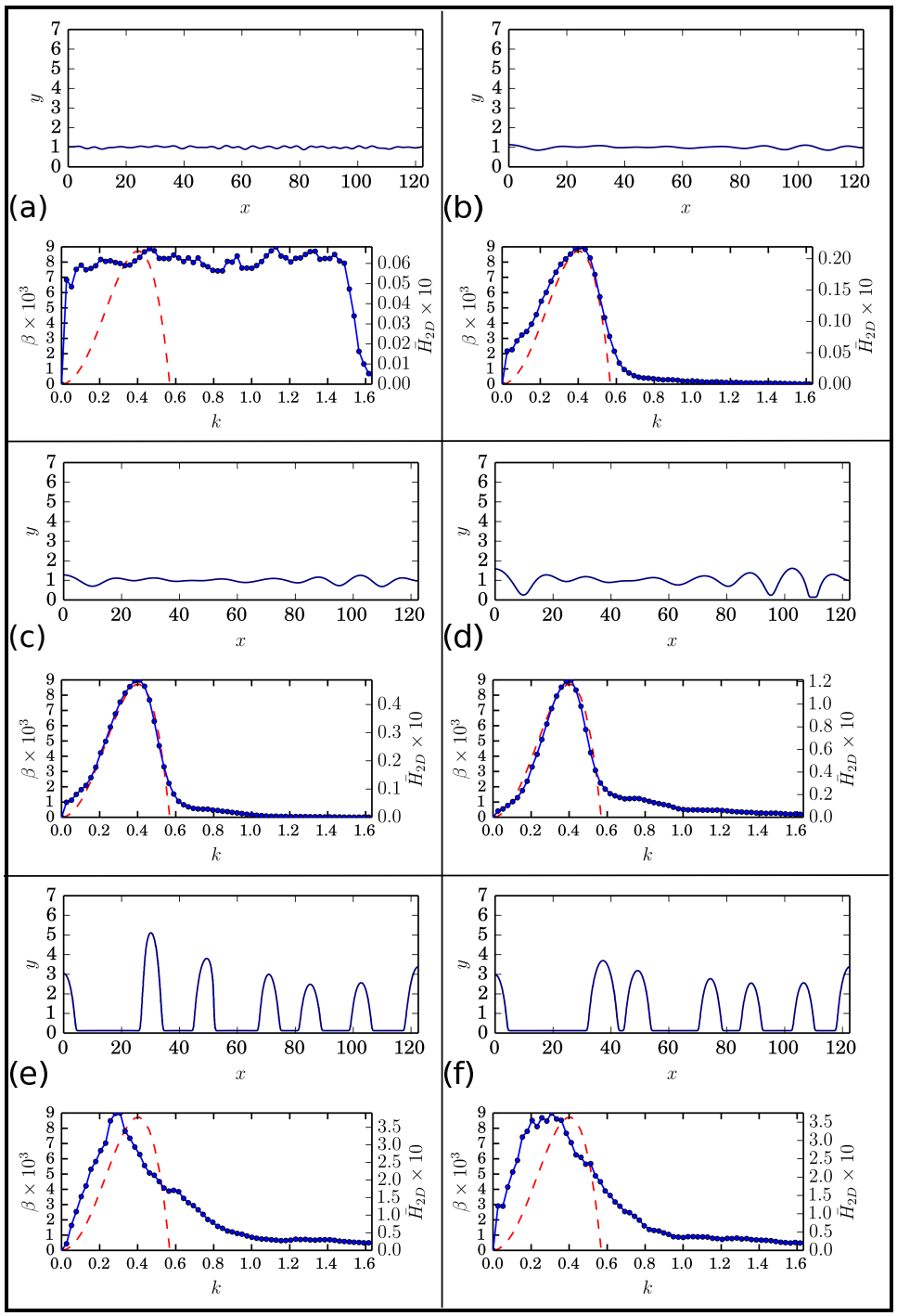

Figure 6.6 Temporal evolution of a representative simulation of film breakup in 2D for $t =$ (a) 0, (b) 357, (c) 536, (d) 715, (e) 1429, (f) 2858. The parameters are $h_0 = 1$, $Oh = 0.0487$, and $\theta_{eq} = 0.439\pi$, and $h^* = 0.1225$; the solid blue curve shows the fluid interface. The associated Fourier spectrum, averaged over 20 instances, is shown below each image.

form

$$\zeta(x) = \sum_{i=1}^{60} \epsilon_i \cos\left(\frac{2\pi x}{\lambda_i}\right) \tag{6.16}$$

where $\lambda_i = 245/i$, and ϵ_i is a random perturbation amplitude, uniformly distributed in the range ± 0.0125. The wavelength $\lambda_1 = 245$ is twice the width of the computational domain, and consequently the longest wavelength which can be resolved. We simulate the breakup of this film with $N_s = 20$ sets of ϵ_i. For each simulation (numbered j), a discrete height profile is produced, $\hat{h}_j(t, x)$. We then compute the discrete Fourier transform (DFT) of each height profile, $\hat{H}_j(t, k)$. Finally, we compute the average of these as

$$\bar{H}_{2D}(t, k) = \frac{1}{N_s} \sum_{j=1}^{N_s} \hat{h}_j(t, k) \tag{6.17}$$

In Figure 6.5, we plot the time evolution of the profile $\hat{h}_0(t, x)$ (the upper image in each of Figure 6.5(a)-(f)), and the corresponding plot of $\bar{H}_{2D}(t, k)$ along with the dispersion curve from the LSA (bottom image in each of Figure 6.5(a)-(f), shown smoothed with a 5 point average to smooth the curve). We see that as the initial perturbations begin to grow, the $\bar{H}_{2D}(t, x)$ is of similar shape to the dispersion curve (Figure 6.5(a) - (c)). However, as the holes begin to form in the film, and consequently drops begin to form, the peak in $\bar{H}_{2D}(t, k)$ shifts towards smaller values of k, so that the final distribution of drops is characterized by a larger length scale than λ_{max} predicted by the LSA (Figure 6.5(d) - (f)).

Next we consider different values of Oh. For $Oh = 4.87$, no significant difference was observed. The results obtained with smaller values of Oh show several significant differences. Figure 6.6 shows profiles and associated averaged Fourier spectra for a film with $Oh = 0.0487$. In the simulations that use smaller Oh, the film takes an order of magnitude longer to break up as compared to films with larger Oh. Otherwise, prior to breakup, the evolution of the Fourier spectrum is quite similar. The long

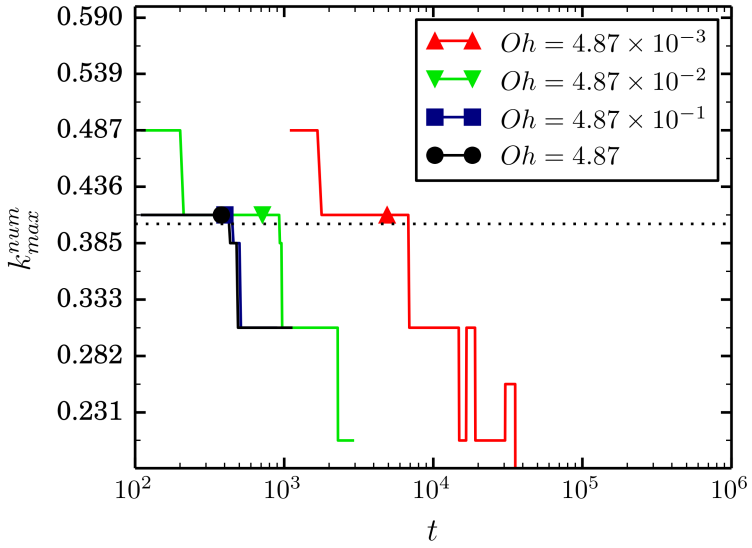

Figure 6.7 Comparison of k_{max}^{num} as a function of time for films of varying Oh. Symbols show the approximate breakup times for each parameter set, and the solid dashed line shows k_{max} predicted by the LSA. Note that $Oh = 4.87$ and $Oh = 0.487$ are visually nearly indistinguishable on this plot. The ticks on the y-axis are for wavenumbers which can be resolved on the finite domain. $h_0 = 1$, $\theta_{eq} = 0.439\pi$, $h^* = 0.1225$.

term evolution of the Fourier spectrum shows a flatter peak when compared with the larger Oh simulations, indicating that the preference for a specific wavenumber is weaker in the late stages of evolution.

In order to study the effect of Oh on the evolution of the film, we define $k_{max}^{num}(t)$ to be the value of k for which $\bar{H}_{2D}(t)$ attains its maximum. Figure 6.7 plots k_{max}^{num} for various Oh as a function of time; note that due to the finite domain size, k_{max}^{num} only takes discrete values, leading to the staircase appearance of these plots. The symbols on each curve indicate the approximate time at which the film ruptures, and the dashed line shows the value of k_{max} from the LSA. The overall behavior is similar for all curves: k_{max}^{num} quickly takes a value as close to the k_{max} as can be resolved on a finite domain; k_{max}^{num} then stays at this value until the film breaks up. Afterwards, it becomes smaller, indicating that the length scale of the final drop distribution is larger than k_{max}. For $Oh = 4.87$ and $Oh = 0.487$, the behavior is nearly indistinguishable,

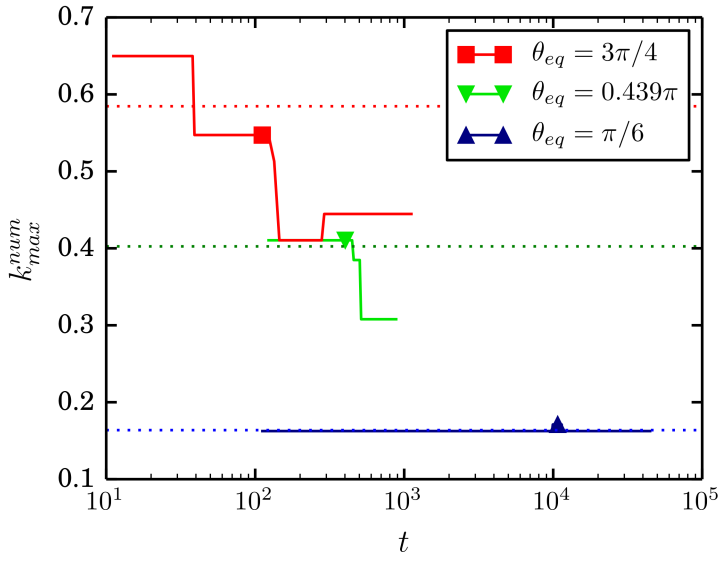

Figure 6.8 Plot of k_{max}^{num} for varying θ_{eq}. The green curve corresponds to $Oh = 0.487$ in Figure 6.7. The symbols show the approximate time of film rupture. Each dashed line shows k_{max} from the LSA for the curve of the same color. $h_0 = 1$, $h^* = 0.1225$.

indicating that these films are in the large Oh limit. The most important effect of Oh is that smaller Oh significantly increases the time it takes for the film to rupture. For $Oh = 4.87 \times 10^{-3}$, the time of breakup is an order of magnitude larger than for $Oh = 4.87$. The LSA does not capture this behavior, and instead predicts that the breakup time is approximately 500 irrespective of Oh; this is consistent with the large Oh simulations, which are insensitive to Oh.

Next, we investigate the effect of the contact angle on the rupture. We ran two additional simulation sets, both with $Oh = 0.487$.

1. $\theta_{eq} = \pi/6$, $(x, y) \in (0, 367.5) \times (0, 43.125)$.

2. $\theta_{eq} = 3\pi/4$, $(x, y) \in (0, 91.875) \times (0, 43.125)$.

These computational domain widths are approximately the same multiple of the respective λ_{max} of each θ_{eq} as the simulations described above. For each set, the form of the perturbation is the same as in Eq. (6.16), except that for $\theta_{eq} = \pi/6$ we set $\lambda_i = 735/i$, and for $\theta_{eq} = 3\pi/4$, $\lambda_i = 183.75/i$. We plot k_{max}^{num} for these two contact

angles, as well as for $\theta_{eq} = 79/180\pi \approx 0.439\pi$ in Figure 6.8. For each curve, the symbol of the same color indicates the breakup time, and the dashed line of the same color shows k_{max} from the LSA; note that the breakup times predicted by the LSA are $\approx$ 18000, 500, and 110, for $\theta_{eq} = \pi/6$, 0.439π, and $3\pi/4$, respectively, which is roughly in line with the simulated breakup time for all cases. When $\theta_{eq} = 3\pi/4$, the behavior is similar to $\theta_{eq} = 79/180\pi$. However, the evolution of $\theta_{eq} = \pi/6$ is simpler than for larger θ: almost immediately, k_{max}^{num} relaxes to near k_{max}, and remains at approximately the same value for the considered simulation times. This indicates that for small contact angles, the length scale associated with k_{max} dominates in both the linear and nonlinear regimes of breakup, at least within the resolution of our simulations.

The difference in evolution between the small θ_{eq} and the larger θ_{eq} results can be understood as follows. We approximate the profile of a rupturing film of unit initial thickness, perturbed by a mode of wavelength λ_{max}, by

$$h(x) = 1 + A(t)\cos\left(\frac{2\pi x}{\lambda_{max}}\right)$$

where $A(t)$ is the time dependent amplitude. At the time of breakup, $A(t) \approx 1$. We approximate the instantaneous contact angle of the rupturing film by considering the slope at the point of inflection, given by

$$\tan\theta_r = \frac{2\pi}{\lambda_{max}}$$

Substituting the expression for λ_{max}, we obtain

$$\tan\theta_r = B\sqrt{1-\cos(\theta_{eq})}$$

where B is a positive constant:

$$B = \sqrt{-\frac{(mh^{*m} - nh^{*n})}{2\sqrt{2}h^*}}$$

Consider the expression

$$|\theta_r - \theta_{eq}| = |\tan^{-1}\left(B\sqrt{1-\cos\theta_{eq}}\right) - \theta_{eq}|$$

This expression is an increasing function of θ_{eq} for $\theta_{eq} \in (0, \pi/2)$. This suggests that when films with larger θ_{eq} rupture, the contact angles near the initial holes are further from θ_{eq} than for the films involving smaller θ_{eq}. This difference in contact angles leads to a stronger tendency to retract from the initial hole for films with larger θ_{eq}, and, correspondingly, the liquid between two holes (which we call a filament) will tend to collapse. We conjecture that velocity field due to the collapse of the filament interferes with any further rupture from the liquid/solid interaction.

Next, we consider film breakup in 3D. We have not previously considered 3D simulations, owing to the large computational cost associated with the B–F method. The setup is identical, except that the domain consists of $(x, y, z) \in (0, 61.25) \times (0, 31.25) \times (0, 61.25)$. The initial condition is a perturbed film of the form $y = h_0 + \zeta$ where ζ is a perturbation of the form

$$\zeta(x, y) = \sum_{i=1}^{30}\sum_{j=1}^{30} \epsilon_{ij} \cos\left(\frac{2\pi x}{\lambda_i}\right) \cos\left(\frac{2\pi z}{\lambda_j}\right) \tag{6.18}$$

where $\lambda_i = 122.5/i$, and ϵ_{ij} are random perturbation amplitudes, uniformly distributed in the range ± 0.0125. Due to computational constraints, we simulate the film for $N_s = 10$ sets of ϵ_{ij}. As before, we produce a height profile for each simulation, $\hat{h}_j(t, x, z)$, and compute its DFT, $\hat{H}_j(t, k, l)$. We then compute the following average

$$\bar{H}_{3D}(t, k) = \frac{1}{N_s}\sum_{j=1}^{N_s} \frac{1}{2}\left(\hat{h}_j(t, k, 0) + \hat{h}_j(t, 0, k)\right) \tag{6.19}$$

The summand in Eq. (6.19) represents the average of the DFTs of simulation j along the x and z axes. Equation (6.8) is symmetric in k and l, so the DFT along $k = 0$ and $l = 0$ yields equivalent information about the evolution of the profile.

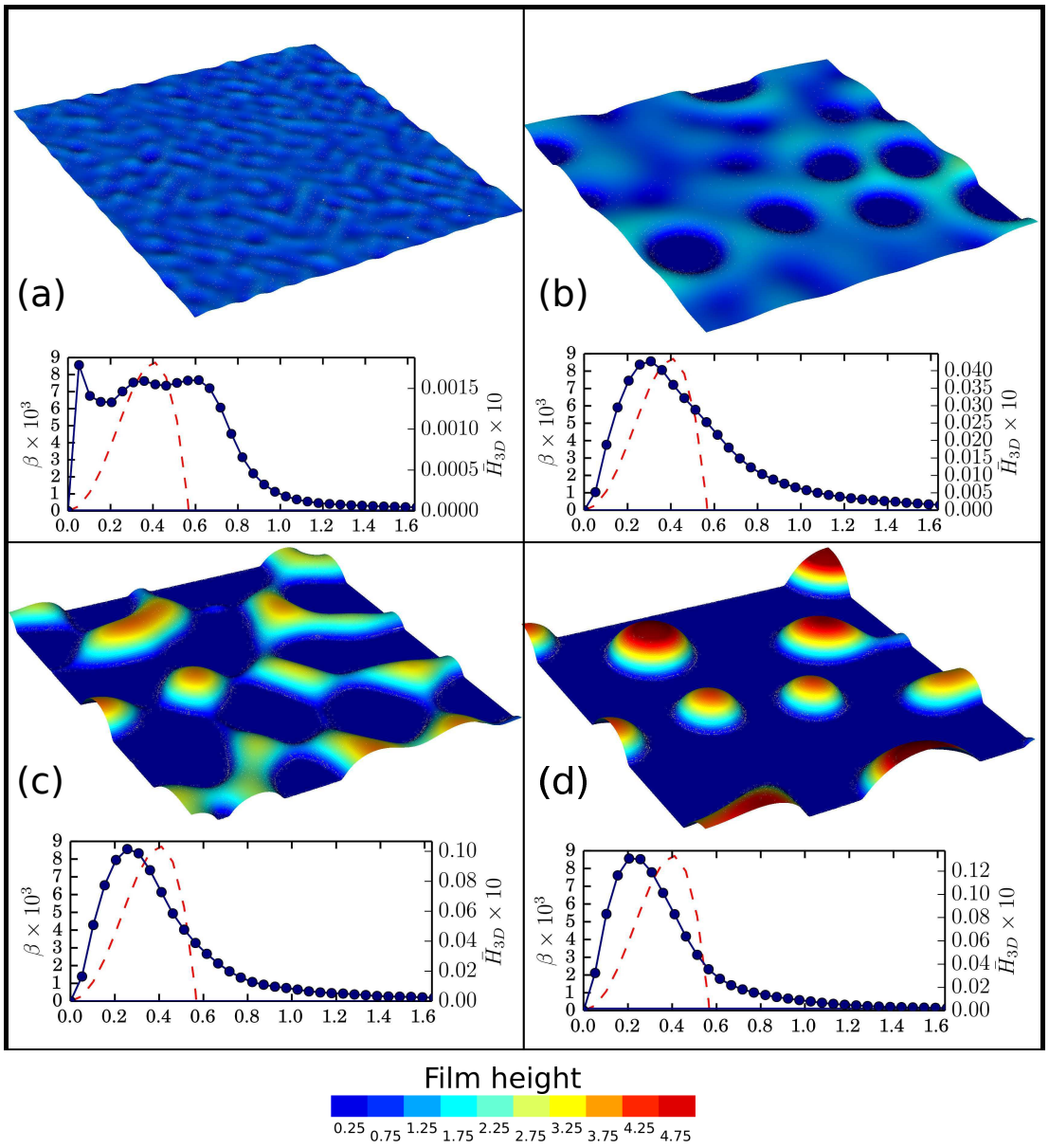

Figure 6.9 Time evolution a representative simulation of film breakup in 3D for t = (a) 0, (b) 335, (c) 558, (d) 781. The parameters are $Oh = 0.487$, $h_0 = 1.0$, and $\theta_{eq} = 0.439\pi$, $h^* = 0.1225$. The color shows the logarithm of the height of the interface above the substrate. The associated Fourier spectrum is shown below each image; these data are averaged over 10 instances, and smoothed with a 5 point running average.

Figure 6.9 plots the time evolution of $\hat{h}_0(t, x, z)$ (top image in each part of the figure), and $\bar{H}_{3D}$ along with the dispersion curve predicted by Eq. (6.8) (bottom images). The plots of $\bar{H}_{3D}$ have been smoothed by a five point average. A similar

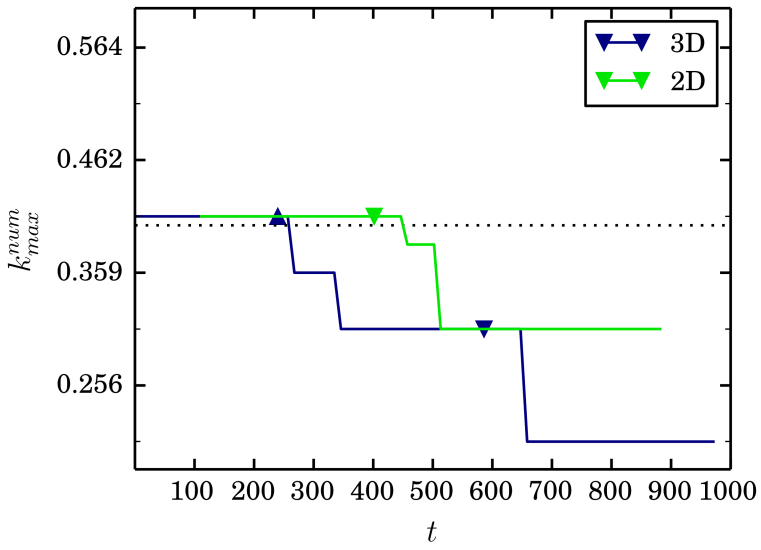

Figure 6.10 Comparison of k_{max}^{num} as a function of time for 3D films (blue) and 2D films (green). The green inverted triangle shows the approximate breakup time of the 2D simulation. The blue triangle shows the approximate time at which the first holes form in the 3D film; the inverted blue triangle shows the approximate time that drops begin to form. The solid dashed line shows k_{max} predicted by the LSA. $h_0 = 1$, $h^* = 0.1225$.

trend is observed as in Figure 6.5: the spectrum takes on a similar profile to the dispersion curve from the LSA, and as breakup proceeds, its peak, k_{max}^{num}, shifts towards smaller wavenumbers. Note that the peak in the spectrum is smoother for 3D (Figure 6.9) compared to 2D (Figure 6.5), suggesting that in 3D larger variability of the drops spacing may be expected. However, more detailed analysis is needed to confirm this finding, in particular since DFT in 3D contains fewer points, so that the averaging procedure is not identical between 2D and 3D.

To contrast the evolution of the 3D film with the 2D one, in Figure 6.10 we plot $k_{max}^{num}(t)$, computed for both with the same parameters ($Oh = 4.87$). We mark two important events for the 3D simulations in Figure 6.10: first, the appearance of holes in the film (marked by a blue triangle), and second, the formation of drops (marked by a blue inverted triangle). As in Figure 6.7, we mark time of breakup of the 2D film with a triangle. For both 2D and 3D, k_{max}^{num} is close to k_{max} until the film ruptures,

after which k_{max}^{num} relaxes to a smaller values. However, once drops begin to form for 3D simulations, k_{max}^{num} relaxes to an even smaller value, characterizing the distribution of drops at equilibrium.

To summarize, the DFT of the nonlinear film breakup shows that the dominant length scales deviate from λ_{max} from the LSA. The degree of deviation depends on θ_{eq}, and whether the film is 2D or 3D; additionally, the time it takes for the film to rupture depends strongly on Oh. For 2D simulations with small θ_{eq}, the DFT has a peak at or close to k_{max} for the entirety of the film evolution. For larger θ_{eq}, the evolution of the DFT shows two distinct phases: prior to breakup, when the peak in the DFT is at k_{max}, and after breakup, when the peak shifts to smaller wavenumbers. For 3D simulations, the evolution of the DFT shows three distinct phases, each associated with a shift towards smaller wavenumbers: prior to breakup, after holes begin to form, and after drops begin to form. A decrease in Oh is primarily associated with a dramatic increase in the time it takes for the film to rupture.

6.4 Conclusions

In this chapter, we demonstrate a computationally efficient method for including fluid/solid interactions into direct numerical simulations. This method is found to perform as well as the body force formulation of Chapter 5, while requiring only a fraction of the computational cost. The advantages of the present method are specifically demonstrated by comparing contact angles in 2D, where both methods perform similarly in terms of convergence in mesh, and in terms of the behavior of θ_{num} as h^* is reduced. The computational time required however is dramatically simpler in the presented method.

Due to the improvement in computational performance, it is now possible to study the instability of films due to fluid/solid interaction using direct numerical simulation. We compare the results with the LSA of the long–wave equations, and find that when θ_{eq} is larger, there is a significant difference with the predictions of the LSA. We also demonstrate that a reduction in the film thickness does not reduce the difference with the LSA, as the horizontal length scale decreases with the vertical length scale.

Finally, we study breakup of a film in both 2D and 3D. We describe the evolution of the length scales by computing the discrete Fourier transform of the fluid profile. 2D films are characterized by a two stage evolution, and 3D films by a three stage evolution; for both cases, the initial phase exhibits a DFT with a peak, k_{max}^{num}, near k_{max} from the LSA, and each successive stage is associated with a decrease in k_{max}^{num}, and correspondingly, an increase in the characteristic length scales.

The speed and simplicity of implementation of the method presented in this chapter opens up the possibility of studying a variety of problems that have either not been studied extensively in direct numerical simulations, or were impractical to simulate previously. The method allows for the simulation of arbitrary contact angles (including those greater than $\pi/2$), and film breakup, with full inertial effects for the

first time. While we have studied the influence of varying θ_{eq} and Oh in 2D films, we leave an exhaustive parameter of 3D films for a future work.

CHAPTER 7

CONCLUSION

In this thesis we have studied the use of Volume of Fluid based, direct numerical simulations of contact angle dynamics and dewetting problems. We have examined the differences between the classical long–wave method and these direct numerical simulations, and have quantified the disagreement that these two methods show at larger contact angles.

A novel form of breakup was studied, which resulted from an initially rectangular-wave liquid metallic shape on a substrate. This rectangular-wave was found to result in drop spacings which are of unprecedentedly close spacing. Moreover, several unique end states were observed as this geometry relaxed, including combinations of drops and filaments; in practical applications these liquid metallic configurations will solidify into patterns of nanoparticles and nanowires. Experimental investigation into reproducing these configurations is an ongoing project.

We developed a method that, for the first time, permits the inclusion of the nanoscale interaction between liquid films and a solid substrate in Volume of Fluid based simulations. This method leads to simulation of the underlying physics in such a way that contact angles of arbitrary size arise naturally. We studied the convergence properties of this method thoroughly, and demonstrated that it can be used to simulate systems with large contact angles. Furthermore, we described an improvement to this method that possesses comparable accuracy at greatly reduced computational cost. This improvement in performance permitted the practical study of diverse phenomena in 2D and 3D. We demonstrated the first direction numerical simulations of film breakup due to the liquid/solid interaction with inertial effects and

large contact angles. The limitations and applicability of long–wave linear stability analysis were studied, and we described the effect of contact angle and inertia on the process of film rupture.

While the long–wave model has shown considerable versatility in the study of dewetting nanometallic films, our results have reinforced the need to use direct numerical simulation, as these systems have large contact angles and potentially significant inertia. At the same time, long–wave models have for a long time included the interaction between the fluids and the solid substrate which has been essential for studying certain kinds of film dewetting. By developing a new numerical method for Volume of Fluid simulations with fluid/solid interactions, we can now simulate these film breakups. This is an important step towards developing a more complete continuum based theory of nanofilm breakup and directed nanoparticle assembly.

The liquid/solid interaction methods of Chapters 5 and 6 more generally permit the study of a great variety of new problems. While we have discussed the influence of inertia and contact angle in a limited parameter regime, an exhaustive study of these effects for unstable thin films has not been possible previously. An important future direction of this research is to develop a more complete theory characterizing the influence these parameters in the temporal and spatial scales characterizing thin film dewetting.

In the future, direct numerical simulation can be extended further to simulate nanometallic film breakup in greater detail. A core feature of the model of Chapter 4 is that we treated the film as constant in temperature. In experiments such as [72], however, multiple laser pulses are used, resulting in the nanostructure liquefying and resolidifying multiple times, with the temperature varying significantly while it is in the liquid phase. The viscosity during the liquid evolution, in particular, may vary by a factor or two or more, leading to increased inertial effects. The temperature may furthermore vary spatially, as discussed in [90]; such temperature

variation leads to a corresponding spatially varying surface tension, and consequently, to thermocapillarity effects which may promote breakup or dampen instabilities, depending on the nature of the temperature profile. Finally, the solidification itself may influence the breakup, by halting the evolution and consequently canceling out some of the inertial effects that we found to be significant in Chapter 4.

BIBLIOGRAPHY

[1] S. Afkhami and M. Bussmann. Height functions for applying contact angles to 2D VOF simulations. *Int. J. Numer. Meth. Fluids*, 57:453, 2008.

[2] S. Afkhami and M. Bussmann. Height functions for applying contact angles to 3D VOF simulations. *Int. J. Numer. Meth. Fluids*, 61:827, 2009.

[3] S. Afkhami and L. Kondic. Numerical simulation of ejected molten metal nanoparticles liquified by laser irradiation: Interplay of geometry and dewetting. *Phys. Rev. Lett.*, 111:034501, 2013.

[4] S. Afkhami, S. Zaleski, and M. Bussmann. A mesh-dependent model for applying dynamic contact angles to VOF simulations. *J. Comput. Phys.*, 228:5370, 2009.

[5] E. Aulisa, S. Manservisi, R. Scardovelli, and S. Zaleski. Interface reconstruction with least-square fit and split Eulerian-Lagrangian advection. *J. Comput. Phys.*, 225:2301, 2007.

[6] S. Baderi. Colloquium: Opportunities in Nanomagnetism. *Rev. Mod. Phys.*, 78:1, 2006.

[7] T. Baer, R. Cairncross, P. Schunk, R. Rao, and P. Sackinger. A finite element method for free surface flows of incompressible fluids in three dimensions. part ii. dynamic wetting lines. *Int. J. for Num. Meth. in Fluids*, 33(3), 2000.

[8] G. Barenblatt. *Scaling, Self-similarity, and Intermediate Asymptotics*. Cambridge University Press, New York, 1996.

[9] J. Bell, P. Colella, and H. Glaz. A second-order projection method for the incompressible Navier-Stokes equations. *J. Comput. Phys.*, 85:257, 1989.

[10] D. Bonn, J. Eggers, J. Indekeu, J. Meunier, and E. Rolley. Wetting and spreading. *Rev. Mod. Phys.*, 81:739, May 2009.

[11] J. Brackbill, D. Kothe, and C. Zemach. A continuum method for modeling surface tension. *J. Comput. Phys.*, 100:335, 1992.

[12] A. Briant, A. Wagner, and J. Yeomans. Lattice boltzmann simulations of contact line motion. i. liquid-gas systems. *Phys. Rev. E.*, 69:031602, 2004.

[13] F. Brochard-Wyart and C. Redon. Dynamics of Liquid Rim Instabilities. *Langmuir*, 8:2324, 1992.

[14] V. Carey. *Statistical Thermodynamics and Microscale Thermophysics*. The Press Syndicate of the University of Cambridge, Cambridge, 1999.

[15] N. Churaev and V. Sobolev. Prediction of contact angles on the basis of the Frumkin-Derjaguin approach. *Adv. Colloid Interface Sci.*, 61:1, 1995.

[16] C. Cottin-Bizonne, S. Jurine, J. Baudy, J. Crassous, F. Restagno, and E. Charlaix. Nanorheology: An investigation of the boundary condition at hydrophobic and hydrophilic interfaces. *Eur. Phys. J. E*, 9:47, 2002.

[17] R. Cox. The dynamics of the spreading of liquids on a solid surface. Part 1. Viscous flow. *Phys. Fluids*, 168:169, 1986.

[18] R. Craster and O. Matar. Dynamics and stability of thin liquid films. *Rev. Mod. Phys.*, 81:1131, 2009.

[19] S. Davis. Moving contact lines and rivulet instabilities. Part I: The static rivulet. *J. Fluid Mech.*, 98:225, 1980.

[20] B. Derjaguin and L. Landau. Theory of the stability of strongly charged lyophobic sols and of the adhesion of strongly charged particles in solutions of electrolytes. *Acta Physico Chemica USSR*, 14:633, 1941.

[21] J. Diez, A. Gonzalez, and L. Kondic. On the breakup of fluid rivulets. *Phys. Fluids*, 21:082105, 2009.

[22] J. Diez, R. Gratton, L. Thomas, and B. Marino. Laplace pressure driven drop spreading. *Phys. Fluids*, 6:24, 1994.

[23] J. Diez and L. Kondic. Computing three-dimensional thin film flows including contact lines. *J. Comput. Phys.*, 183:274, 2002.

[24] J. Diez and L. Kondic. On the breakup of fluid films of finite and infinite extent. *Phys. Fluids*, 19:072107, 2007.

[25] J. Diez, L. Kondic, and A. L. Bertozzi. Global models for moving contact lines. *Phys. Rev. E*, 63:011208, 2001.

[26] T. Driessen, R. Jeurissen, H. Wijshoff, F. Toschi, and D. Lohse. Stability of viscous long liquid filaments. *Phys. Fluids*, 25:062109, 2013.

[27] E. Dussan V. The moving contact line: the slip boundary condition. *J. Fluid Mech.*, 77:665, 1976.

[28] E. B. Dussan V. On the spreading of liquids on solid surfaces: Static and dynamic contact lines. *Annu. Rev. Fluid Mech.*, 11:317, 1979.

[29] J. Eggers. Nonlinear dynamics and breakup of free-surface flows. *Rev. Mod. Phy.*, 69:865, 1997.

[30] J. Eggers. Toward a description of contact line motion at higher capillary numbers. *Phys. Fluids*, 16:3491, 2004.

[31] J. Eggers. Contact line motion for partially wetting fluids. *Phys. Rev. E*, 72:061605, 2005.

[32] S. Fan, M. Chapline, N. Franklin, T. Tombler, A. Cassell, and H. Dai. Self-oriented regular arrays of carbon nanotubes and their field emission properties. *Science*, 283:512, 1999.

[33] G. Fleming and M. Ratner. Grand challenges in basic energy sciences. *Phys. Today*, 61:28, 2008.

[34] J. Fowlkes, L. Kondic, J. Diez, and P. Rack. Self-Assembly versus Directed Assembly of Nanoparticles via Pulsed Laser Induced Dewetting of Patterned Metal Films. *Nano Lett.*, 11:2478, 2011.

[35] J. Fowlkes, N. Roberts, Y. Wu, J. Diez, A. González, C. Hartnett, K. Mahady, S. Afkhami, L. Kondic, and P. Rack. Hierarchical nanoparticle ensembles synthesized by liquid phase directed self–assembly. *Nano Lett.*, 14:774, 2014.

[36] M. Francois, S. Cummins, E. Dendy, D. Kothe, J. Sicilian, and M. Williams. A balanced-force algorithm for continuous and sharp interfacial surface tension models within a volume tracking framework. *J. Comput. Phys.*, 213:141, 2006.

[37] M. Fuentes-Cabrera, B. Rhodes, J. Fowlkes, A. López-Benzanilla, H. Terrones, M. Simpson, and P. Rack. Molecular dynamics study of the dewetting of copper on graphite and graphene: Implications for nanoscale self-assembly. *Phys. Rev. E*, 83:041603, 2011.

[38] J. Gomba and G. Homsy. Analytical solutions for partially wetting two-dimensional droplets. *Langmuir*, 25:5684, 2009.

[39] A. González, J. Diez, and L. Kondic. Stability of a liquid ring on a substrate. *J. Fluid Mech.*, 718:246, 2013.

[40] A. González, J. Diez, Y. Wu, J. Fowlkes, P. Rack, and L. Kondic. Instability of Liquid Cu films on a SiO_2 Substrate. *Langmuir*, 29:9378, 2013.

[41] R. Goodwin and G. M. Homsy. Viscous Flow down a slope in the vicinity of a contact line. *Phys. Fluids A.*, 3:515, 1991.

[42] R. Gratton, J. A. Diez, L. P. Thomas, B. Marino, and S. Betelú. Quasi-self-similarity for wetting drops. *Phys. Rev. E*, 53:3563, 1996.

[43] H. Greenspan. On the motion of a small viscous droplet that wets a surface. *J. Fluid Mech.*, 84:125, 1978.

[44] P. Haley and M. Miksis. The effect of the contact line on droplet spreading. *J. Fluid Mech.*, 223:57, 1991.

[45] S. Henley, J. Carey, and S. Silva. Metal nanoparticle production by pulsed laser nanostructuring of thin metal lms. *Appl. Surf. Sci.*, 253:8080, 2007.

[46] L. Hocking and A. Rivers. The spreading of a drop by capillary action. *J. Fluid Mech.*, 121:425, 1982.

[47] C. Huh and L. Scriven. Hydrodynamic Model of Steady Movement of a Solid /Liquid/Fluid Contact Line. *J. Colloid Interface Sci.*, 35:85, 1971.

[48] J. Israelachvili. *Intermolecular and surface forces*. Academic Press, New York, 1992. second edition.

[49] J. Jacqmin. Calculation of two-phase navier-stokes flows using phase field modeling. *J. Comp. Phys.*, 155:96, 1999.

[50] J. Jacqmin. Contact-line dynamics of a diffuse fluid interface. *J. Fluid Mech.*, 402:57, 2000.

[51] J. Jacqmin. Onset of wetting failure in liquid-liquid systems. *J. Fluid Mech.*, 517:209, 2004.

[52] X. Jiang and A. J. James. Numerical simulation of the head-on collision of two equal-sized drops with van der Waals forces. *J. Eng. Math*, 59:99, 2007.

[53] P. Joseph and P. Tabeling. Direct measurement of the apparent slip length. *Phys. Rev. E*, 71:035303, 2005.

[54] L. Kondic, J. Diez, P. Rack, Y. Guan, and J. Fowlkes. Nanoparticle assembly via the dewetting of patterned thin metal lines: Understanding the instability mechanism. *Phys. Rev. E*, 79:026302, 2009.

[55] T. Lee and L. Liu. Lattice boltzmann simulations of micron-scale drop impact on dry surfaces. *J. Comp. Phys.*, 229:8045, 2010.

[56] K. Mahady, S. Afkhami, and L. Kondic. A volume of fluid method for simulating fluid/fluid interfaces in contact with solid boundaries. *J. Comp. Phys.*, 294:243, 2015.

[57] S. Maier. *Plasmonics: Fundamentals and Applications*. Springer-Verlag, New York, 2007.

[58] S. Maier, P. Kik, H. Atwater, S. Meltzer, E. Harel, B. Koel, and A. Requicha. Local detection of electromagnetic energy transport below the diffraction limit in metal nanoparticle plasmon waveguide. *Nat. Mat.*, 2:229, 2003.

[59] Y. Min, M. Akbulut, K. Kristiansen, Y. Golan, and J. Israelachvili. The role of interparticle and external forces in nanoparticle assembly. *Nat. Materials*, 7:527, 2008.

[60] A. Münch and B. Wagner. Contact-line instability of dewetting thin films. *Physica D*, 209:178, 2005.

[61] T. Nguyen, M. Fuentes-Cabrera, J. Fowlkes, J. Diez, A. González, L. Kondic, and P. Rack. Competition between collapse and breakup in nanometer-sized thin rings using molecular dynamics and continuum modeling. *Langmuir*, 28, 2012.

[62] Z. Nie, A. Petukhova, and E. Kumacheva. Properties and emerging applications of self-assembled structures made from inorganic nanoparticles. *Nature Nanotech.*, 453:15, 2009.

[63] A. Oron, S. Davis, and S. Bankoff. Long-scale evolution of thin liquid films. *Rev. Mod. Phys.*, 69:931, 1997.

[64] C. Perazzo and J. Gratton. Navier-Stokes solutions for parallel flow in rivulets on an inclined plane. *J. Fluid Mech.*, 507:367, 2004.

[65] R. Pit, H. Hervet, and L. Leger. Direct experimental evidence of slip in hexadecane: Solid interfaces. *Phys. Rev. Lett.*, 85:980, 2000.

[66] S. Popinet. An accurate adaptive solver for surface-tension-driven interfacial flows. *J. Comput. Phys.*, 228:5838, 2009.

[67] S. Popinet. The Gerris flow solver. http://gfs.sourceforge.net/, 2012. 1.3.2.

[68] T. Qian, X.-P. Wang, and P. Sheng. Molecular hydrodynamics of the moving contact line in two-phase immiscible flows. *Comm. Comput. Phys.*, 1:1, 2006.

[69] Lord Rayleigh. On the instability of jets. *Proc. London Math. Soc.*, 1:4, 1878.

[70] M. Renardy, Y. Renardy, and J. Li. Numerical Simulation of Moving Contact Line Problems Using a Volume-of-Fluid Method. *J. Comput. Phys.*, 171:243, 2001.

[71] Y. Renardy and M. Renardy. PROST: a parabolic reconstruction of surface tension for the volume-of-fluid method. *J. Comput. Phys.*, 183:400, 2002.

[72] N. Roberts, J. Fowlkes, K. Mahady, S. Afkhami, L. Kondic, and P. Rack. Directed assembly of one- and two-dimensional nanoparticle arrays from pulsed laser induced dewetting of square waveforms. *ACS Appl. Mater. Interfaces*, 5:4450, 2013.

[73] R. Scardovelli and S. Zaleski. Analytical relations connecting linear interfaces and volume fractions in rectangular grids. *J. Comput. Phys.*, 164:228, 2000.

[74] L. Schwartz and R. Eley. Simulation of droplet motion on low-energy and heterogeneous surfaces. *J. Colloid Interface Sci.*, 202:173, 1998.

[75] L. Schwartz, R. Roy, R. Eley, and S. Petrash. Simulation of droplet motion on low-energy and heterogeneous surfaces. *J. Colloid Interface Sci.*, 234:363, 2001.

[76] Y.D. Shikhmurzaev. Moving contact lines in liquid/liquid/solid systems. *J. Fluid Mech.*, 334:211, 1997.

[77] D. Sibley, A. Nold, and S. Kalliadasis. Unifying binary fluid diffuse-interface models in the sharp interface limit. *J. Fluid Mech.*, 736:5, 2013.

[78] J. Snoeijer. A microscopic view on contact angle selection. *Phys. Fluids*, 20:057101, 2008.

[79] J. H. Snoeijer. Free-surface flows with large slope: Beyond lubrication theory. *Physics Fluids*, 18:021701, 2006.

[80] P. Spelt. A level-set approach for simulations of flows with multiple moving contact lines with hysteresis. *J. Comput. Phys.*, 207:389, 2005.

[81] J. E. Sprittles and Y. D. Shikhmurzaev. Finite element framework for describing dynamic wetting phenomena. *Int. J. Numer. Meth. Fluids*, 68:1257, 2012.

[82] J. E. Sprittles and Y. D. Shikhmurzaev. Finite element simulation of dynamic wetting flows as an interface formation process. *J. Comput. Phys.*, 233:34, 2013.

[83] Y. Sui and Peter D.M. Spelt. An efficient computational model for macroscale simulations of moving contact lines. *J. Comput. Phys.*, 242:37, 2013.

[84] S. Sun, C. Murray, D. Weller, L. Folks, and A. Moser. Monodisperse FePt nanoparticles and ferromagnetic FePt nanocrystal superlattices. *Science*, 287:1989, 2000.

[85] M. Sussman. A second order coupled level set and volume-of-fluid method for computing growth and collapse of vapor bubbles. *J. Comput. Phys*, 187:110, 2003.

[86] M. Sussman. A method for overcoming the surface tension time step constraint in multiphase flows II. *Int. J. Numer. Meth. Fluids*, 68:1343, 2012.

[87] M. Sussman, A. S. Almgren, J. B. Bell, P. Colella, L. H. Howell, and M. L. Welcome. An adaptive level set approach for incompressible two-phase flows. *J. Comput. Phys.*, 148:81, 1999.

[88] L. Tanner. The spreading of silicone oil drops on horizontal surfaces. *J. Phys. D.*, 12:1473, 1979.

[89] M. Torrey, L. Cloutman, R. Mjolsness, and C. Hirt. NASA-VOF2D: a computer program for incompressible flows with free surfaces. *NASA STI/Recon Technical Report N*, 86:30116, 1985.

[90] J. Trice, D. Thomas, C. Favazza, R. Sureshkumar, and R. Kalyanaraman. Pulsed-laser-induced dewetting in nanoscopic metal films: Theory and experiments. *Phys. Rev. B*, 75:235439, 2007.

[91] S. Unverdi and G. Tryggvason. A front-tracking method for viscous, incompressible, multi-fluid flows. *J. Comp. Phys.*, 100:25, 1992.

[92] O. Voinov. Hydrodynamics of wetting. *Fluid Dynamics*, 11:714, 1976.

[93] Y. Wu, J. Fowlkes, P. Rack, J. Diez, and L. Kondic. On the Breakup of Patterned Nanoscale Copper Rings into Droplets via Pulsed-Laser-Induced Dewetting: Competing Liquid-Phase Instability and Transport Mechanisms. *Langmuir*, 26:11972, 2010.

[94] Y. Wu, J. Fowlkes, N. Roberts, J. Diez, L. Kondic, A. Gonzalez, and P. Rack. Competing Liquid Phase Instabilities during Pulsed Laser Induced Self-Assembly of Copper Rings into Ordered Nanoparticle Arrays on SiO2. *Langmuir*, 2011. to appear.

[95] T. Young. An essay on the cohesion of fluids. *Philos. Trans. R. Soc. London*, 95, 1805.

[96] P. Yue, C. Zhou, and J. Feng. Sharp-interface limit of the Cahn-Hilliard model for moving contact lines. *J. Fluid Mech.*, 645:279, 2010.